POLITECNICO DI TORINO

Collegio di Ingegneria Meccanica, Aerospaziale, dell'Autoveicolo e della Produzione

Corso di Laurea Magistrale
in Ingegneria Meccanica (Mechanical Engineering)

Tesi di Laurea Magistrale

Spray characterization of a planar airblast prefilmer under oscillating airflow conditions

Relatore
prof. Eliodoro Chiavazzo

Candidato
Matteo Occhialini

Correlatori
prof. Nikolaos Zarzalis
prof. Hans-Jörg Bauer

Dicembre 2020

Contents

List of symbols and abbreviations

Latin symbols

Symbol	Description	Unit
A_x, A_y	Cross sectional area	[m^2]
C_D	Drag coefficient	[-]
d, D	Droplet diameter	[m]
d_x, d_y, d_z	Measurement volume dimensions	[m]
D_0	Orifice diameter	[m]
E	Beam expansion factor	[-]
E	Bridge voltage	[V]
f	Frequency	[Hz]
f_{vx}, f_{vy}	Volume flow	[m s^{-1}]
i, j, k	Element index	[-]
L_S	Photodetector slit width	[m]
$\dot{m}'$	Mass flux	[kg m^{-2} s^{-1}]
$\dot{m}$	Mass flow rate	[kg s^{-1}]
m	Relative refractive index	[-]
n	Absolute refractive index	[-]
n	Siren rotational speed	[RPM]
N	Number of particles	[-]
Oh	Ohnesorge number	[-]
p	Pressure	[Pa]
Re	Reynolds number	[-]
S_g	Geometric standard deviation	[-]

S_n	Standard deviation	[-]
u, U	Velocity	[m s^{-1}]
t	Time	[s]
th	Liquid sheet thickness	[m]
T	Temperature	[K]
We	Weber number	[-]
X, Y, Z	Coordinates	[-]

Greek symbols

Symbol	Importance	Unit
β	Geometric correction factor	[m]
δ_f	Fringe distance	[m]
Δ	Difference	[-]
θ	Beam angle intersection	[°]
λ	Wavelength	[m]
μ	dynamic viscosity	[kg m^{-1} s^{-1}]
ρ	Density	[kg m^{-3}]
σ	Surface tension	[kg s^{-1}]
φ	Scattering angle	[°]
Φ	Phase shift	[°]
Ψ	Azimuth angle	[°]
$\dot{\omega}'_T$	Heat release	[W]

Subscripts

Symbol	Description
$()_d$	Droplet
$()_A$	Air
$()_R$	Relative

Abbreviations

Symbol	Description
AFR	Air to Fuel Ratio
ALR	Air to Liquid Ratio
CTA	Constant Temperature Anemometry
DPSS	Diode Pumped Solid State
FFT	Fast Fourier Transform
LPP	Lean Premixed Prevaporised
PDA	Phase Doppler Anemometry
RQL	Rich Quench Lean
SMD	Sauter Mean Diameter
SNR	Signal to Noise Ratio
UHC	Unburned Hydrocarbons

1 Introduction

In order to achieve the higher requirements concerning clean combustion technology in the aircraft engines applications and reducing in this way harmful emissions, in particular nitrogen oxides emissions, the major jet engine manufacturers are developing lean premixed pre-evaporators (LPP) that operate at very high pressure. In this context, it is possible that thermoacoustic instabilities occur inside the combustion chamber. The unsteady heat released by the flame generates pressure waves that are linked with a feedback loop to the inlet air velocity [1]. This loop enhances the instabilities of the inlet air velocity, which as a result affects the atomization process. Since the atomization process on the airblast atomizers of most jet engine combustors is governing crucial operating characteristics such as the air-to-fuel ratio (AFR) distribution inside the combustor, the flame's stability or the NO_x emissions, the predictions of the performance of this process under unsteady conditions has a significant value [2].

The main problem with the introduction of thermoacoustic instabilities in a combustor is that they carry a high risk for reduced robustness and lifetime of the engines. If not mitigated, these interactions (strongly fluctuating heat release of the combustion process with naturally occurring acoustic resonances) can reduce the lifetime of crucial components and potentially lead to premature mechanical failures. High-frequency combustion instabilities are more likely due to the relatively short aero-engine combustor geometries [3].

Fluctuations of the AFR inside the chamber means that the generated spray characteristics and properties are changing; a need to predict the instabilities in the droplet behaviour arises. Some of the well defined in the literature characteristics of the spray are the Sauter Mean Diameter (SMD), the mean diameter, as well as the droplet velocity. These characteristics of the spray can be measured by means of non-intrusive techniques such as Phase Doppler Anemometry (PDA). The unsteady flow field of the airflow can be determined by utilizing hot wire Constant Temperature Anemometry (CTA), which can provide the frequencies lying in the system by means of the appropriate post processing method.

For the purposes of the present investigation, the aforementioned methods and techniques were applied. By measuring the properties of a spray produced by a generic planar airblast atomizer, the complete characterization of the spray under steady airflow conditions can be achieved, in order to finally examine the influence of the unsteady flow field on the atomization process.

2 Basics and Theory

2.1 Basics of a combustion chamber in a jet engine

Aero engines contribute to alter the concentration of atmospheric ozone by directly emitting into the upper troposphere and lower stratosphere a number of chemically active species like nitric oxide (NO), nitrogen-dioxide (NO_2) and soot. Calculated estimates show that such aircraft-related emissions have increased the concentration of NO_x at cruise altitudes in the northern mid-latitudes by approximately 20% [4]. The latest new technological improvements in combustion efficiency have decreased CO, CO_2 and Unburned Hydrocarbons (UHC) emissions but NO_x have remained fairly unaffected.

The most important factor affecting the NO_x formation rates is known to be the flame temperature, exhibiting an exponential influence. Furthermore, NO_x production is shown to linearly increase with rising combustor residence times. However, a trade-off between NO_x emissions and CO and UHC emissions should be done since low temperatures and low combustor residence times tend to decrease NO_x but increase the other emissions (Figure 2.1).

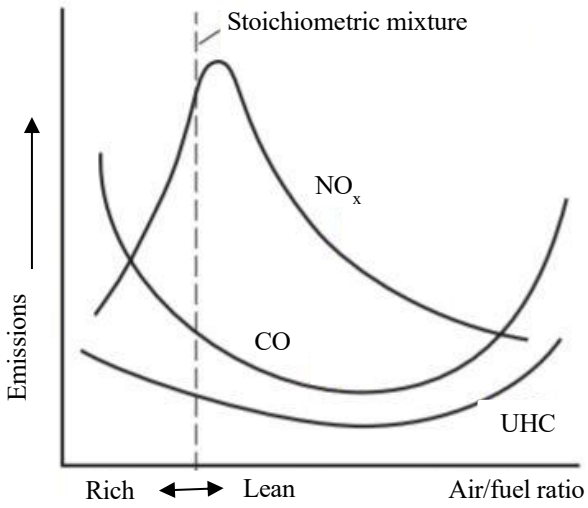

Figure 2.1: Emissions characteristics as a function of the air-fuel-ratio [5].

Depending on whether the regime under which combustion takes place is lean or rich, two different concepts have emerged as the most promising solutions:

1) **Rich-burn / Quick-quench / Lean-burn (RQL) combustion**. With this configuration, the combustion chamber is divided in two principal zones: a rich primary zone and a lean burnout zone. In between the two ones, a fast quenching zone takes place; here a big amount of air enters the combustion chamber and makes the AFR pass from rich to lean burning conditions. In the following figure a sector of annular RQL-combustor is shown, where the mentioned zones are depicted.

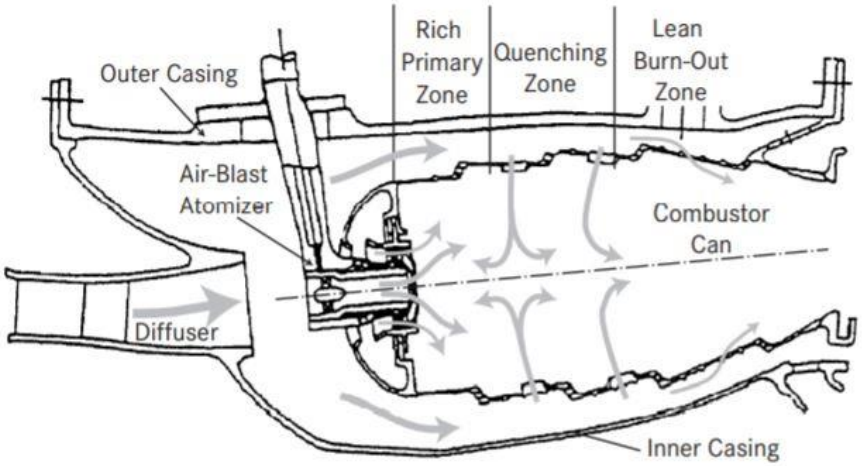

Figure 2.2: Typical RQL-combustor [6].

This type of staged combustion is commonly found in modern combustor designs but the potential of NO_x reduction is limited in practice due to the increased formation of soot.

2) **Lean-Premixed-Prevaporised (LPP) combustion**. With this configuration there are no zones inside the combustion chamber in which the AFR is close to the stoichiometric burning conditions [7] and for this reason, according also to Figure 2.1, it is possible to note that the NO_x reduction potential is higher if compared to the RQL combustor. The combustion process takes place entirely in the lean regime. Prerequisites for this type of combustor are a near-perfect mixture homogeneity before combustion and a sufficiently large auto-ignition delay time ([8],[9],[10]). In order to achieve these conditions LPP-burner design strives for intense air-fuel mixing and prevaporisation within an additional pre-mixing section being part of the injector. This section has to be kept axially short enough to avoid auto-ignition of the combustible mixture in the duct. A schematic view of an LPP-combustor cross section is shown in the following figure.

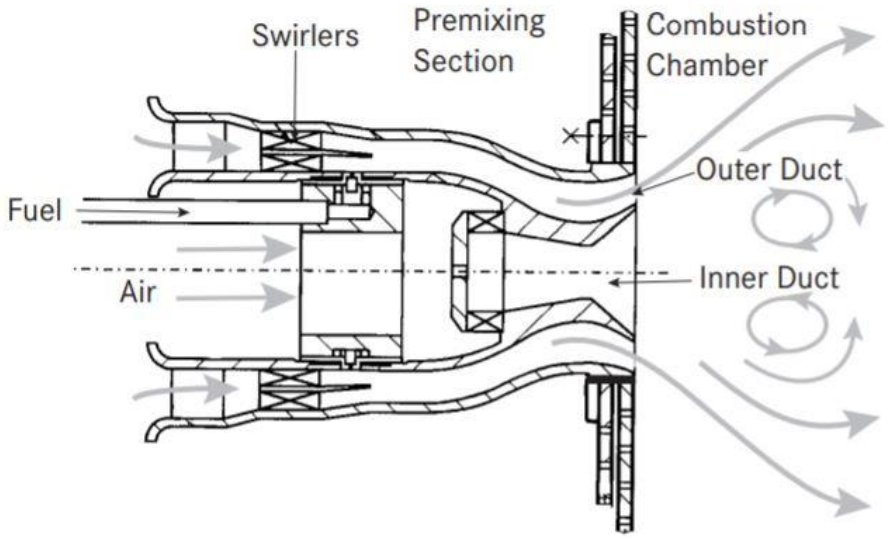

Figure 2.3: Generic LPP-injector design [9].

The main problem of the LPP design is that they are more likely to be affected by thermoacoustic instabilities [1]. More information regarding this subject is mentioned in 2.3.

2.2 Atomization process

Liquid atomization of sprays is used in power engineering (combustion processes, attemperation of steam, water cooling, cleaning of boiler pipe screens, water treatment, improvement of the composition of combustion products), mechanical engineering (oil mist lubrication, liquid metal atomization, spray coating, washing and cleaning, cooling), transport (piston engines, spark-ignition engine, flow engines, rocket engines, airfield service), agriculture and forecast industry, chemical engineering (spray-drying), environmental protection (gas scrubbing, pollution propagation protection, fire protection) and many other various fields [11].

Atomization is the process whereby a volume of liquid is converted into a multiplicity of small drops [12]. A high ratio of surface to mass in the liquid phase is the main target of an efficient atomization process.

The main targets of a good atomization process are a large and rapid increase of surface area that guarantees an increase in the heat and mass transfer rates. Furthermore, it plays an important role

in controlling NO_x, CO_2 and unburned hydrocarbons since ignition and flame stability vary according also to the droplet size of the fuel and air-fuel mixture properties.

2.2.1 Types and classification of atomizers

In this chapter a brief overview among the different atomization techniques and atomizers is given with a higher level of explanation for the airblast one, which is used in this work. A detailed classification of the different types of atomizers is proposed in [11]. The "energy approach" may be applied in order to distinguish among the different typologies, according to [13], [14] and [15]. Atomization is guaranteed by the presence of a relative velocity between the liquid and gaseous phase.

The first type of atomizer takes advantage of a high pressure drop across the nozzle: the liquid is pumped at a high pressure through a small orifice and then it expands in the environment gaining high velocity values. For this reason, they are called pressure atomizers. The relative velocity is reached because of the high liquid velocity, while the air velocity remains low. An example is the plain orifice in which a simple circular orifice is used to inject a round liquid jet into the surrounding air. The smaller the diameter of the orifice the finer the droplets obtained but a limit in the reduction of this dimension is given by the foreign solid particles that could be present in the liquid. For more details about pressure atomizers refers to [12].

The second one applies a centrifugal force to the liquid by using a mechanical device driven by an electrical motor. In this way, the energy is transmitted from the device to the liquid, which is forced to flow radially, and it leaves the atomizer from its periphery with high kinetic energy and it disintegrates. A 360° spray is generated and it is usually inserted in cylindrical or conical chambers where an umbrella-like shape is created by downward gas currents [16]. These atomizers are named rotary atomizers and their application is more common with respect to the pressure atomizers since they allow independent variation of flow rate and disk speed, thereby providing more flexibility in operation [17].

The last type are the twin fluid atomizers whose principle of operation is the use of shear stresses caused by the interaction of aerodynamic forces at the gas-liquid interface. Two categories belong to this branch: air-assist atomizers which take advantage of small quantities of air with high velocities (until sonic values) and airblast atomizers which use high air flow rates at lower speeds instead.

The following figure (Figure 2.4) shows the different aforementioned atomizer types.

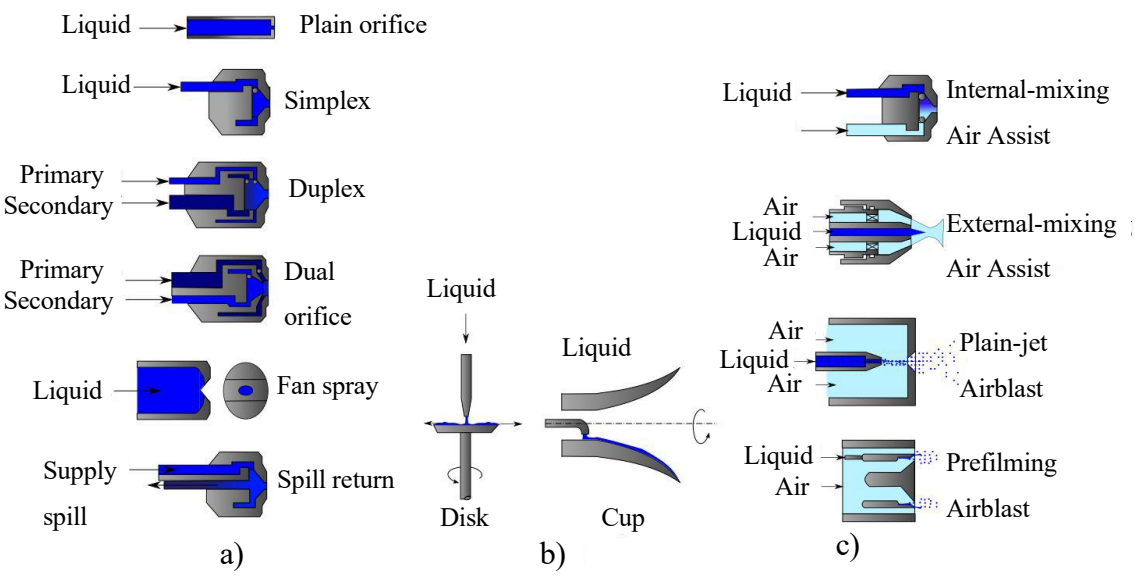

Figure 2.4: Atomizers classification. a) Pressure atomizers b) Rotary atomizers c) Twin fluid atomizer [18].

Since an airblast atomizer was used during this project, a better explanation for this type of atomizer needs to be discussed. In recent years, this method has started to be preferred to the pressure atomizer. The relative velocity is guaranteed by an high air velocity and a low liquid velocity, thus being the opposite of the pressure atomizers. The advantages of the airblast approach are even more important in the field of gas turbines engines with high compression ratios [19]. They require lower fuel pressures and produce a finer spray. Moreover, because the airblast atomization process ensures thorough mixing of air and fuel, the ensuing combustion process is characterized by very low soot formation and a blue flame of low luminosity, resulting in relatively cool liner walls and a minimum of exhaust smoke [12]. A further asset of the airblast atomizer is that it provides a sensibly homogeneous fuel distribution over the entire range of fuel flows. This offers an important practical advantage in the temperature distribution in the chamber efflux gases, which is crucial for turbine blade life at high pressures, which may be adequately predicted from temperature surveys carried out at lower and more convenient levels of pressure.

Most of the airblast atomizers, and also the one used in this work, are of the prefilming type: the liquid is firstly spread out in a thin continuous sheet and then undergoes the atomizing action by means of high velocity air. In order to fulfil this objective a high relative velocity between the liquid and the surrounding is required. The influence of liquid physical properties, air velocities, film flow rate, pre-filming length and atomizing edge thickness has been investigated for prefilming airblast atomizers [20]. Mean air velocity and atomizing edge thickness were found to

be the dominating parameters. The prefilming length, liquid physical properties and liquid volume flow rate seem to have only a minor effect on the mean droplet diameter but affect the ligament formation process.

Some high-performance aircraft engines use a piloted or hybrid airblast atomizer in which a pressure swirl atomizer is also included in order to overcome issues (poor atomization) due to possible low velocity air associated with low cranking speeds [21].

Another alternative form of airblast atomizer is the plain-jet atomizer. In this nozzle the fuel flows through a number of radially drilled plain circular holes, from which it emerges in the form of discrete jets that enter a swirling airstream. These jets then undergo an in-flight disintegration without any further preparation such as prefilming [17].

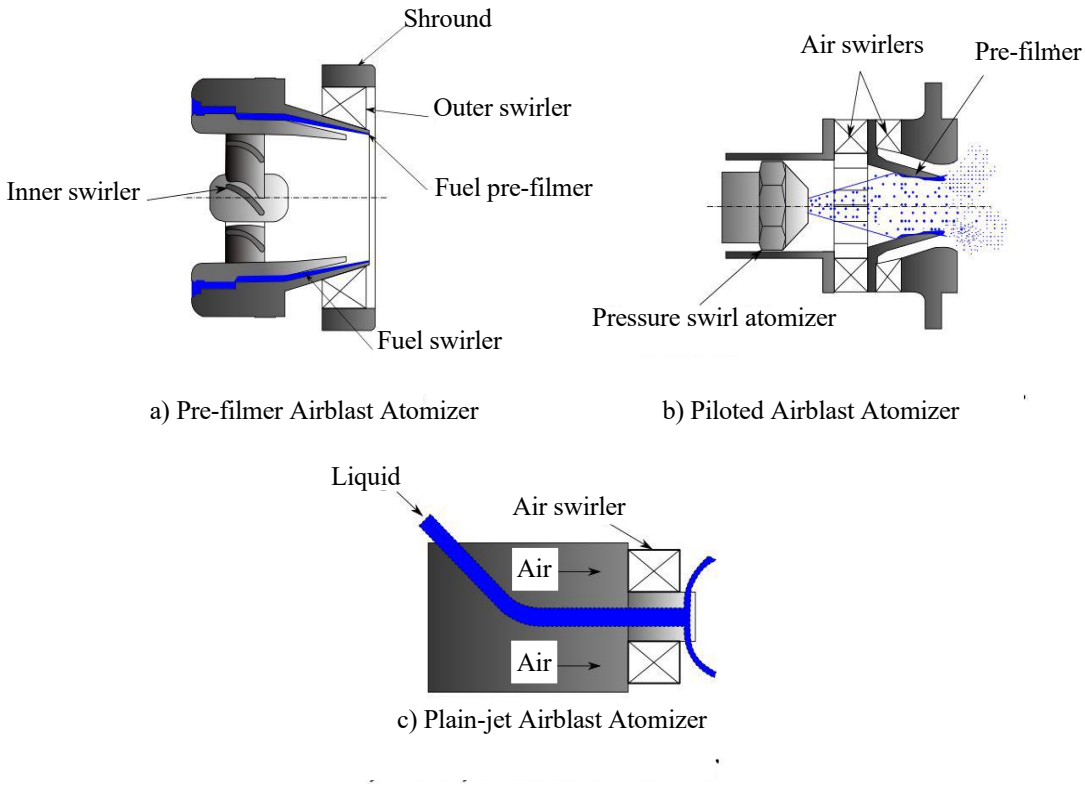

Figure 2.5: Airblast atomizers. a) Pre-filmer airblast b) Piloted airblast c) Plain-jet airblast [18].

2.2.2 Breakup mechanisms

The process of generation of the spray can be divided into two steps: a primary atomization in which the fuel stream is broken up into shreds and ligaments and a secondary atomization in which the large liquid elements previously created are finally disintegrated in smaller droplets.

During these stages the most influencing parameters for the spray characteristics (particle size, distribution, mean droplet velocity) are the internal geometry of the atomizer, the liquid properties and the properties of the medium into which the liquid is injected [11].

Breakup of drops

The breakup of a droplet is caused by the interaction of the droplet itself with the aerodynamic forces of the surrounding air. The exact mathematical solution of the breakup dynamic requires the knowledge of the distribution of the aerodynamic pressure in each point of the droplet surface. However, as soon as the drop is deformed by these pressures, the pressure distribution on its surface changes, thus leading to a different state of equilibrium and causing a possible breakup. These changes in the pressure distribution on the droplet surface are discussed in detail in [22].

The forces involved in the equilibrium are the external aerodynamic forces of the air p_A that tend to disintegrate the droplet, the surface tension pressure p_σ and the internal pressure at any point on the drop surface p_1. At the equilibrium condition it results

$$p_1 = p_A + p_\sigma = constant \tag{2.1}$$

where for a spherical drop the surface tension pressure is

$$p_\sigma = \frac{4\sigma}{D} \tag{2.2}$$

A drop can remain stable if p_1 does not change, so for any change in the external aerodynamic forces that cause a change in p_A, the surface tension p_σ should change accordingly in order to keep p_1 constant. If p_A is much larger and p_σ cannot reach such high values in order to guarantee the equilibrium, the drop will undergo further deformation that reduce p_σ and it will breakup into smaller drops [23]. The disintegration process will continue until a droplet dimension that can guarantee a value of p_σ large enough is reached. Decreasing the droplet diameter, the breakup time will increase accordingly until the stable drop size for which an infinite breakup time is attained [24].

Considering a droplet breakup in flowing air, which is the case in this work, many theories were formulated since the twentieth century. The influence of the flow pattern around the liquid droplets induces the aerodynamic forces to act on them and to deform in some way. Three types of deformation were identified by Hinze [25]:

1. *Lenticular deformation* (Figure 2.6 a): the droplet is flattened to form an oblate ellipsoid. Subsequent deformation depends on the magnitude of the internal forces causing deformation. The ellipsoid is then converted into a torus that gets stretched and disintegrate into small drops [17].
2. *Cigar-shaped deformation* (Figure 2.6 b): the initial drop becomes elongated to form a long cylindrical thread or ligament that breaks up into small drops.
3. *Bulgy deformation* (Figure 2.6 c): local deformations on the drop surface cause the detachment of protuberances that are going to form new smaller drops.

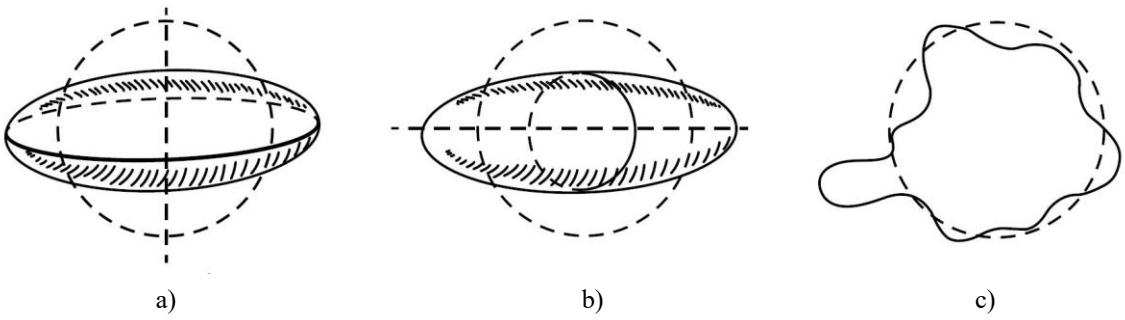

Figure 2.6: Deformations: a) Lenticular b) Cigar-shaped c) Bulgy [17].

The preference for one of the above described types of deformation depends mostly on the physical properties of the gas and liquid phases (density, viscosity, interfacial tension) and on the flow pattern around the drop [17].

For liquids of low viscosity, the deformation of a drop is mainly dependent on the ratio between the aerodynamic forces represented by $0.5\rho_A U_R^2$ (in which ρ_A is the air density and U_R is the relative velocity between air and liquid) and the surface tension forces that are related to σ/D. Writing the ratio and rearranging it in a dimensionless form, it is possible to obtain

$$We_{crit} = \left(\frac{\rho_A U_R^2 D}{\sigma}\right)_{crit} = \frac{8}{C_D} \tag{2.3}$$

in which the term inside the parenthesis represents the Weber number and the subscript stands for a reached critical condition. Knowing the critical Weber number it is possible to determine the dimension of the stable droplet for a given air velocity or, in other studies, it has been investigated which is the critical relative velocity U_R at which the particle of a given diameter will breakup

(see [25], [26]). According to the way in which the liquid is exposed to the airflow, different Weber numbers are proposed in the literature: $We_{crit} = 22$ for a free falling drop (steady stream), $We_{crit} = 13$ for drops suddenly exposed to an airflow at a constant speed [17].

Another important property to take into account for the understanding of the droplet breakup mechanism is the viscosity of the liquid, μ_d, which acts in favour of the droplet stabilization. The Ohnesorge number is a dimensionless parameter representing the ratio of the viscous forces to inertial and surface tension forces [27].

$$Oh = \frac{\sqrt{We}}{Re} = \left[\frac{\rho_A U_R^2 D}{\sigma_d}\right]^{0.5} \left[\frac{\mu_d}{\rho_d U_R D}\right] \tag{2.4}$$

in which the subscript d stands for droplet. The effect of viscosity influences the value of the Oh number and the critical We number also changes by following the relation

$$We_{crit\_eff} = We_{crit}[1 + f(Oh)] \tag{2.5}$$

in which We_{crit} is the critical Weber number for zero viscosity [25]. Other relations are proposed in literature by Brodkey [28] and Gelfand [29], who suggested that the role of viscosity is to delay breakup.

Literature proposes different theories about the relation between the Weber and Ohnesorge numbers during the deformation process. In Figure 2.7 is shown a summary of these theories.

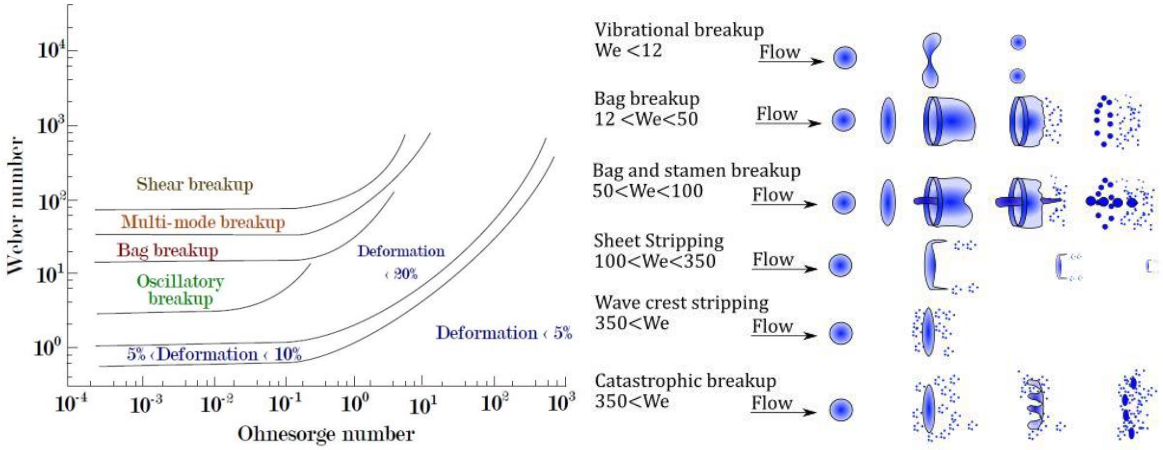

a) b)

Figure 2.7: a) Droplet breakup regime map b) Modes of droplet breakup [22].

For low We and Oh values, different levels of deformation are present. Increasing We, the deformation of the droplet increases until a different breakup mode appears. For higher Oh, the deformation region increases and the breakup region starts at higher We numbers.

Breakup of liquid jets

The breakup of liquid jets corresponds to the primary atomization step and it is in general much more complex to describe compared to the droplet breakup. The disintegration mechanism is mostly caused by the propagation of waves in the liquid surface and by their change in amplitude that causes a certain loss of stability [11]. Several studies were performed inducing on the liquid surface small perturbances generated by internal (liquid swirling, liquid expansion due to pressure drop, vibrations of the atomizers) and external (interaction with the surrounding media, different aerodynamic forces) vibrations. The mathematical solution of the effects caused by these perturbations is proposed in [11].

Generally, there are three different forms of disintegration caused by axisymmetric waves, asymmetric waves (called "first wind induced atomization") and aerodynamics forces and they apply to velocities of order 1 m/s, 10 m/s and 100 m/s respectively. A fourth type was added in which the effects of turbulence and aerodynamic forces are predominant for the atomization process ("turbulent breakup") [30]. Figure 2.8 represents a map that collects all types of this analysis [31] and associates the typology of breakup with the corresponding values of Ohnesorge and Reynolds numbers.

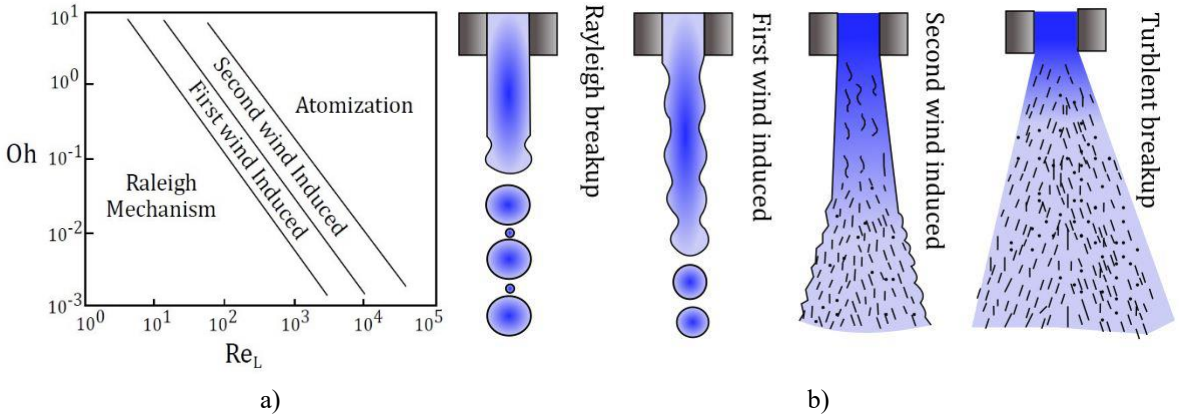

Figure 2.8: a) Jet breakup regime. b) Jet breakup modes [18]

The map in Figure 2.8 can be divided in four regions [17]:

1. the first breakup method above showed is the Rayleigh breakup and it is valid for the disintegration of liquid jets at low velocities in a vacuum. It is induced by the axisymmetric oscillations of the jet surface. From [32] the mathematical solution to the problem gives as result an average diameter d of the formed droplets:

$$d \geq 1.436 D_0 \tag{2.6}$$

where D_0 is the orifice diameter. Introducing the viscosity of the fluid, the above equation becomes:

$$\frac{d}{D_0} = 1.436(1 + 3Oh)^{\frac{1}{6}} \tag{2.7}$$

In his work, Rayleigh also demonstrates which is the critical wavelength at which the jet starts to become unstable:

$$\lambda = 4.51 D_0 \tag{2.8}$$

Smaller wavelength are damped by the surface tension [33]. The contribution of increased liquid viscosity increases the critical wavelength value.

2. The first wind-induced breakup method in which the surface tension is augmented by the relative velocity between the jet and the air, which produces a static pressure distribution across the jet, thereby accelerating the breakup process. Breakup occurs many jet diameters downstream of the nozzle. Mean droplet diameter d is about the same as the orifice diameter D_0.
3. The second wind-induced breakup method is attained for higher relative velocities. Drops are produced by the unstable growth of short wavelength surface waves on the jet surface. The produced diameter is much smaller than the orifice diameter D_0.
4. The atomization or turbulent breakup method causes a complete disruption of the jet exactly at the nozzle exit and the produced drops that have a diameter which is much smaller than the orifice diameter.

Disintegration of flat sheets

The disintegration of a sheet depends mainly on the liquid discharge velocity. Since a liquid sheet disintegrates initially into jets and then into droplets, the lack of stability is the factor that induces

to the breakup. According to the sheet discharge velocity, three characteristic modes of sheet disruption can be identified [11]:

1. With a discharge velocity of a few meters per second the liquid sheet becomes thinner by increasing its distance from the atomization edge, then a series of perforations develop in sufficiently thin areas. When the net of perforations becomes bigger, it is possible to identify different liquid jets that in the end, when they lose stability, collapse into droplets.
2. For increasing discharge velocities, the sheet undergoes wave disturbances (annular and circumferential waves appear) whose main direction is longitudinal to the velocity direction of the sheet. In the end, it disintegrates into annuli who subsequently disintegrate into droplets.
3. For very high discharge velocities (around 100 m/s) the flat sheet is directly disintegrated into drops without the formation of annuli. The wavelength of the disturbances is short and, as soon as they gain a bigger amplitude, they cause the loss of stability and the direct atomization takes place.

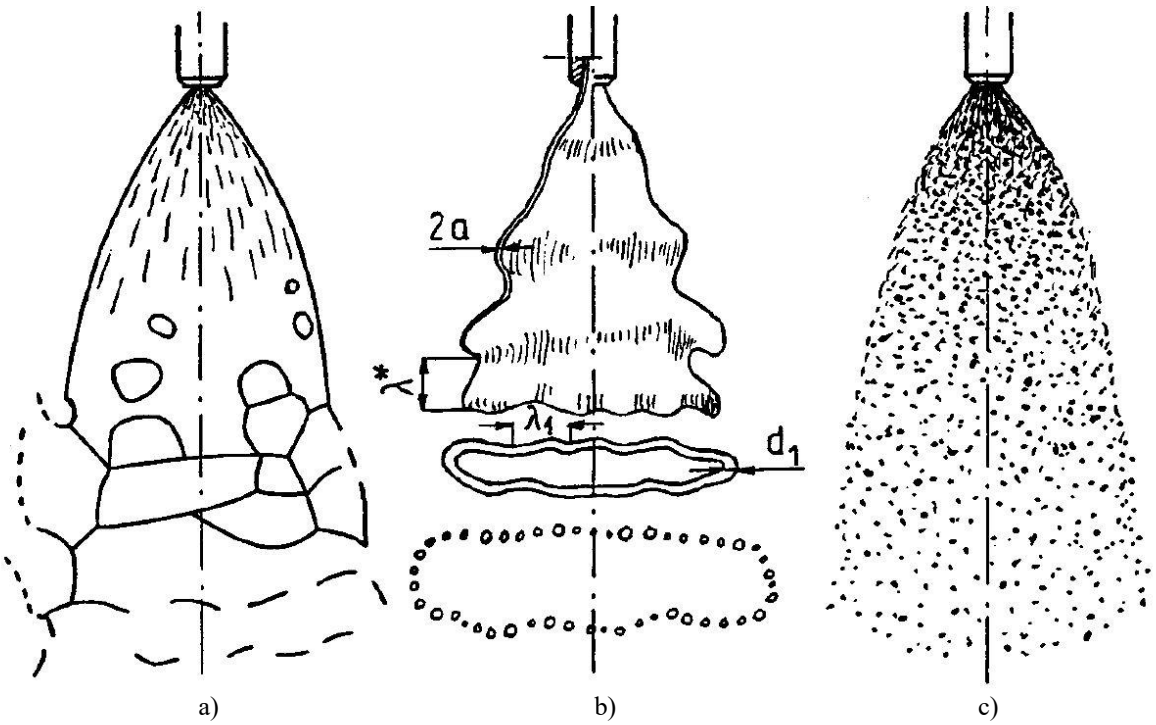

Figure 2.9: Sheet disintegration. a) Perforation b) Wave phenomena c) Atomization [11].

Rizk and Lefebvre studied the particular case of an airblast atomizer and investigated how the thickness of the liquid sheet influences the generated spray characteristics [34]. In particular, they

observed that a thinner film can generate smaller droplets and the SMD turns to be lower, according to the following relation

$$SMD \propto th^{0.4} \tag{2.9}$$

where *th* is the thickness of the liquid sheet.

Furthermore, they observed that higher liquid viscosity values create thicker films and so larger drops and for this reason they underlined the importance of spreading the liquid into a very thin sheet to achieve the finest atomization [17].

2.2.3 Spray distribution

A general definition of a spray is "a system of drops immersed in a gaseous continuous phase" [17]. Usually, atomizers produce sprays composed of drops whose diameter can vary in a range from few to 500 μm as a consequence of different breakup mechanisms. Therefore, the mean drop size should be integrated with the distribution of drop sizes in order to fully characterize the spray. The graphical representation of the distribution can be built with a histogram in which in the abscissas there are the diameter ranges and in the ordinates the particle number or the corresponding volume of the spray occupied by the particles whose diameter falls in the interval with extremes $D - \Delta D/2$ and $D + \Delta D/2$. In the second case, the distribution is skewed to the right due to the weighting effect of the larger drops (Figure 2.10). If ΔD tends to zero, the columns of the interval can be substituted by a frequency curve that may be regarded as a characteristic of the spray, provided it is based on a sufficient big number of samples. In the ordinates it is possible to show the values in different ways: number of drops with a given diameter, relative number or fraction of the total, or the fraction of the total number per size class. Cumulative frequency plot can also be built: they are essentially a plot of the integral of the frequency curve and it represents the percentage of the total number of drops in the spray that is below a certain diameter.

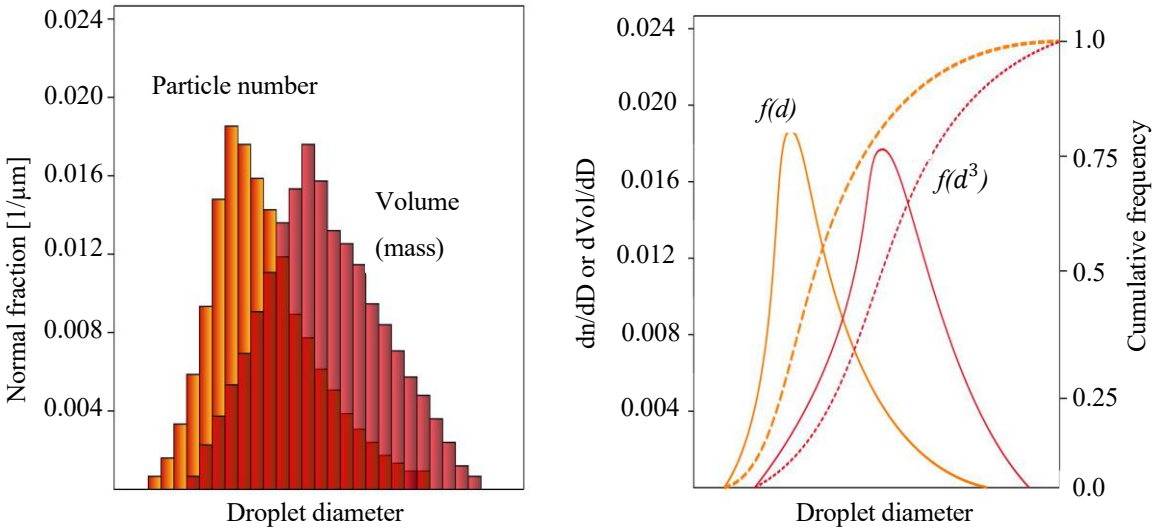

Figure 2.10: Graphical representation of droplet size distribution [18].

The increasing need to compare simulation models to experimental data and the possibility to obtain interesting results also from limited number of detected droplets has driven the research into finding continuous mathematical functions that describe accurately a drop distribution starting from few parameters. According to [35], some requirements of these mathematical models are: provide a satisfactory fit to the drop size data, allow extrapolation to drop sizes outside of the measured values, permit calculations of representative drop diameters and other parameters of interest, furnish a means of consolidating large amounts of data and give some insights into the basic mechanism involved in atomization. Different functions have been proposed based on probability or purely empirical considerations which allow the mathematical representation. The most common ones are generally the normal, log-normal, Nukiyama-Tanasawa, Rosin-Rammler and the upper-limit distributions.

The normal distribution function is based on the random occurrence of a given drop size. It is usually expressed in terms of a number distribution function *f(D)* that gives the number of particles of a given diameter *D*. The area under the curve is equal to 1 and the areas on both sides of the y axis are equal.

$$\frac{dN}{dD} = f(D) = \frac{1}{\sqrt{2\pi}s_n} exp\left[-\frac{1}{2s_n^2}(D-\bar{D})^2\right] \tag{2.10}$$

where s_n is the standard deviation, s_n^2 is the variance and $\bar{D}$ is the mean drop diameter.

The log-normal function is better approximating many particle size distributions that occur in nature. This function is equal to the Gaussian (normal) distribution above mentioned but the logarithm of the particle diameter is used as the variable.

$$\frac{dN}{dD} = f(D) = \frac{1}{\sqrt{2\pi s_n D}} exp\left[-\frac{1}{2s_n^2}(lnD - ln\bar{D})^2\right] \tag{2.11}$$

When the data fit this function, it means that the logarithm of the diameter is distributed normally. Log-normal distributions can also be written for surface and volume distributions as surface distribution (explained in detail in [17]).

The other functions proposed below are empirical functions. Each of them is valid under certain specific conditions that depend largely on the mechanism of disintegration involved.

Nukiyama and Tanasawa created a model that permits to fit experimental data that present more than one peak. Therefore, their function is suitable for those applications in which multipeaked distributions occur. In order to be able to show more than one peak, this function depends on four independent constants a, b, p and q.

$$\frac{dN}{dD} = aD^p exp - (bD)^q \tag{2.12}$$

Some simplifications can be applied thus reducing the four parameters to two.

The most widely used correlation is the Rosin-Rammler distribution (also known as Weibull distribution) whose expression is:

$$1 - Q = exp - \left(\frac{D}{X}\right)^q \tag{2.13}$$

where Q is the fraction of the total volume that is contained in drops whose diameter is lower than D, while X and q are constants. The exponent q provides a measure of the spread of drop sizes of the spray, the higher it is the more uniform the spray is (if q is equal to infinite the spray has all the droplets of the same size). A typical value for q is in the range between 1.5 and 4 but some rotary atomizers can reach a value of 7 [17]. The popularity of this function is mainly due to its simplicity and it permits to extrapolate very fine droplet sizes reaching those values where most of the time measurements are not accurate. It is possible to extrapolate q from the slope of the line of the usual Rosin-Rammler plot (Figure 2.11 a). The parameter X, which is a representative diameter of some kind, is given by the value of D for which

$$1 - Q = exp - 1 \tag{2.14}$$

whose solution is $Q = 0.632$. It means that the 63.2 % of the total liquid volume is composed by droplets whose diameter is lower than *X*.

A modified version of this distribution is given by Rizk and Lefebvre and it improves the quality of the fit of the previous function for the larger drop sizes (Figure 2.11 b). Its analytical expression is:

$$1 - Q = exp - \left(\frac{ln\, D}{ln\, X}\right)^{q} \tag{2.15}$$

As mentioned above, the main disadvantage of the Rosin-Rammler and modified Rosin-Rammler distributions is the inability to catch multiple peaks in the experimental data.

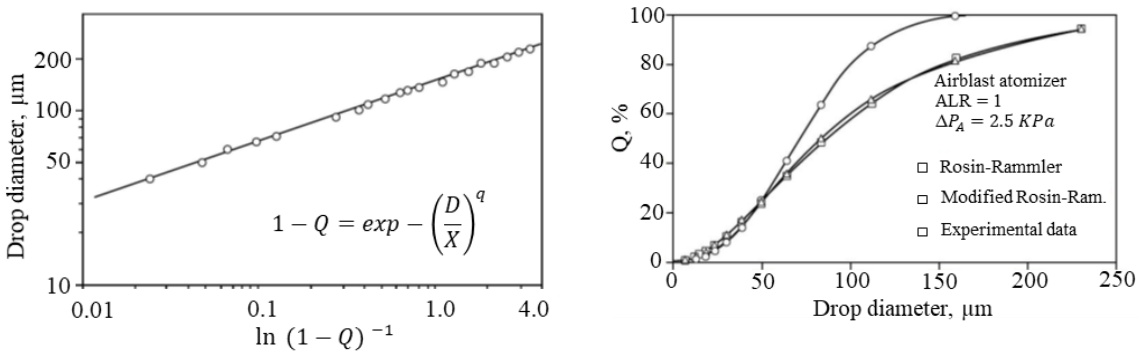

(a) (b)

Figure 2.11: Typical Rosin-Rammler (a). Modified Rosin-Rammler (b) [17].

The upper-limit function is a modified form of the log-probability equation that is based on the normal distribution function. The volume distribution equation is given by

$$\frac{dQ}{dy} = \delta exp \frac{-\delta^2 y^2}{\sqrt{\pi}} \tag{2.16}$$

where

$$y = ln \frac{aD}{D_m - D} \tag{2.17}$$

in which y goes from $-\infty$ to $+\infty$, so *D* goes from D_0 (minimum drop size) to D_m (maximum drop size), δ is related to the standard deviation of *D* and *a* is a dimensionless constant. The Sauter mean diameter (SMD) is given by

$$SMD = \frac{D_m}{1 + aexp\left(\frac{1}{4\delta^2}\right)} \tag{2.18}$$

that means that a reduction in δ implies a more uniform distribution.

The upper-limit distribution function considers a realistic spray of finite minimum and maximum drop sizes but it requires a difficult integration. The value of D_m must be assumed and usually many trials are necessary before finding a suitable value [17].

2.2.4 Mean diameters

In some fields of application, it is more convenient to deal only with mean or average diameters instead of the whole droplet size distribution in order to characterize the spray. Different mean diameters have been defined and each of them is suitable for a specific purpose. A general mathematical expression is the following one

$$D_{ab} = \left[\frac{\int_{D_0}^{D_m} D^a \left(\frac{dN}{dD}\right) dD}{\int_{D_0}^{D_m} \left(\frac{dN}{dD}\right) dD}\right]^{\frac{1}{a-b}} \tag{2.19}$$

where *a* and *b* can take any value depending on the studied effect and $a + b$ is called the order of the mean diameter. It may also be written, for disperse distribution

$$D_{ab} = \left[\frac{\sum N_i D_i^a}{\sum N_i D_i^b}\right]^{\frac{1}{a-b}} \tag{2.20}$$

where *i* indicates the size range considered, N_i is the number of drops in size range *i* and D_i is the middle diameter of size range *i.*

The principle mean diameters and their application are reported in the following table.

a	b	Symbol	Name of Mean Diameter	Application
1	0	D_{10}	Length	Comparisons
2	0	D_{20}	Surface area	Surface area controlling
3	0	D_{30}	Volume	Volume controlling, hydrology
2	1	D_{21}	Surface-area-length	Absorption
3	1	D_{31}	Volume-length	Evaporation, molecular, diffusion
3	2	D_{32}	Sauter mean diameter (SMD)	Mass transfer, reaction, combustion
4	3	D_{43}	De Brouckere or Herdan	Combustion equilibrium

Table 1: Mean diameters and their applications [17].

For the purpose of this work the SMD is largely used and compared among the tests since it is generally used for combustion processes. The physical meaning of the SMD is that it is equal to the diameter of a droplet whose ratio of volume to surface area is the same as that of the entire spray. Another explanation for the SMD is that it is simply the drop size at the mean of the droplet surface area distribution. Hence, it makes sense to adopt the SMD to investigate correlations that depend on surface area such as evaporation or combustion.

To fully represent a spray in these kind of applications a two-parameter function is sufficient. One of the two parameters is a representative diameter and the other one is a measure of the range drop sizes. Literature gives a list of typical representative diameters used to define distribution functions, here below a table is reported.

$\boldsymbol{D_{0.1}}$	Drop diameter such that 10 % of total liquid volume is in drops of smaller diameter.
$\boldsymbol{D_{0.5}}$	Drop diameter such that 50 % of total liquid volume is in drops of smaller diameter. This is the mass median diameter (MMD).
$\boldsymbol{D_{0.632}}$	Drop diameter such that 63.2 % of total liquid volume is in drops of smaller diameter. This is X in Rosin-Rammler function.
$\boldsymbol{D_{0.9}}$	Drop diameter such that 90 % of total liquid volume is in drops of smaller diameter.
$\boldsymbol{D_{0.999}}$	Drop diameter such that 99.9 % of total liquid volume is in drops of smaller diameter.
$\boldsymbol{D_{peak}}$	Value of D corresponding to peak of drop size frequency distribution curve.

Table 2: Typical representative diameters.

2.3 Basics of thermoacoustics

Sound consists of mechanical oscillations propagating in continua [36]. Within the aero-engine field, thermoacoustic waves are studied in their propagation in gaseous media (flue gases inside the combustor). The sound wave is responsible for modifying the properties of the flowing gas, such as its pressure, density or velocity.

Acoustic instabilities play an important role inside the combustion chambers of a jet engine (especially if the LPP concept is adopted) when pressure oscillations due to the released heat by the flame create a feedback loop with the inlet air velocity [1]. The following Figure 2.12 shows this feedback mechanism.

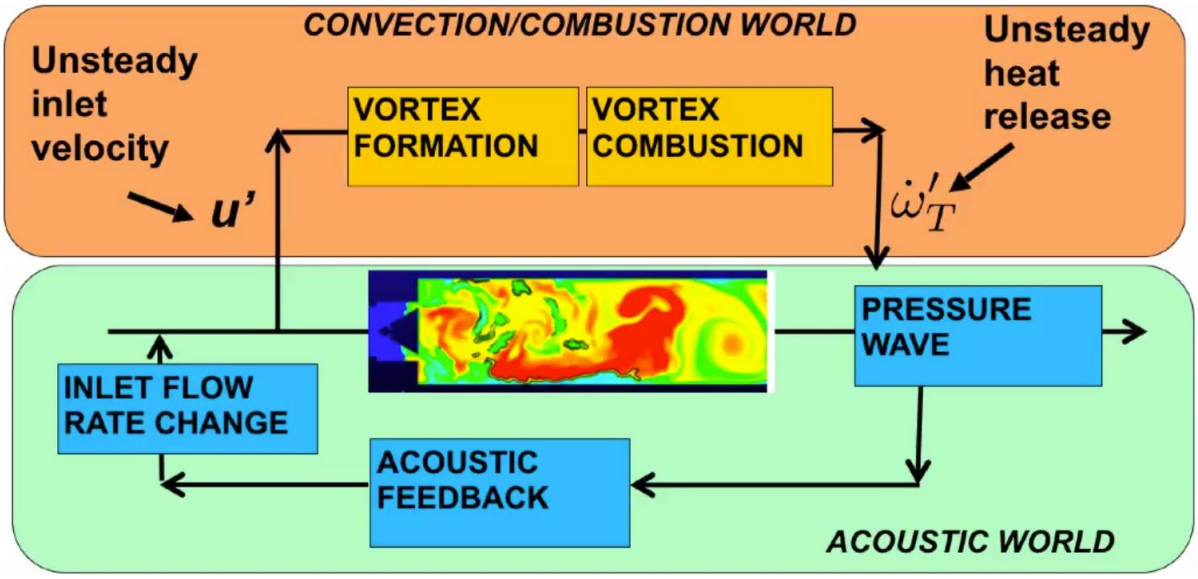

Figure 2.12: Feedback interaction between combustion and acoustic worlds.

The interaction between acoustic waves and heat release was studied by Rayleigh in 1878 [36] and the criterion he established can be expressed in mathematical terms by

$$\int_0^T \dot{\omega}'_T(t) \cdot p'(t)dt > 0 \tag{2.21}$$

where T is the period of the oscillation and p' and $\dot{\omega}'_T$ are the pressure and heat release oscillations. The instability criterion states that instabilities occur in the system when the product of the heat release and pressure perturbations is positive. This means that, inside one period, the instabilities grow when the unsteady pressure and the unsteady heat release are in the same phase in enough places in the combustor.

An unsteady combustion generates acoustic waves, which consequently alter the air and fuel flow rates thus modifying the ALR. At lean conditions, a change in the ALR strongly influences the combustion process and, furthermore, an oscillation in the ALR means that the atomization process is also influenced and thus NO_x emissions and soot formation appear.

The high pressure oscillations also carry a reduction in the mechanical components lifetime of the engines [3].

In this context, this work would like to analyse how these oscillations influence the generated spray characteristics by post-processing experimental data. The results are supposed to be helpful for future research on this field and to provide real numbers that could be needed to create a model that can simulate the studied phenomenon.

3 Test setup and measurement technology

3.1 Test rig description: general overview and layout

The schematic view of the test rig is showed in Figure 3.1.

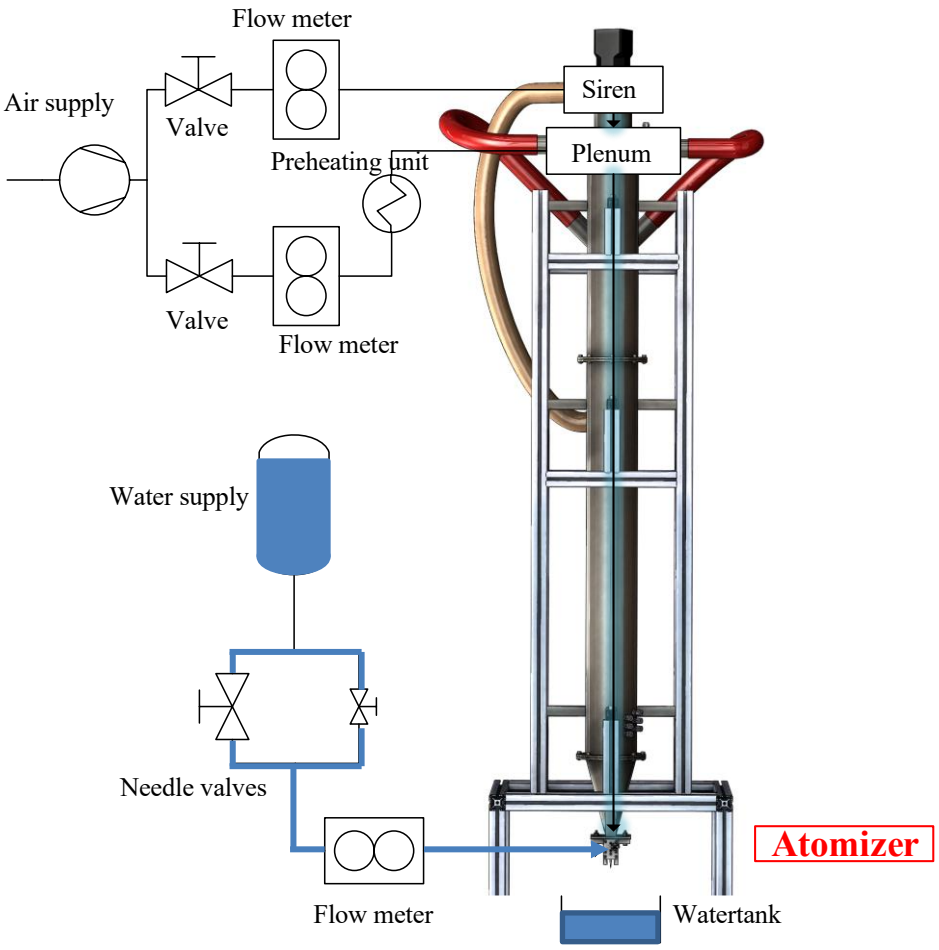

Figure 3.1: Schematic representation of the test rig.

The air is supplied from a compressor and is divided into two different channels: approximately 50 % passes through a siren and is excited at a certain frequency before being coaxially mixed with the rest of the air mass flow, which is bypassed through an air plenum. It is possible to adjust the air mass flow by acting on the valves while the flow meters validate the desired amount. After the mixing, the air flows in a 1.5 m resonance tube before reaching the airblast prefilmer nozzle

at atmospheric pressure. Thanks to the pressure sensor positioned just before the nozzle, it is possible to calculate the pressure drop across it. The liquid (water in the present work) is fed into the system from a pressurized vessel and is controlled by two independent needle valves. Finally, the water is collected in a tank after being atomized into spray at the prefilming airblast nozzle. For the test presented in section 4.1.4, in which the influence of temperature is investigated, a preheating unit was used to heat up the temperature of the air before entering in the plenum. A thermocouple placed just before the nozzle shows the exact value of temperature at the atomization edge, while the desired temperature is set with a PID controller and a thermocouple directly after the preheater for safety reasons.

Some practical operating ranges of the test rig are:

- Air-to-Liquid Ratio: $8 - 40$
- Pressure drop: $1 - 5\ \%$
- Forcing frequency: $0 - 800\ Hz$
- Preheating temperature: $50 - 200°C$

Two different measurement techniques were used for this work: hot wire Constant Temperature Anemometry (CTA) to measure the velocity of the air forced by the siren and the velocity of the air downstream of the atomization edge and Phase Doppler Anemometry (PDA) to determine the spray characteristics.

3.2 Airblast atomizer configuration

First of all it must be said that choosing to use a real airblast atomizer (Figure 3.3) would not be an admissible choice [37]. The primary disadvantage of this atomizer type is that the emerging spray is optically inaccessible to image based diagnostic techniques since the spray has the shape of a hollow cone, thus each optical path intersects the spray twice. As solution, the geometry has been transformed into a planar prefilming surface inside a rectangular duct. The similitude between the two typologies of atomizers is shown in Figure 3.2. The wide aspect of the rectangular duct guarantees that no interfering corner vortices create. It also provides a 2-dimensional airflow in the measurement volume, thus neglecting the swirl motion [37].

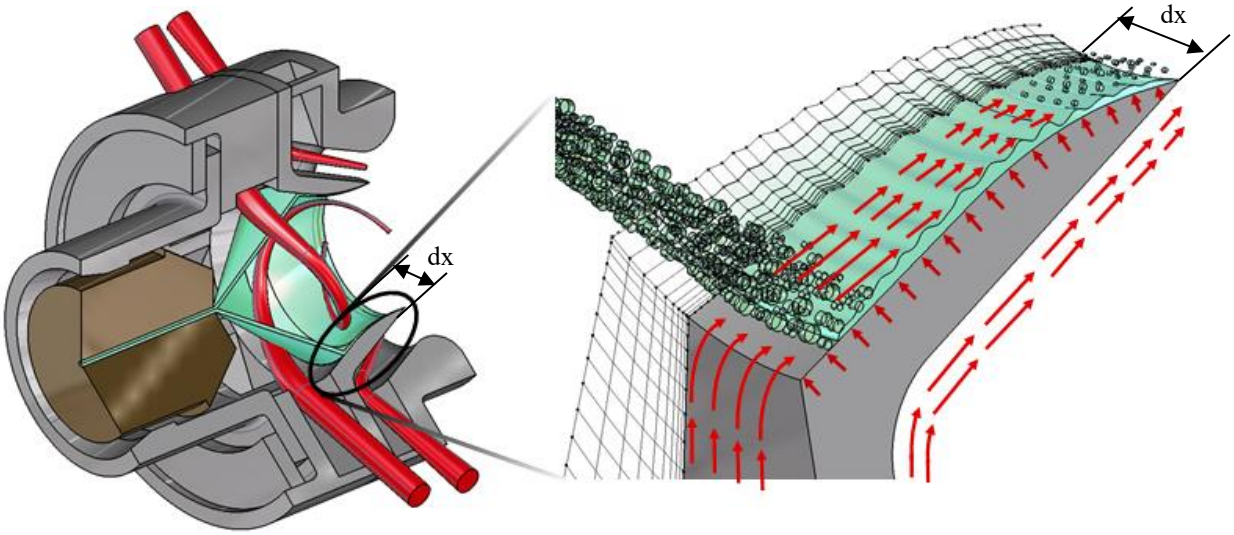

Figure 3.2: Comparison of model atomizer with typical airblast atomizer [38].

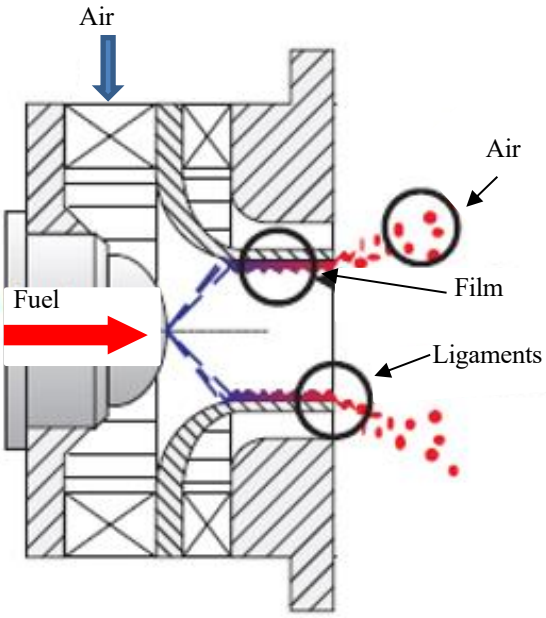

Figure 3.3: Cut through a real airblast atomizer [37].

The three-dimensional representation of the used airblast atomizer is shown in cut sections in Figure 3.4.

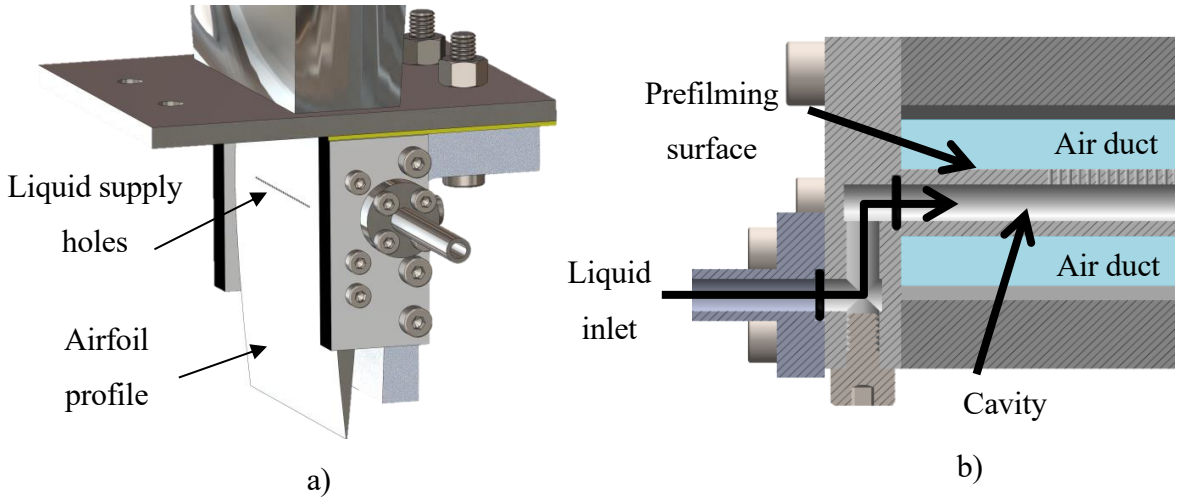

Figure 3.4: Scheme of the prefilming airblast atomizer.

It consists of a standardized symmetrical airfoil profile made of stainless steel (NACA-0010) with a chord length of 73 mm and an atomizing lip thickness of about 200 µm. The cavity on the inside of the airfoil hosts the liquid (Figure 3.4 b), which then exits through 40 equidistant holes on the surface of the prefilmer (Figure 3.4 a), creating a uniform liquid film. The water is entering the cavity on the inside of the prefilmer symmetrically from the two sides before it reaches the surface flowing through the 40 holes. The air flows on both sides of the prefilming atomizer, while the liquid film covers only one side, thus reproducing the prefilm surface of a conventional airblast atomizer. The measured effective area of the nozzle is 1026 mm^2.

3.3 Pulsating flow generator

The siren is used for the air excitation with possible frequencies up to 800 Hz. It was designed and manufactured at the Technical University of Munich [39]. The main components of it are an internal rotating disc attached to a motor whose speed is controlled by computer software and a fixed housing. The rotor has eight openings while the fixed housing has four openings (Figure 3.5): during the rotation of the rotor, when the openings of the two components coincide, the

airflow can pass through, otherwise it is interrupted. Therefore, the air flows at forced frequency, which is linearly dependent on the rotational speed of the siren rotor:

$$f = \frac{8}{60} n \tag{3.1}$$

where f is the frequency in Hz at which the air is allowed to pass through and n the rotational speed of the motor in RPM, regulated by software.

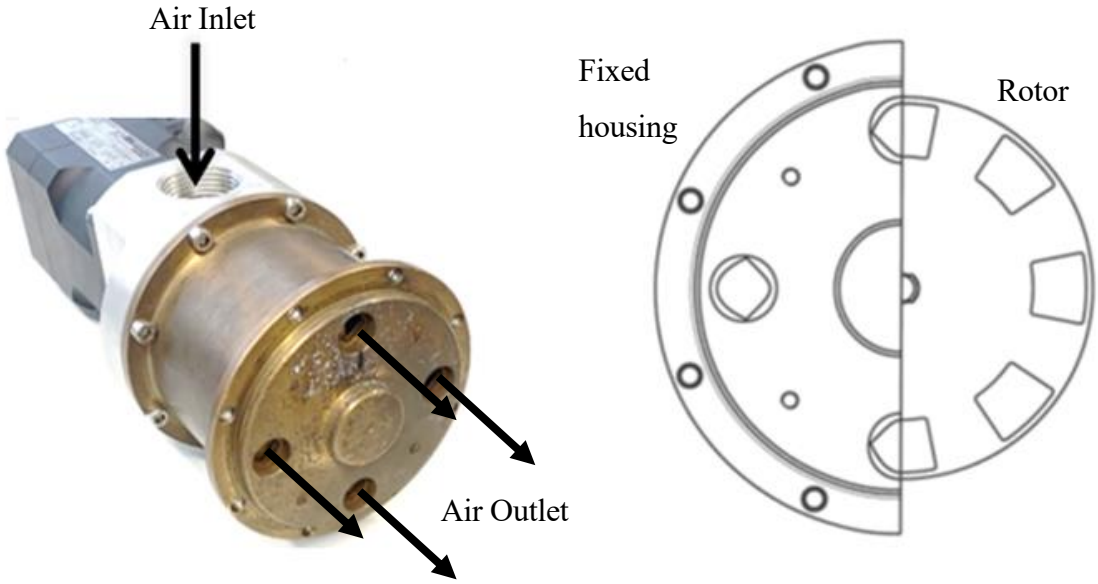

Figure 3.5: Frontal section of the rotor and fixed housing.

3.4 Hot wire constant temperature anemometry (CTA)

Since the end of the sixties, hot wire anemometry is one of the most common methods used to measure instantaneous fluid velocity [40]. The technique depends on the convective heat loss to the surrounding fluid from an electrically heated sensing element or probe. In the method of Constant Temperature Anemometry (CTA), the electrical resistance of the sensor is kept constant automatically through the agency of a feedback arrangement (Figure 3.6). Hence, the temperature of the wire remains constant even when there is heat transfer into the flow. Therefore, it is possible to determine the airflow velocity with very high accuracy. Due to the high temporal resolution, turbulence parameters can also be determined.

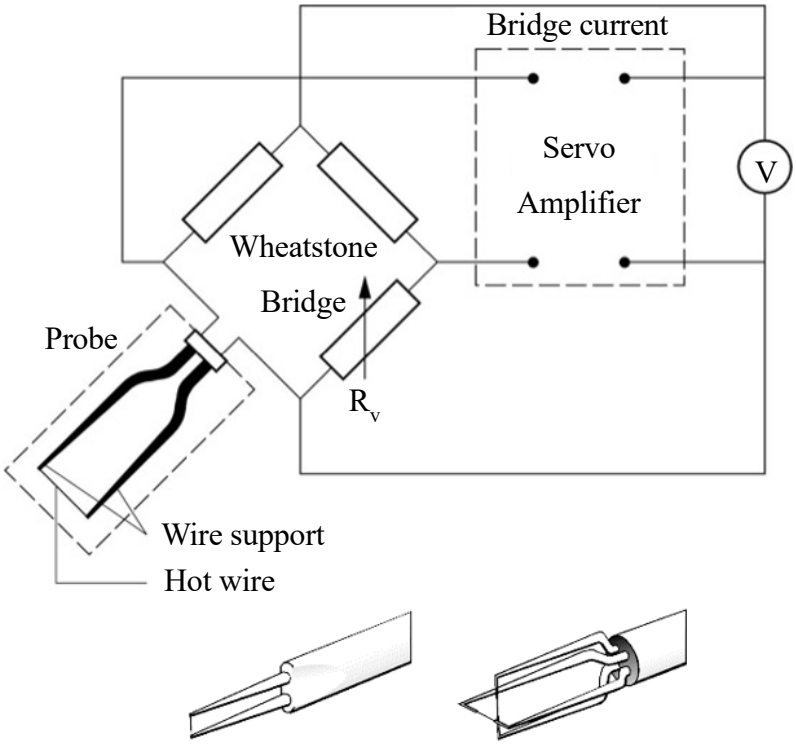

Figure 3.6: Circuit representation of CTA.

In order to measure with the CTA hot wire technique, a calibration of the probe is needed for the software to correlate the bridge voltage to the air velocity. Placing the probe in a well-defined airflow for a variety of air velocities, the known velocity is matched with the voltage that the probe senses. The resulting calibration curve should follow a non-linear trend and can be approximated by the King's Law, given in the following equation

$$E^2 = A + B \times U^n \tag{3.2}$$

In which:

- E: bridge voltage [V]
- U: Air Velocity [m/s]
- A, B, n: parameters

Important to notice is that more calibration points are needed for low velocities since the curve has a steeper angle there.

When the calibration of a probe is finished, it can be used in the desired application if the expected airflow velocities are within the range of the velocities used for the calibration. After the probe is

inserted in an unknown airflow, the bridge voltage that is measured can be translated in air velocity using the King's Law

$$U = \sqrt[n]{\frac{E^2 - A}{B}} \tag{3.3}$$

3.5 Phase Doppler Anemometry (PDA)

Phase Doppler Anemometry (PDA) is a non-invasive optical measuring method for simultaneous measurements of droplet diameter and velocity. The crossing of laser beams originating from a sender optic create an interference pattern of fringes with a determined distance among them, which generate the measurement volume. The underlying principle of PDA is based on light-scattering interferometry and therefore does not require any calibration.

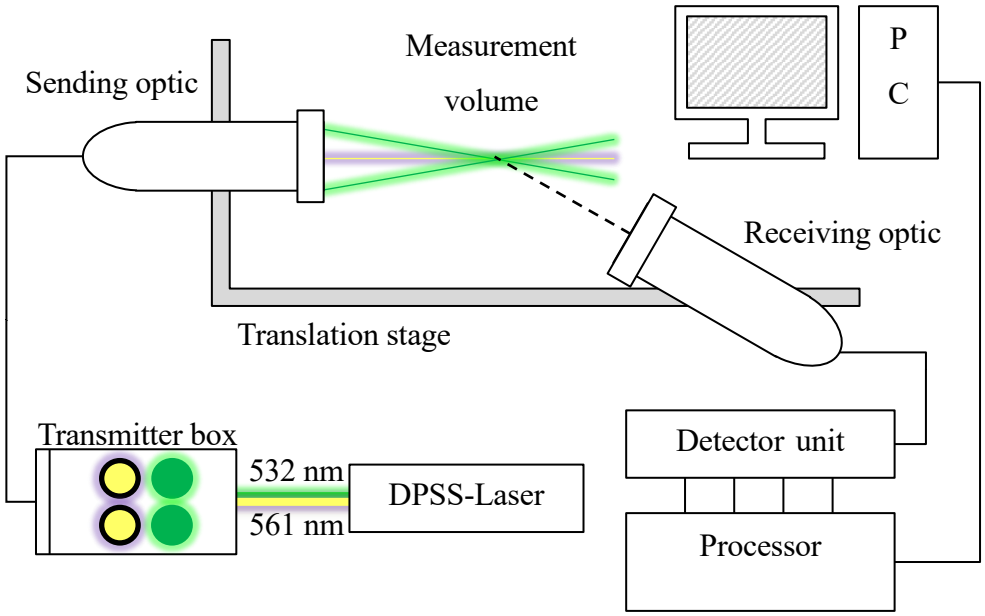

Figure 3.7: Schematic representation of PDA.

Particles crossing the measurement volume scatter light and a receiving optic placed at a well-determined off-axis location collects a portion of the scattered light in three detectors. Each detector converts the optical signal into a Doppler burst with a frequency linearly proportional to the particle's velocity. The phase shift between the Doppler signals from the three different detectors is a direct measure of the particle's diameter.

The phenomena of light scattering can be visualised by ray tracing. For example, the light which is incident on a water droplet moving in a medium is partially reflected from the surface and

partially transmitted and refracted in both forward and backward directions after one internal reflection. The scattered light intensity is not uniform in all directions and depends on the relative refractive index between the droplet and the medium. Therefore, the position of the receiver should be carefully considered, in order to make one light scattering mode dominant.

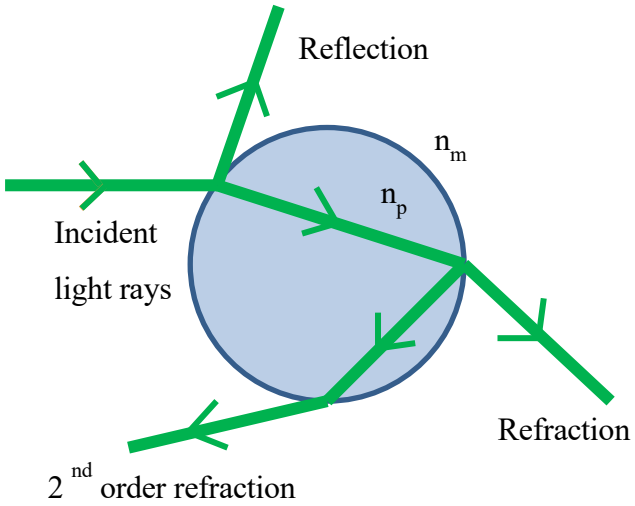

Figure 3.8: Light scattering through a water droplet.

3.5.1 Velocity measurement

The basic outcome of this technique is the measurement of the velocities of the droplets in a spray.

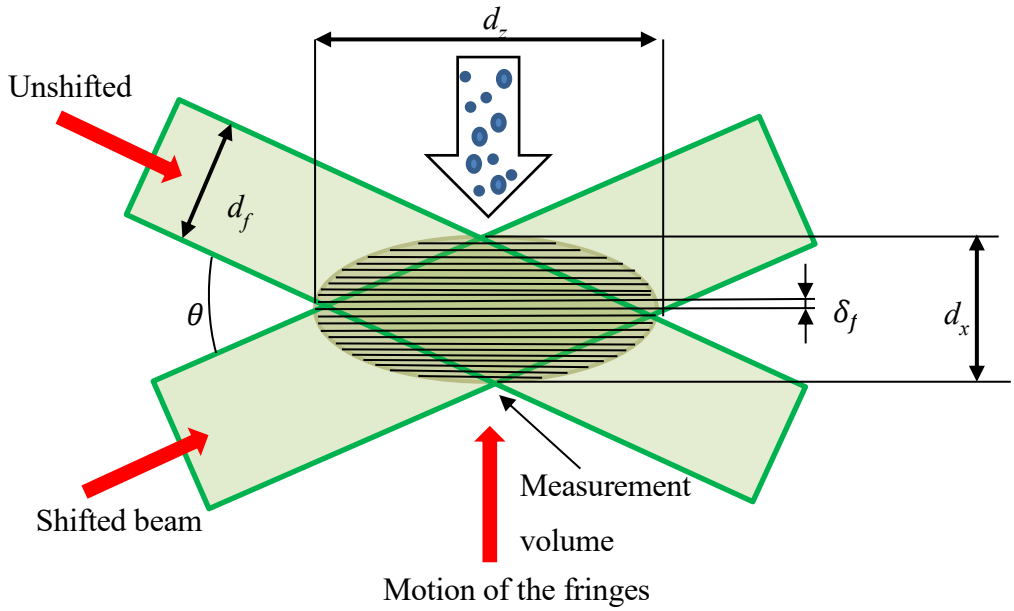

Figure 3.9: Interference volume created by the two laser beams.

Considering the measurement volume created by the intersection of the two laser beams as shown in Figure 3.9, a particle passing through it with a velocity U perpendicular to the interference plane needs the time T to travel the distance δ_f. The fringe distance, δ_f, is determined as

$$\delta_f = \frac{\lambda}{2 \cdot sin\left(\frac{\theta}{2}\right)} \tag{3.4}$$

and the velocity can be therefore calculated as follows

$$U = \frac{\delta f}{T} = \frac{\lambda}{2 \cdot sin\left(\frac{\theta}{2}\right)} \cdot f_D \tag{3.5}$$

where f_D is the Doppler frequency associated with the time *T*. As the particle passes through the measurement volume, the light of the two interfering laser beams is scattered due to refraction and reflection phenomena and its original frequency changes proportionally according to the droplet velocity U. The two laser beams undergo a frequency shift that has the same absolute value but opposite sign, since the perpendicular components of the lasers' light have opposite direction (blue arrows in Figure 3.10). The decisive factor for the velocity measurement is that the Doppler frequency shift Δf_{Dop} is identical to the frequency f_D that is required to calculate the droplet velocity.

$$\Delta f_{Dop} = f_D \tag{3.6}$$

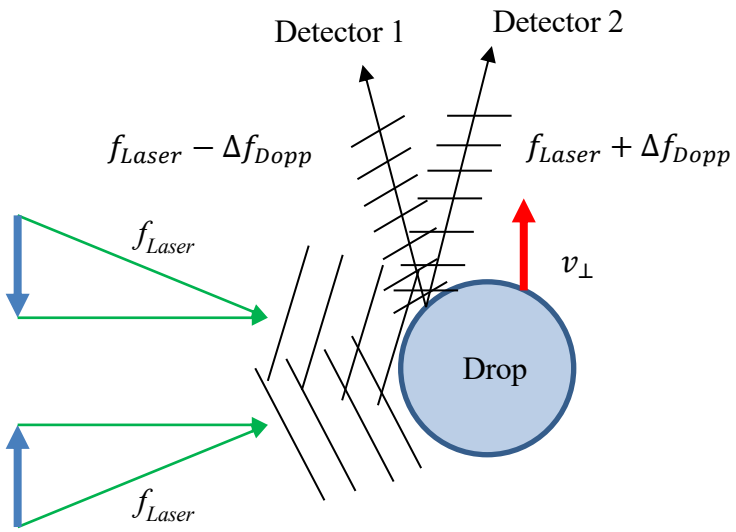

Figure 3.10: Laser beam frequencies before and after the interference with the droplet with velocity component U.

One detector will therefore measure the frequency $f_{Laser} + \Delta f_{Dop}$ while the other will measure the frequency $f_{Laser} - \Delta f_{Dop}$. Since $f_{Laser} \gg \Delta f_{Dop}$ and considering that interference of the two scattered laser beams happens at the receiving optics, a beat is generated. A beat is a wave created by superimposing two waves whose frequencies slightly differ. It is calculated in the following way

$$f_{beat} = \frac{1}{2}\left[\left(f_{Laser} + \Delta f_{Dop}\right) + \left(f_{Laser} - \Delta f_{Dop}\right)\right] = f_{Laser} \tag{3.7}$$

The information of interest regarding the Doppler frequency shift Δf_{Dop} can be obtained by calculating the halved difference of the original frequency

$$f_{Amplitude\_modulated} = \frac{1}{2}\left[\left(f_{Laser} + \Delta f_{Dop}\right) - \left(f_{Laser} - \Delta f_{Dop}\right)\right] = \Delta f_{Dop} \tag{3.8}$$

This means that the PDA device, that is connected to the receiving optics, must be able to detect the frequency f_D from (3.8) and (3.6), and with this data it can elaborate the *U* component of the velocity, according to (3.5). Furthermore, the direction in which the droplets cross the measurement volume must be detected. For this purpose, a positive direction in the BSA software is imposed (fringe movement direction). The fringe direction setting affects the sign of the phase factors but not the Doppler frequency. Therefore, the direction of fringe motion affects the measurement of diameter but not the velocity measurement. If the fringe direction is incorrect, the phase of most of the detected particles will be outside the tolerance band [41].

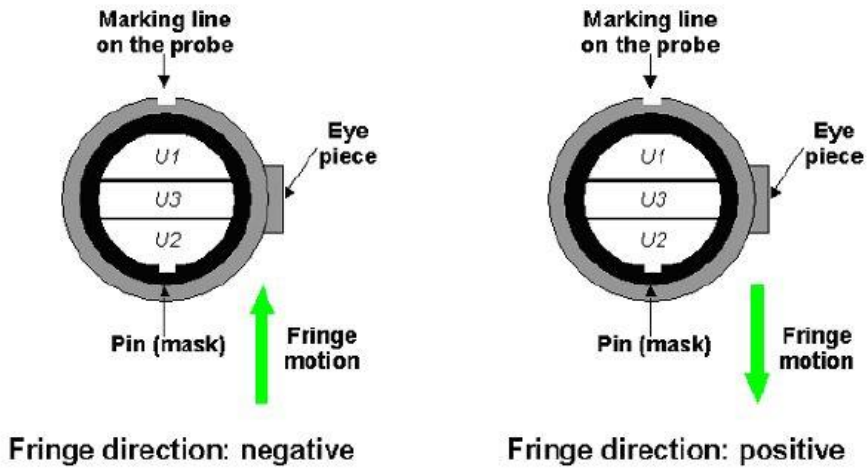

Figure 3.11: Fringe direction settings for the Dual PDA (front view) [41].

Due to the symmetry of the measurement volume and considering that the scattered laser beams have the same frequency shift it is not possible to understand in which verse the spray droplets move. To overcome this problem, one laser beam undergoes a frequency shift of $f_0 = 40\ MHz$. This frequency adjustment is performed by a Bragg cell, which is placed in the transmitter box of the PDA system (Figure 3.7). In Figure 3.12 it is possible to see which is the relation between f_D and the particle velocity component U: in Figure 3.12 a) it is clear that without the use of the Bragg cell the same frequency f_D is obtained for the same absolute value of the velocity, so it is not possible to detect the direction of the droplet. In Figure 3.12 b), with the Bragg cell, a frequency shift $f_0 = 40\ MHz$ is applied and in this case, for the same absolute value of the velocity but opposite sign, the detected frequencies will be different. Furthermore, we will observe a null velocity value when the detected frequency is $f_D = f_0 = 40\ MHz$.

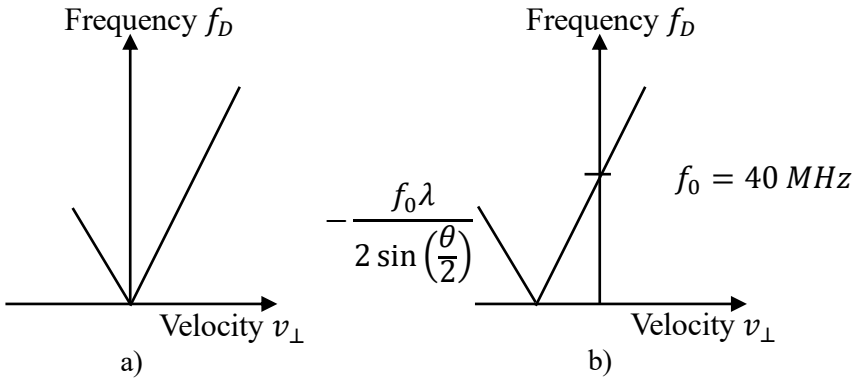

Figure 3.12: Frequency output as a function of droplet velocity component U. a) without Bragg cell b) with Bragg cell.

3.5.2 Diameter measurement

With PDA system, it is possible to detect particle diameters from approximately 0.5 µm to some millimetres. While for velocity detection just one photodetector is required, for diameter detection two of them are required. These two spatially separated photodetectors receive the signals generated by a particle floating in the measuring volume with a time offset. This time offset is responsible for a phase shift Φ between the two received detector signals. The important factor for the determination of the diameter is that a linear relation exists between the phase shift Φ and the particle diameter D

$$\Phi = \frac{2\pi D}{\lambda} \cdot \beta \tag{3.9}$$

The phase difference gives information about the curvature of the droplet at a particular point in its surface. With two pairs of detectors and if the particle is spherical, the measured curvature in two different points in its surface must be identical. A problem can anyway occur when the phase difference exceeds 2π because, as it is showed in Figure 3.13, diameter can no longer be precisely assigned if only two detectors *U1* and *U2* are used. By adding a third detector *U3* which is much closer to detector *U1* it is possible to obtain a wider range for the diameter determination but with a lower accuracy (the steepness of the phase-diameter relation is lower).

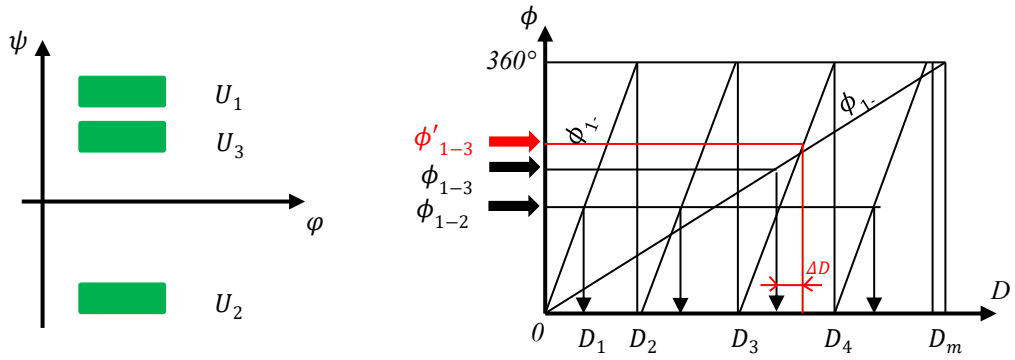

Figure 3.13: Problem and solution for a phase shift bigger than 2π.

Inside the phase-diameter relation (3.9), the factor β appears as well. It is a geometric factor and is function of the intersection angle θ between the two laser beams and the azimuth angle ψ, which is the angle between a photodetector and the YZ plane as shown in Figure 3.14.

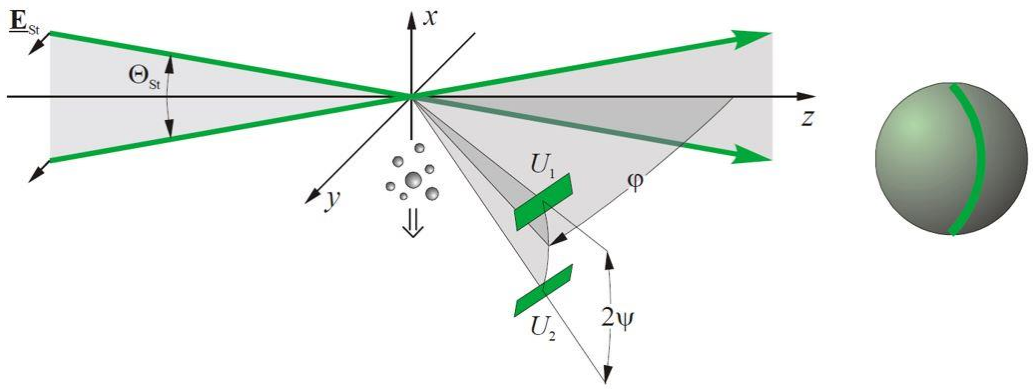

Figure 3.14: Beam crossing angle θ, azimuth or elevation angle ψ and scattering angle φ.

If reflection is used as the scattering mode, the following formula applies

$$\beta = \frac{sin\,\theta\,sin\,\psi}{\sqrt{2(1 - cos\,\theta\,cos\,\psi\,cos\,\varphi)}} \tag{3.10}$$

If refraction is the dominant scattering mode, then

$$\beta = \frac{-m\,sin\,\theta\,sin\,\psi}{2(1 + cos\,\theta\,cos\,\psi\,cos\,\varphi)\left(1 + m^2 - m\sqrt{2(1 - cos\,\theta\,cos\,\psi\,cos\,\varphi)}\right)} \tag{3.11}$$

in which $m = \frac{n_p}{n_m}$ is the relative refractive index between the two mediums, while n_p and n_m are the absolute refractive indices of the scattered particle and of the surrounding medium respectively. For the purpose of this study it is required to have first order refraction over reflection as dominant scattering mode since the intensities given by reflection and distributed over the entire scattering angle are too small to ensure a sufficient signal-to-noise ratio (SNR). This ratio should always remain high, especially where there is a high density of droplets, in order to always obtain a good quality signal. As concerns the scattering angle φ, for Fiber PDA it is usually $\varphi = 30°$, so refraction over reflection is guaranteed and the intensity of the generated signals is high enough to ensure a favourable SNR.

3.5.3 Measurement volume

The measuring volume should be as small as possible in order to avoid multiple drops inside of it simultaneously (when this happens there are measurement errors due to the slit and trajectory effect). The dimensions of the measuring volume shown in Figure 3.9 are explained as follows.

- *Fringe spacing* δ_f: it is the distance between the individual interference fringes. It depends on the wavelength of the laser and the beam intersection angle.

$$\delta_f = \frac{\lambda}{2 \cdot sin\,\theta} \tag{3.12}$$

- *Diameter of the focused laser beam* d_f*:* it is a function of the focal length *f*, the laser wavelength λ, the laser beam diameter when coupled in the transmitter box d_1 and the beam expansion factor *E*.

$$d_f = \frac{4}{\pi \cdot f \cdot E \cdot d_1} \tag{3.13}$$

- *Measurement volume dimensions (*Figure 3.9*):*

$$d_x = d_f \tag{3.14}$$

$$d_y = \frac{d_f}{cos\left(\frac{\theta}{2}\right)} \tag{3.15}$$

$$d_z = \frac{d_f}{cos\left(\frac{\theta}{2}\right)} \tag{3.16}$$

$$Volume = \frac{\pi}{3 \cdot d_f^3 \cdot sin(\theta)} \tag{3.17}$$

3.5.4 Volume and mass flux calculation

In order to be detected by the photomultiplier, a particle of a given size passing through the measuring volume should scatter sufficient light. Since this cannot be achieved in the whole theoretical measurement volume (Gaussian shape of the light intensity), an effective measuring volume is defined. What really matters is the definition of the cross sectional areas; for example, the cross sectional area in the YZ plane (green in Figure 3.15) is represented in the following figure and it mainly depends in three parameters: laser beam width, scattering angle φ and slit width of the photodetector.

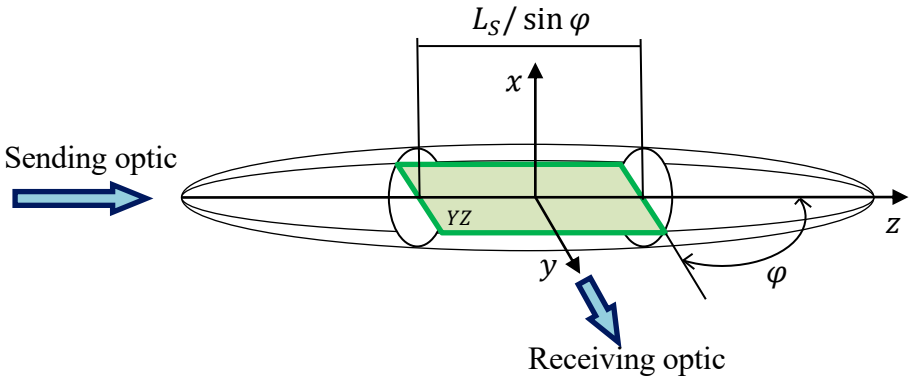

Figure 3.15: YZ cross sectional area, function of *Ls*, φ and laser beam width.

However, three other factors are also important: particle diameter, trajectory and validation criteria.

- *Dependence on particle size*

According to the algorithm proposed by Saffman [42], the cross sectional area is calculated as a function of an effective measurement volume diameter d_e, which is dependent on particle sizes d_K, Knowing this quantity, the cross sectional areas depicted in Figure 3.15 are defined by the relations:

$$A_x(d_K) = \frac{d_e(d_K) \cdot L_s}{sin\,\varphi} \tag{3.18}$$

$$A_y(d_K) = \frac{d_e(d_K) \cdot L_s}{sin\,\varphi} + \frac{\pi}{4} \cdot d_e^2 \cdot cot\,\varphi \tag{3.19}$$

- *Dependence on trajectory*

In particle size, concentration or mass flow measurement, the number of detected particles is always measured in relation to a reference cross sectional area. For particles moving in the X or Y direction (Figure 3.15), these reference areas are A_x and A_y respectively. However, if the particles have a different trajectory within the XY plane, then the properties must take into account just the component perpendicular to the X or Y-axis so new effective areas must be considered, according to the following formulas:

$$A'_x = \frac{A_x}{cos\,\gamma} \tag{3.20}$$

$$A'_y = \frac{A_y}{sin\,\gamma} \tag{3.21}$$

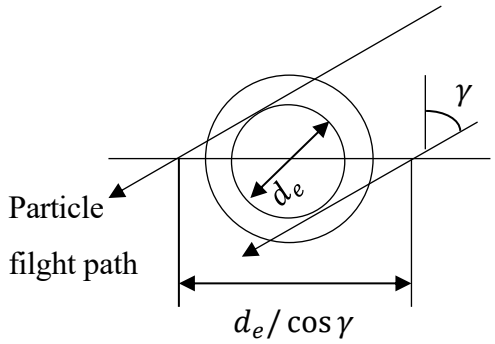

Figure 3.16: Effective cross sectional area perpendicular to the X axis.

- *Dependence on validation criteria*

The reduction of detected particles is dependent on the particle size, the refractive index and the particle trajectory. The reference detection range is influenced by the validation procedure in the Fiber PDA. In order to reduce the probability to have multiple droplets together inside the measuring volume a limit along the axial direction is imposed to the detector by using a slit of a proper length. Therefore, the volume flow can be calculated separately for each velocity component:

$$f_{vx} = \frac{\pi}{6\Delta t} \sum_{i=1}^{n_i} \frac{d_i^3 \cos \gamma_i}{A_x(D_K)} \tag{3.22}$$

$$f_{vy} = \frac{\pi}{6\Delta t} \sum_{i=1}^{n_i} \frac{d_i^3 \sin(\gamma_i)}{A_y(D_K)} \tag{3.23}$$

where d_i and γ_i are the diameter and trajectory of the individual particles for the reference range A_K of the respective size class. From (3.22) and (3.23) it is possible to derive the mass flux multiplying them by the density of the liquid.

$$\dot{m}'_x = f_{vx} \cdot \rho_l \tag{3.24}$$

$$\dot{m}'_y = f_{vy} \cdot \rho_l \tag{3.25}$$

3.5.5 PDA system configuration

The setup employed for accomplishing measurements regarding the research activities of this dissertation was a Fiber PDA system from Dantec Dynamics. This PDA system was utilized to measure two droplet velocity components as well as the droplet diameter (2D Fiber PDA). For this purpose, a diode-pumped solid-state laser (DPSS) was used providing laser beams of two wavelengths (2x150mW):

1. Green (532 nm): used to detect the droplets velocity in the direction parallel to the flow. This is the main component of the droplets velocity since the droplets move mainly in the axis of the flow.
2. Yellow (561 nm): used to detect the component of the droplet velocity in the direction perpendicular to the main velocity component.

A schematic representation of the aforementioned PDA system is illustrated in Figure 3.7.

A laser power optimization is required in order to not stress excessively the optical fiber cables, but also because enough power is needed at the exit of the sending optic in order to receive proper signal.

Figure 3.17: Cables that link the manipulators of the transmitter box to the sender.

A laser power meter (COHERENT FieldMaxII-TOP™) was used in order to optimize the laser power at the exit of each of the manipulators attached on the transmitter box, as well as at the exit of the sending optic.

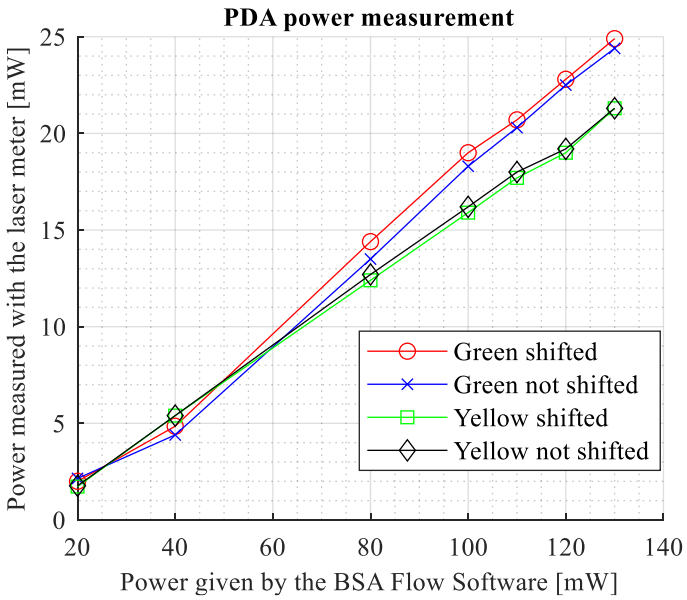

Figure 3.18: PDA power measurement.

After the end of the optimization process, the final output power of each of the four laser beams is displayed in Figure 3.18 as a function of the set laser power controlled in the software. A correspondence between the power of two beams of the same colour is also achieved.

4 Results and discussion

4.1 Steady airflow tests

During the execution of these tests, the motor of the siren is kept closed and the whole amount of air is forced to pass through the bypass plenum (see Figure 3.1). The air supply, and thus the resulting velocity profile of the air has a constant value during the entire measurement period.

For all tests in this subsection, the following parameters were settled up in the test rig:

- Laser set power: 110 mW;
- Water mass flow rate: $\dot{m}_{water} = 12$ kg/h;

4.1.1 XZ plane – horizontal and vertical investigation

For this first test the target was to assess how the spray characteristics are affected by the different positions at which it was measured. The 44 points were positioned in a way that permits to evaluate these properties along two main directions, horizontal and vertical, below the atomization edge. The following Figure 4.1 shows where the measurements were performed (positions mentioned in mm).

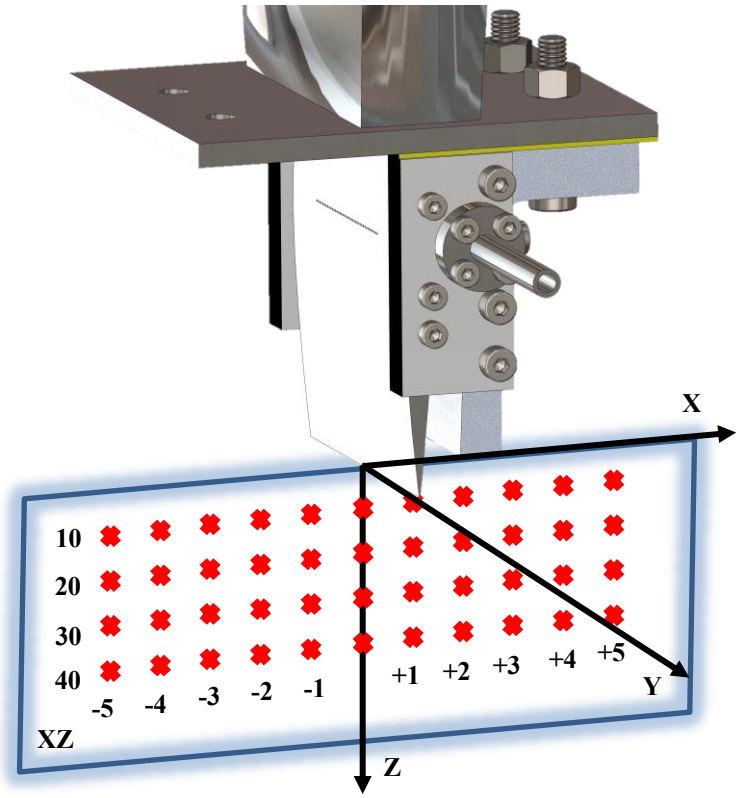

Figure 4.1: Measurement positions for the XZ plane scan, at Y = 0 mm.

The following parameters were chosen and fixed in the test rig:

- Pressure drop across the nozzle: $\Delta p_{nozzle} = 31.33$ mbar;
- Air mass flow rate across the nozzle: $\dot{m}_{air,nozzle} = 245.86$ kg/h.

or respectively:

- Pressure drop in percentage: $(\Delta p/p)_{nozzle}(\%) = 3\ \%$;
- $ALR = 20.49$.

The results are reported in the following diagrams. For the different studied spray properties, the comparison between the four different Z positions is reported.

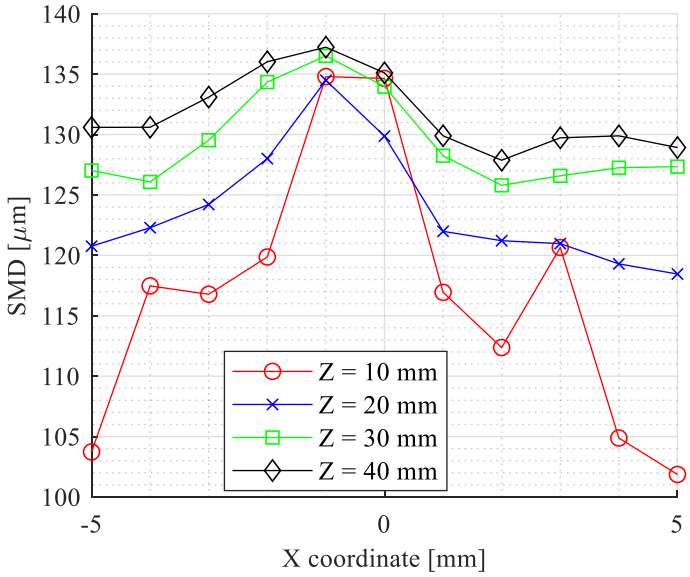

Figure 4.2: SMD, for the XZ scan.

Starting with the Sauter Mean Diameter of the spray, it is possible to notice that for the four different vertical positions there is a local maximum that seems to stay always in the horizontal interval of two millimeters around the central position, below the atomization edge. Moving away from the center on the X-axis, the SMD seems to spread and stay almost constant further away from the nozzle, while it keeps decreasing closer to the nozzle.

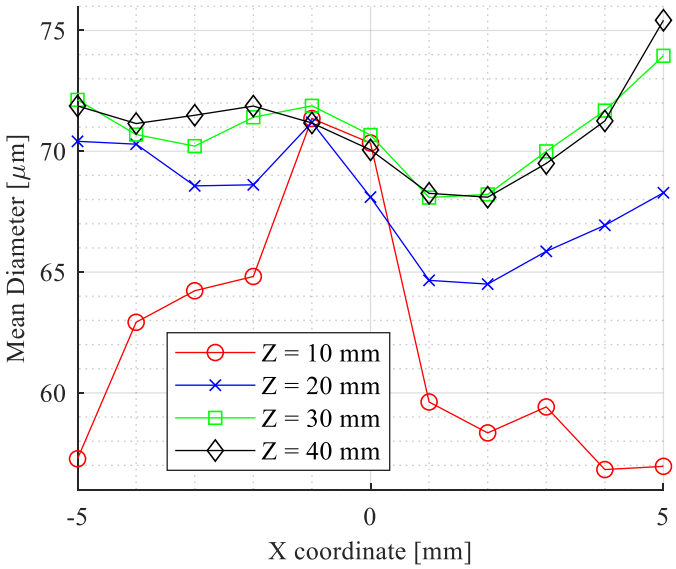

Figure 4.3: Mean Diameter, for the XZ scan.

For the mean diameter, the shape of the diagrams is obviously similar to the SMD diagrams but in this case the path tends to increase again at the extremes of the horizontal scan, for $X = \pm 5$ mm when moving at distances far from the nozzle. Only for $Z = 10$ mm this increase is not happening. This trend of the mean diameter makes sense, if one analyzes the number of small droplets (for example droplets with diameter lower than 25 µm) that are present inside the total number of droplets. The ratio between small droplets and total number of droplets is shown in Figure 4.4.

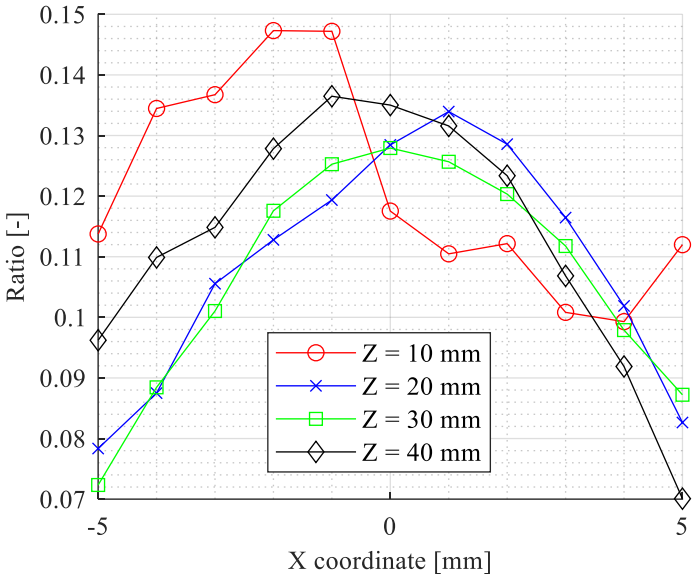

Figure 4.4: Ratio between number of small droplets and total number of droplets.

Since at the extremes of the interval the ratio tends to decrease, a higher number of bigger droplets (diameter bigger than 25 µm) will be present there, resulting in an increase of the mean diameter.

This difference is also justified by observing the droplet diameter distribution in Figure 4.5.

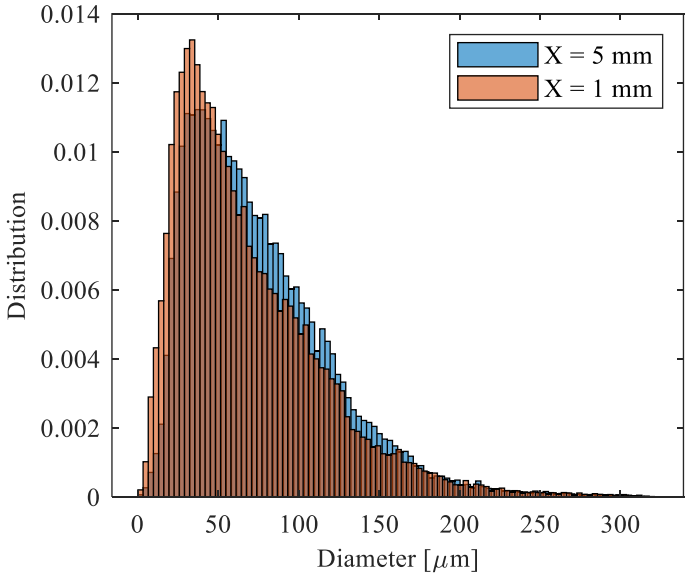

Figure 4.5: Droplet diameter distribution, at Z = 40 mm.

A probability density function displays how often the specific property (in this case the droplet diameter) appears in the measured spray. In this case, it shows how many droplets (in percentage of the total spray) have the particular diameter.

The positions at $X = 5$ mm and $X = 1$ mm for $Z = 40$ mm are selected for further investigation because they present similar SMD and quite different mean diameter (Figure 4.2 and Figure 4.3). From the histograms, it is clear to notice that the average mean diameter is higher at the position $X = 5$ mm (blue distribution), since the peak of the distribution is shorter and shifted slightly to the right. As concerns the SMD, generally it is strongly influenced by the big diameters of the smaller amount of droplets represented in the right part of the histogram; since the two shown distributions are very similar for increasing diameters (the columns of the histograms tend to overlap in that region), the resulting SMD is similar for both cases.

After investigating the size characteristics of the spray, the behaviour of the droplet velocities needed to be examined. Since the experiments were conducted with a 2D Fiber PDA system, a two velocity components analysis took place.

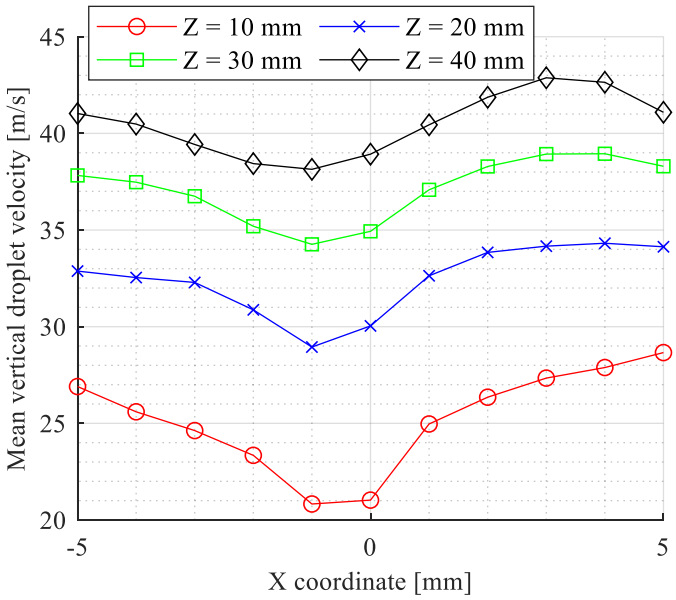

Figure 4.6: Mean vertical droplet velocity, for the XZ scan.

The mean vertical droplet velocity (along the Z-axis) shown in Figure 4.6 is inversely proportional to the Sauter Mean Diameter, so a local minimum appears slightly left to the central axis. For increasing Z values, so for higher distances from the atomization edge, the average velocity value increases. This was expected, since the droplets have more available distance to accelerate due to the drag force of the airflow.

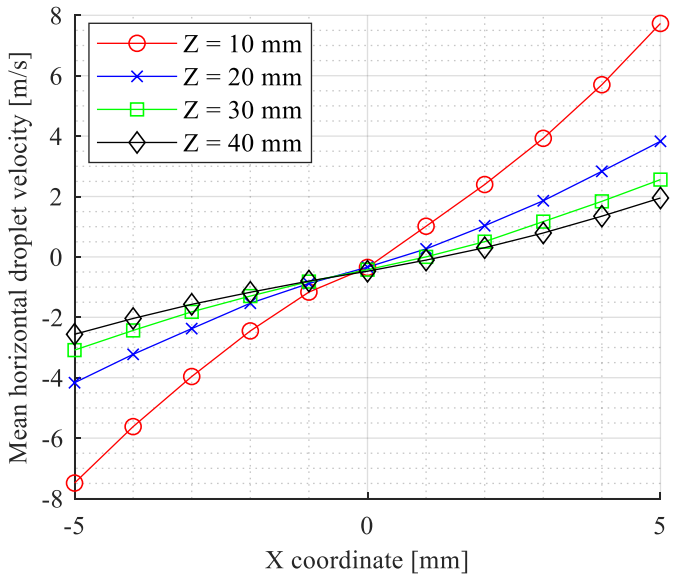

Figure 4.7: Mean horizontal droplets velocity, for the XZ scan.

As it was also expected, exactly below the atomization edge, for $X = 0$ mm, the absolute droplet velocity is mainly consisted of the vertical component, so for each different vertical position the mean horizontal droplet velocity (Figure 4.7) is close to zero. Furthermore, it makes sense that the mean horizontal velocity increases (as an absolute value) symmetrically towards the extremes of the interval.

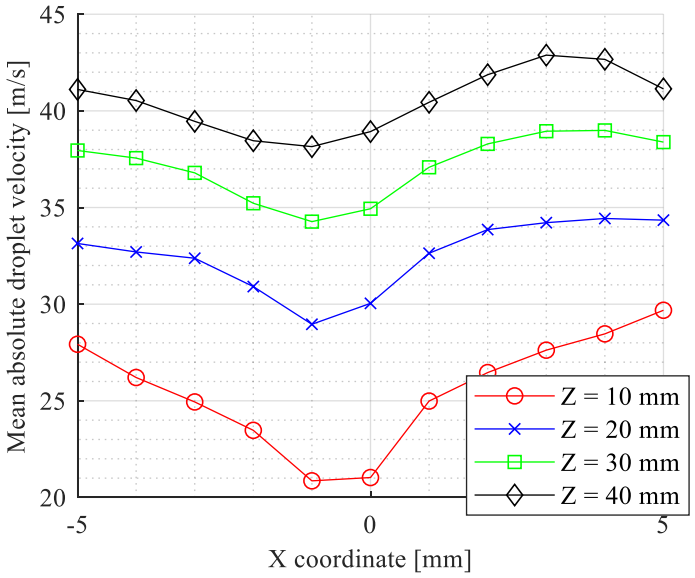

Figure 4.8: Mean Absolute droplets velocity, for the XZ scan.

The mean absolute droplet velocity (Figure 4.8) follows the same trend as the vertical velocity since it is the main component and the horizontal one has not a great impact on it. In Figure 4.9, the angle between the absolute velocity vector and the Z direction is represented. Moving away from the atomization edge, the vertical velocity component becomes dominant with respect to the horizontal one, so the angle is reducing.

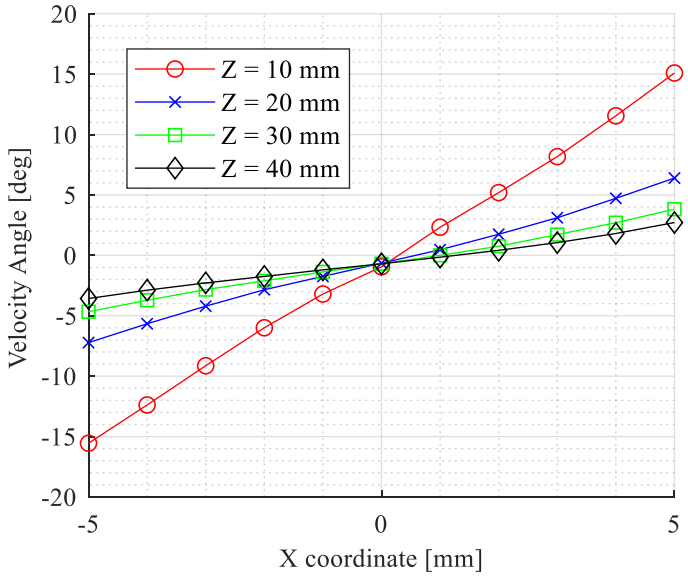

Figure 4.9: Angle between absolute velocity vector and Z direction, for the XZ scan.

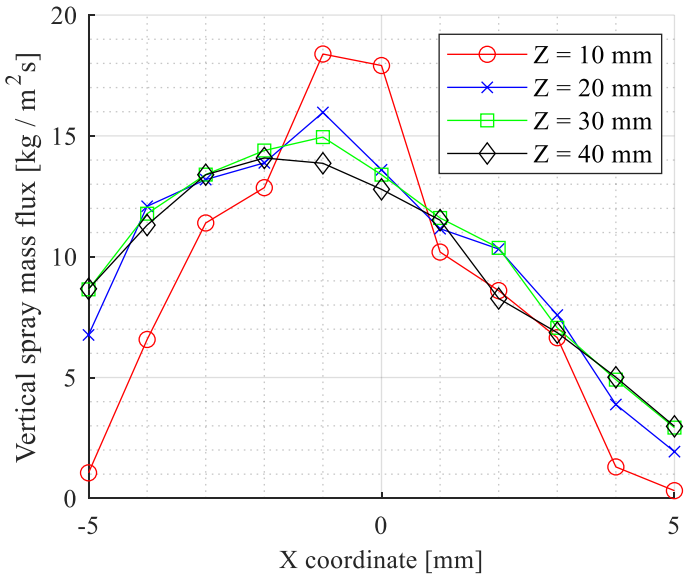

Figure 4.10: Spray mass flux, vertical component, for the XZ scan.

Finally, the mass flux of the spray was calculated analytically by using the Saffman algorithm described in section 3.5.4. With the geometries of the nozzle and of the atomization edge used for this study, the obtained trends shown in Figure 4.10 are reasonable. In fact, the spray tends to spread symmetrically around the central vertical axis near $X = 0$ and for this reason, a maximum appears in the mass flux in the center of the spray. Furthermore, moving away from the prefilmer

(with increasing Z values), the whole amount of spray will be distributed among a wider area in the horizontal direction resulting in lower mass flux values.

For all the properties listed above in the diagrams it is possible to notice a certain symmetry around $X = -1$ mm and not $X = 0$ (where the prefilmer edge is). This could be explained because the water film covers the left side of the atomization edge, as shown in Figure 3.4. Therefore, the amount of air coming from the right part of the atomization edge will be slightly higher than the one coming from the left side because of the water film thickness. The excess of air in the right part is responsible in moving the center of symmetry of the spray slightly on the left.

4.1.2 XY plane – area spread investigation

After having characterized the spray in the XZ plane, the depth in the Y-axis needed to be investigated as well, in order to determine the homogeneity of the spray. Since by the looks of the spray (Figure 4.11) it was not certain whether it was uniform along the Y-axis, the need for this investigation is even more apparent.

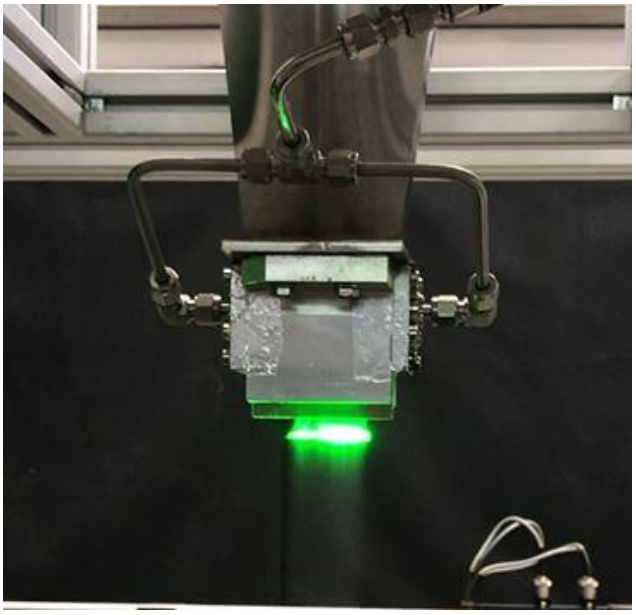

Figure 4.11: Spray along the atomization edge, YZ plane.

After a preliminary scan along the Y-axis and observing until which position a relatively high data rate was still detected by the PDA measurement technique, the boundaries for this

investigation were determined. For the extremes of the X coordinate the choice was based on the previously studied test in section 4.1.1: considering as the centre of symmetry of the spray around the position $X = -1$ mm, a distance of 9 mm from both sides were studied. In Figure 4.12, the measurement positions (in mm) for this test are shown The plane selected for these measurements was at a downstream distance of $Z = 40$ mm, a distance covered also in the aforementioned test.

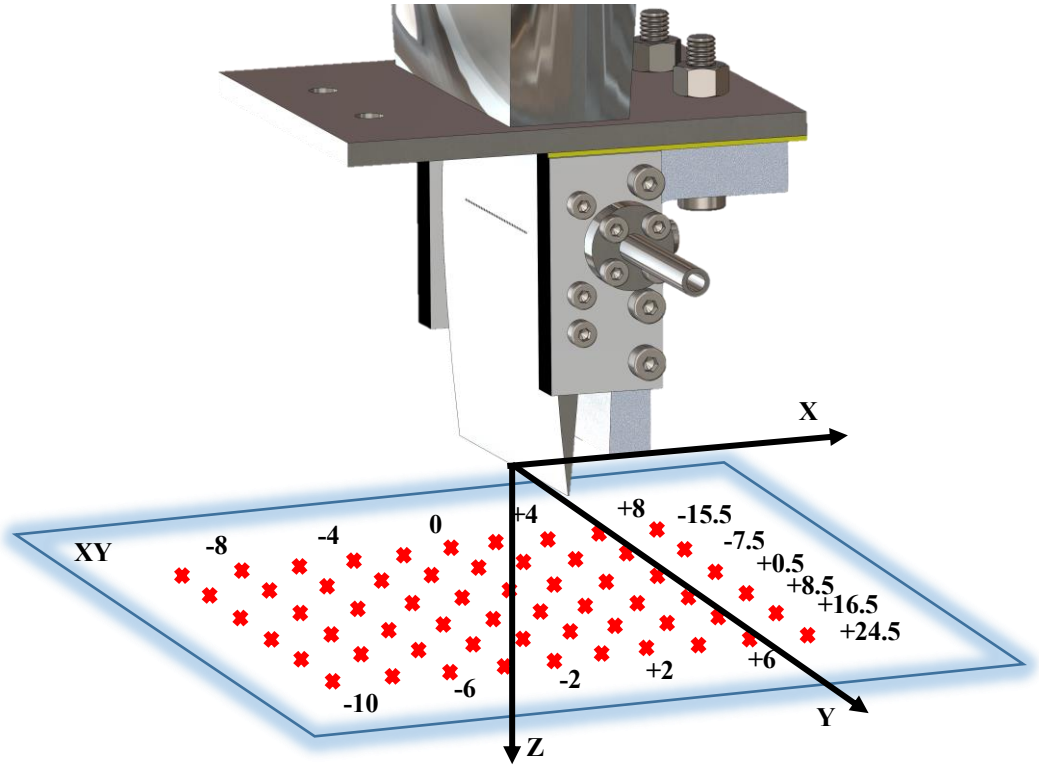

Figure 4.12: Measurement positions for the XY plane scan, at Z = 40 mm.

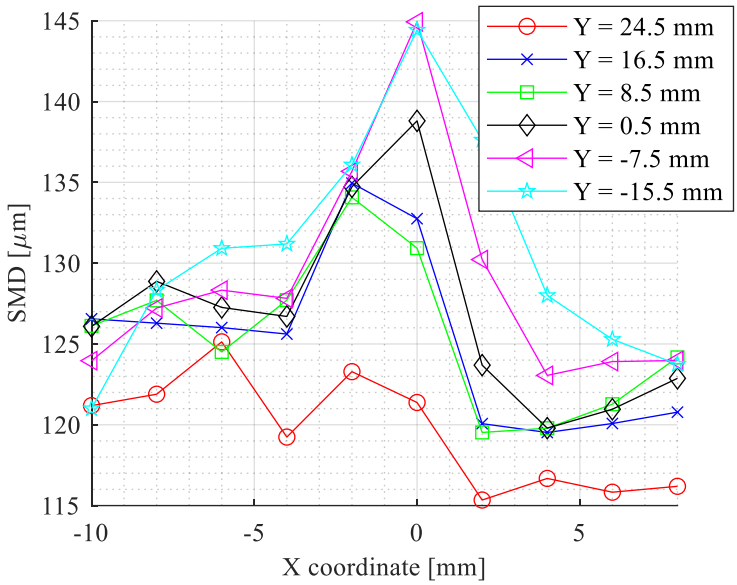

Figure 4.13: SMD, for the XY plane.

The SMD shows a local maximum around $X = -2$ mm and $X = 0$ mm. Mostly, in all different Y positions the SMD is constant along the X-axis. Only the curve at $Y = 24.5$ mm does not follow the trend of the other curves and a reason for this different behaviour could be the low number of droplets since this was a position at the edge of the spray, which contributes to make the data more random. In the interval between $X = -5$ mm and $X = 5$ mm the result is consistent with the test in section 4.1.1.

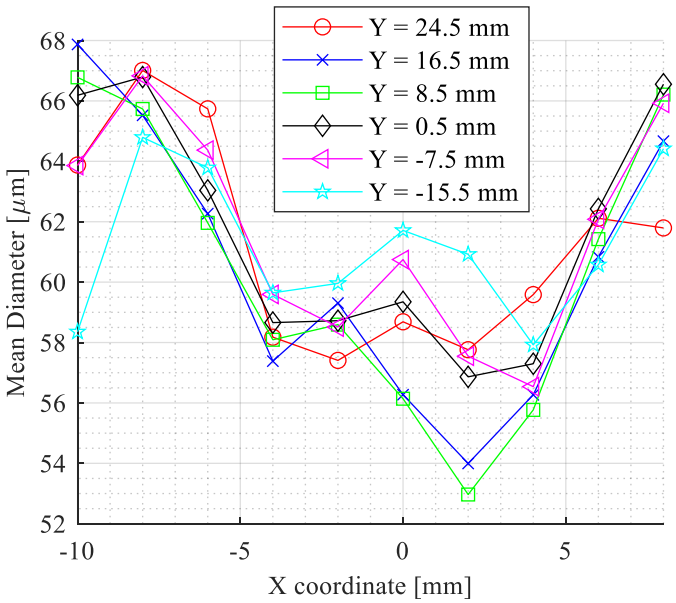

Figure 4.14: Mean Diameter, for the XY plane.

The trend of the mean diameter, shown in Figure 4.14, is consistent with the trend observed in section 4.1.1: at the extremes of the interval, the mean diameter continues increasing while the SMD keeps quite constant.

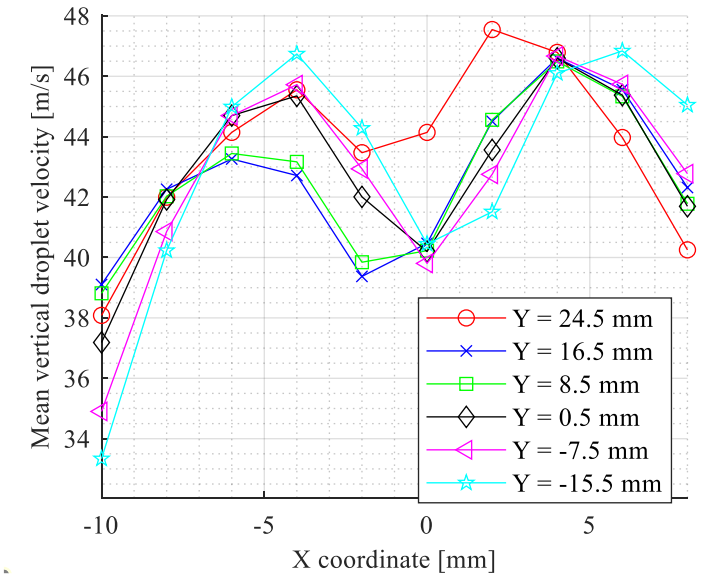

Figure 4.15: Mean vertical droplets velocity, for the XY plane.

Regarding the droplet velocities, Figure 4.15 and Figure 4.16 show the vertical (along Z-axis) and horizontal (along X-axis) components respectively for the different Y positions. As already seen in the previous test, a local peak in the vertical velocity is present near $X = -5$ mm and $X = 5$ mm. This trend is valid for all the different curves represented, so along all Y-axis. The horizontal droplet velocity also has the same trend in the X-axis as was in the previous test.

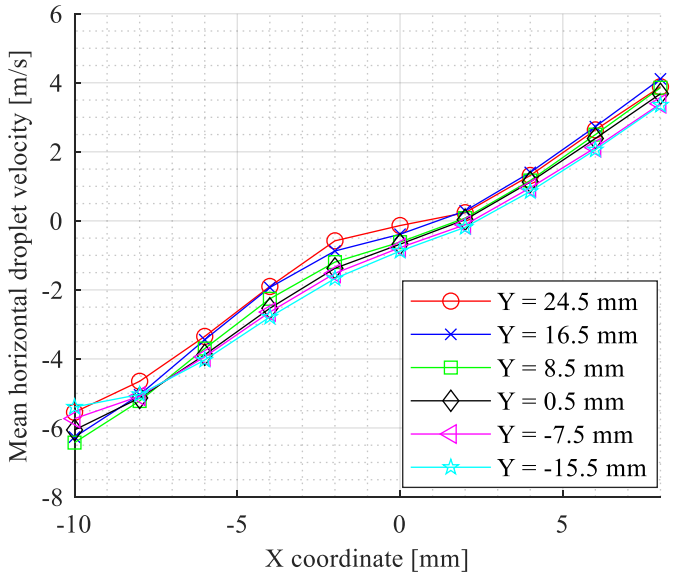

Figure 4.16: Mean horizontal droplets velocity, for the XY plane.

All the curves for the different positions in the Y-axis follow the expected trend: going from the centre of the spray to the extremes of the interval the absolute value of the horizontal component of the velocity increases (Figure 4.16) and the same is also valid for the velocity angle plotted in Figure 4.17. The values are consistent with the ones in section 4.1.1 in the interval between $X = -5$ mm and $X = 5$ mm. Here, going until $X = -10$ mm and $X = 8$ mm it is possible to notice the maximum angle of the spray.

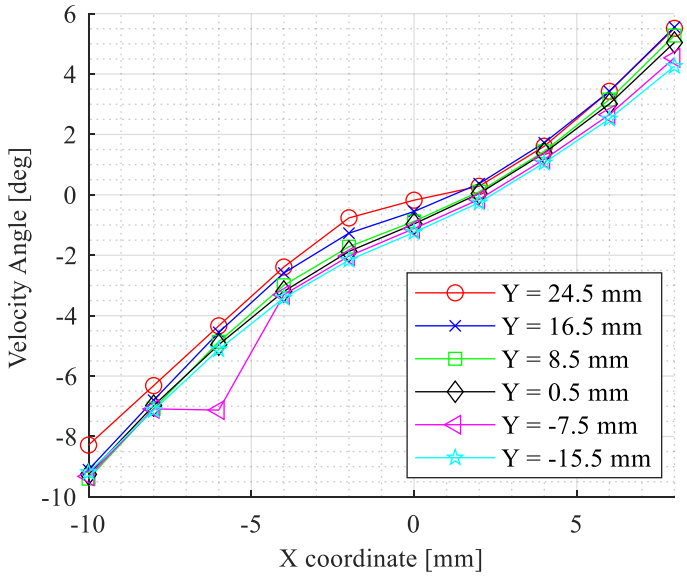

Figure 4.17: Angle between absolute velocity vector and Z direction, for the XY.

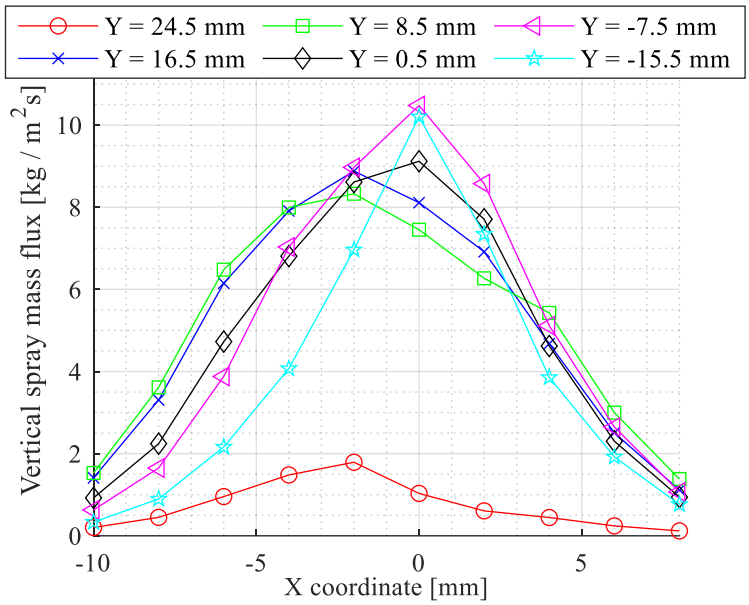

Figure 4.18: Spray mass flux, vertical component, for the XY plane.

The mass flux of the spray in the scanned area can also be calculated. According to the already described peak of the SMD, the mass flux in the vertical (Z-axis) direction shows a maximum placed between $X = 0$ mm and $X = -2$ mm as shown in Figure 4.18. Except for the curve at $Y = 24.5$ mm where the data rate was quite low, all the other curves have a similar trend and almost identical values, which certifies a quite constant behaviour of the spray along the whole atomization edge.

Having established the calculation of the mass flux in the XY plane scanned, it is possible to estimate the total mass flow of water to verify the mass flux calculations. In Figure 4.19 the dominant component of the mass flux is illustrated in the 3D space, in order to fit a surface to the set of points.

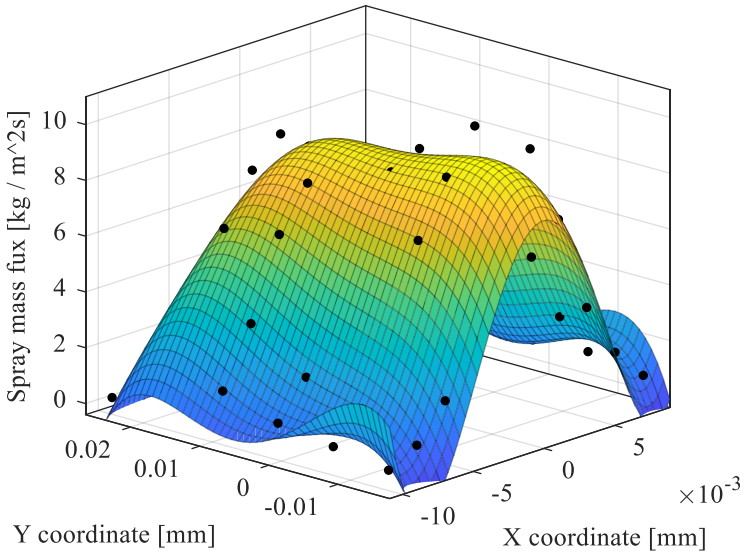

Figure 4.19: Vertical spray mass flux, XY plane.

Through the surface it is easier to visualize the quite constant behaviour of the spray along the Y-axis. By calculating the volume under the surface in the XY plane, by double integration along the two axes, the result would be the estimation of the water mass flow rate. The resulting estimated mass flow from the integration is $\dot{m}_{w,est} = 11.71$ kg/h. Comparing it with the actual value of 12 kg/h read by the mass flow meter of the test rig, the mass flux calculation is acceptable, since the error is lower than 3 %. Therefore, the application of the Saffman algorithm for calculating the spray mass flux is verified for the rest of the experiments in this work. Finally, since the spray is acceptably homogeneous along the Y-axis, the choice of measurements in a single Y position for the rest of the experiments is reasonable.

4.1.3 Influence of pressure drop

With determined the characteristics of the spray in all possible planes, the next target was to define how the droplet characteristics are influenced by a different pressure drop across the nozzle. The measurements were performed exactly below the atomization edge, for $X = 0$ mm and $Y = 0$ mm. Eleven different vertical positions were studied with a space interval between each other of 3 mm. The interval from $Z = 10$ mm to $Z = 40$ mm is covered. Figure 4.20 shows where the measurements positions (in mm) are placed with regard to the nozzle.

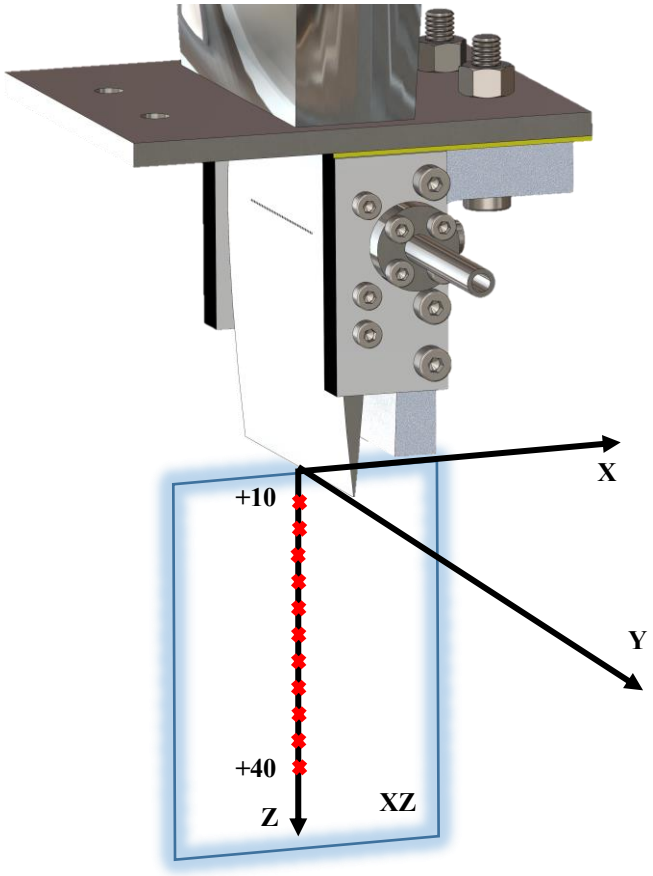

Figure 4.20: Measurement positions for the pressure drop variation.

The results are reported in the following diagrams. For the different studied properties, the comparison between the four different pressure drops across the nozzle is discussed.

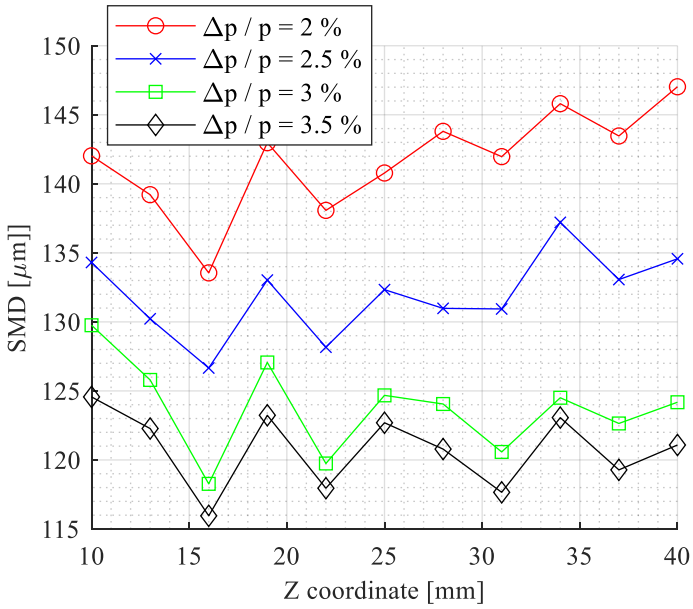

Figure 4.21: SMD, comparison of the vertical scan among different Δp/p values.

Starting with the SMD on Figure 4.21, the trend of each curve remains the same for each chosen pressure drop. For increasing pressure drop, the SMD is decreasing as expected [17].

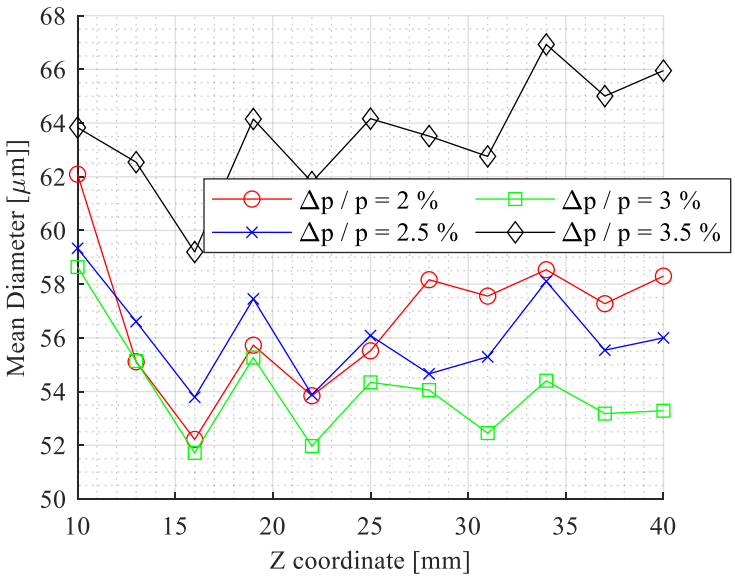

Figure 4.22: Mean Diameter, comparison of the vertical scan among different Δp/p values.

The mean diameter on the other hand (Figure 4.22) shows a different trend at 3.5 % pressure drop, where the mean diameter suddenly increases while the SMD for the same pressure drop was

continuing to decrease with respect to the lower pressure drops (Figure 4.21). To understand this sudden change in the trend, the distributions of the droplet diameters for the case at pressure drops 2 % and 3.5 %, at the vertical position $Z = 40$ mm are presented in Figure 4.23.

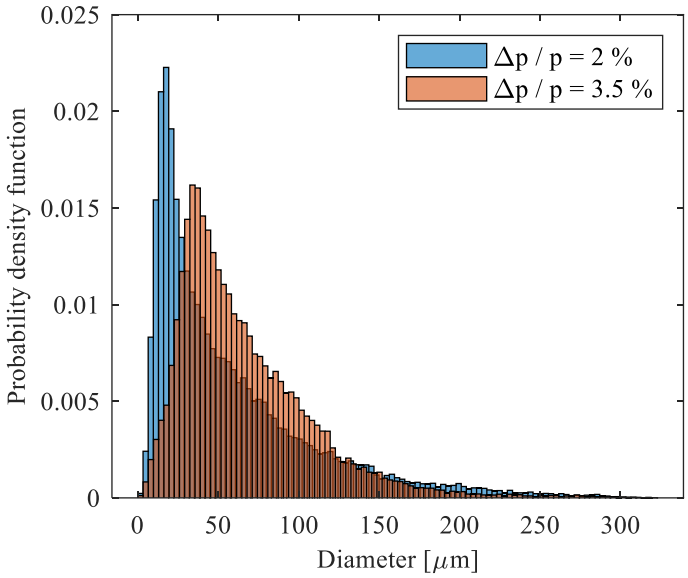

Figure 4.23: Droplet diameter distribution for different pressure drops, at Z = 40 mm.

The mean diameter seems clearly higher at 3.5 % pressure drop since the peak of the distribution is lower and moves to the right, while the SMD is higher at pressure drop 2 % since the columns of the histogram in the region of bigger diameters, where SMD is strongly influenced, present higher values for this pressure drop.

The mean droplet velocity in the vertical direction is presented in Figure 4.24. Since this investigation was conducted at $X = 0$ mm, the horizontal component was close to zero so it shows no interest.

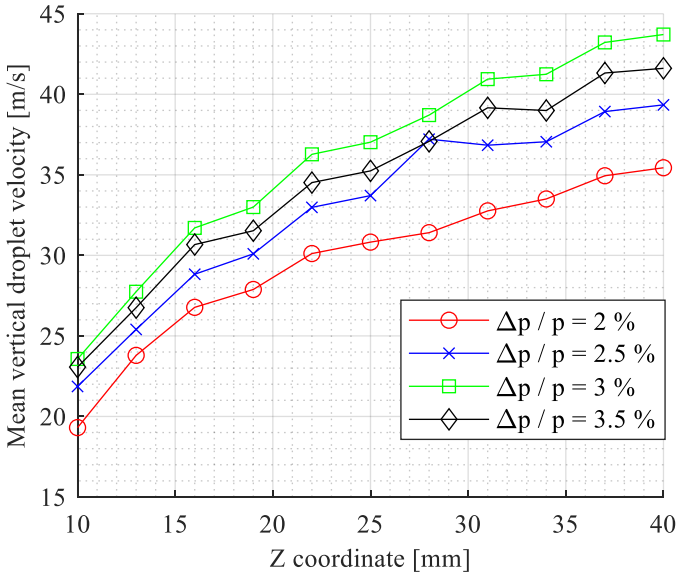

Figure 4.24: Mean vertical droplets velocity, comparison of the vertical scan among different Δp/p values.

As it was already noticed in the steady flow test in section 4.1.1 (Figure 4.6), the vertical droplet velocity increases linearly with increasing the distance from the atomization edge. Furthermore, the velocity also increases for increasing pressure drop values, until $\Delta p/p = 3\ \%$. For $\Delta p/p = 3.5\ \%$, the mean velocity is unexpectedly reduced. For future research, it would make sense to perform other tests in the same conditions until $\Delta p/p = 5\ \%$. Literature confirms that for increasing air velocities (so for increasing pressure drop across the nozzle), the mean vertical droplet velocity should also increase [2].

To explain this unexpected behaviour, one can take into account only the small droplets, since they are more likely to follow the trend of increasing air velocity with increasing pressure drop due to their low inertia and low Stokes number [43]. Considering only the small droplets (diameter lower than 15 µm) the results are showed in Figure 4.25.

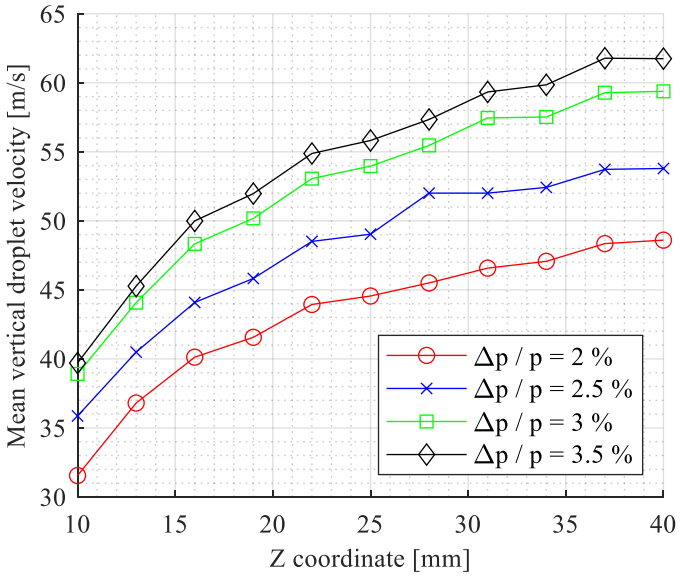

Figure 4.25: Mean vertical droplets velocity, small droplets (diameter lower than 15 µm).

As expected, the mean vertical droplet velocity is higher for increasing pressure drop even after 3 % considering the velocities of only small droplets. This outcome suggests that probably there was no mistake in this particular experiment, but the behaviour of the spray changes.

Finally, the spray mass flux in the vertical direction is shown in the Figure 4.26.

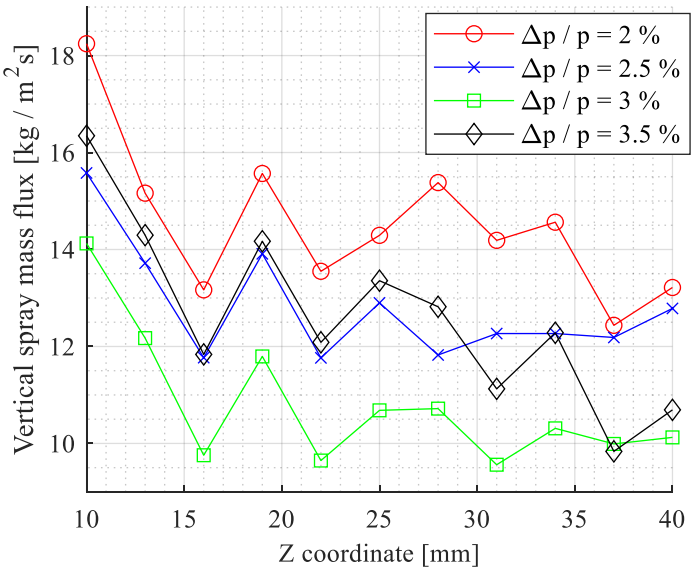

Figure 4.26: Spray mass flux, vertical component, comparison of the vertical scan among different Δp/p values.

Most importantly, the mass flux in all cases has a decreasing trend while going away from the atomization edge, so for increasing Z-values, as it was observed also in the first steady test (Figure 4.10). The mass flux at the highest pressure drop is not lower than the mass flux of the lower pressure drops, which enhances the interest for further investigation in the subject.

4.1.4 Influence of air preheating temperature

In this test the influence of an increasing airflow temperature was investigated. A preheating unit is installed at the test rig before the bypass plenum, as shown in Figure 3.1. The temperature is set by a PID controller and a thermocouple at the exit of the preheater. In order to read a precise value of the airflow temperature close to the atomization edge, a thermocouple is installed just before the nozzle. As a consequence, a higher temperature should be reached at the preheating unit in order to reach the desired value at the atomization edge after all thermal losses. In Figure 4.27 the measurement positions (in mm) are illustrated. A vertical scan is considered for this test, keeping both X and Y coordinates equal to zero.

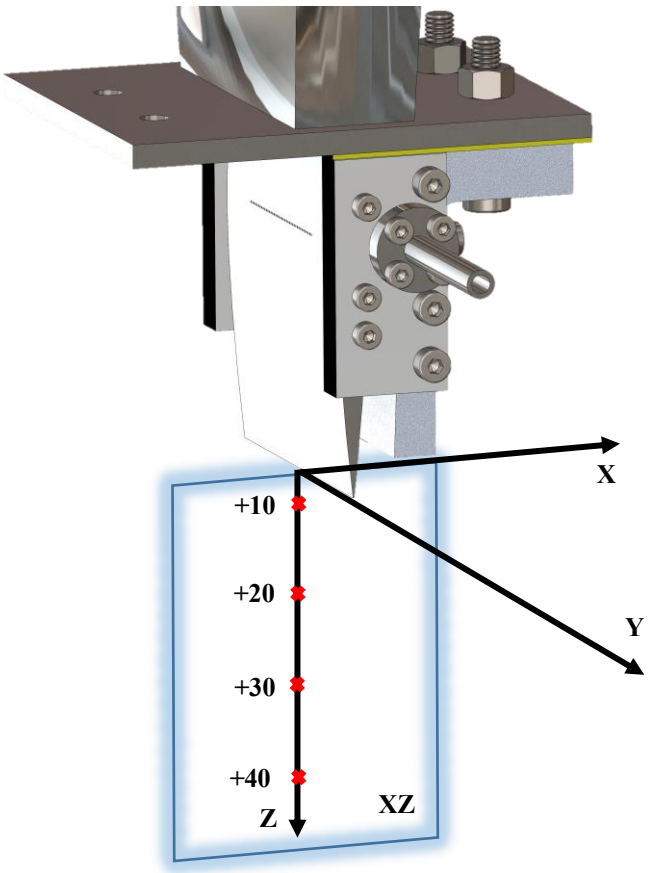

Figure 4.27: Measurement positions for the preheating temperature variation.

The preheating temperatures selected for this investigation were 100 °C, 150 °C and 200 °C before the nozzle. As a reference, a measurement on the same positions with atmospheric temperature is also considered.

Two different tests were performed in order to isolate one single operating parameter each time and observe its influence in the spray characteristics. In the first test, the isentropic air velocity as a function of the pressure difference and the density was kept constant. In the second one, the pressure drop across the nozzle and the Weber number were kept constant. For both tests, a constant ALR is maintained by adjusting the water mass flow rate accordingly. The values of the main parameters for the two tests regarding the influence of the preheating temperature are shown in Table 3 and Table 4. The Weber number was calculated through equation (2.3), considering as characteristic length the atomization edge length. The isentropic air velocity was calculated through the equation

$$U = \sqrt{\frac{2 \cdot \Delta p}{\rho_{air}}} \tag{4.1}$$

Table 3: Influence of a pre-heating temperature, constant air velocity and *ALR*.

T [°C]	T [K]	Δp [mbar]	ρ_{air} [kg /m^3]	$\frac{\Delta p}{p}$ [%]	u_{air} [m/s]	*We* [-]	m_{air} [kg/h]	m_{water} [kg/h]	*ALR* [-]
20	293.15	32	1.24	3.0	71.8	6154	329	12	27
100	373.15	25	0.97	2.4	71.8	4808	257	9.4	27
150	423.15	21,9	0.85	2.1	71.7	4212	225	8.2	27
200	473.15	19,4	0.76	1.9	71.4	3731	200	7.3	27

For the following figures, the droplet characteristics are shown as a function of the air density.

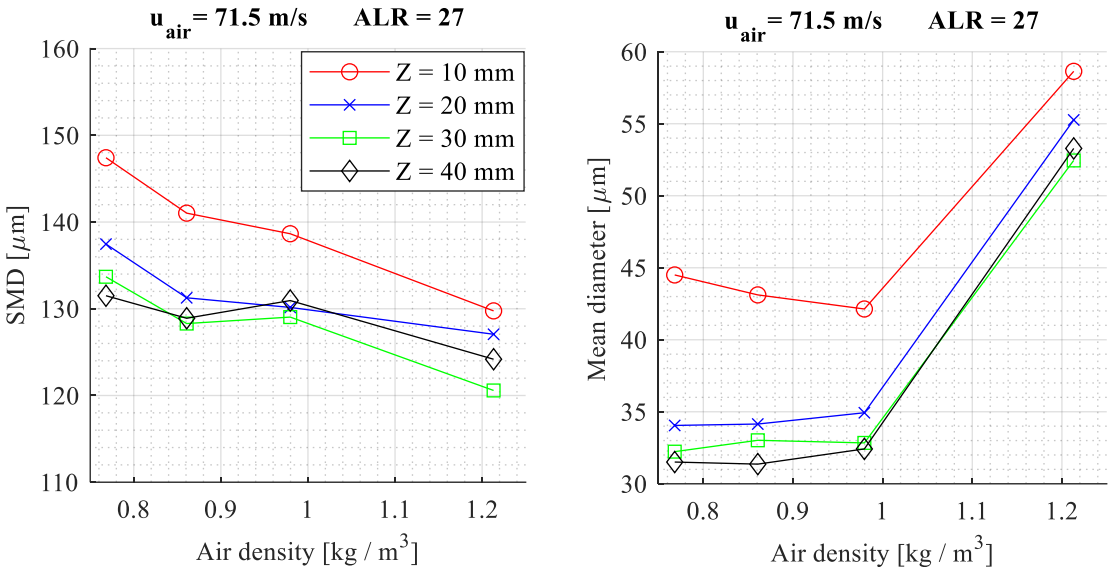

Figure 4.28: SMD and Mean Diameter, influence of a pre-heating temperature.

In Figure 4.28, the SMD and the mean diameter are shown. Increasing the temperature from the ambient to 100 °C, a strong reduction in the mean diameter is observed. On the other hand, a slight increase in the SMD is also noticed for increasing temperatures. The droplet distribution (at $Z = 10$ mm) and the ratio between small and all droplets (diameter lower than 10 mm) give an insight about this contradiction (Figure 4.29).

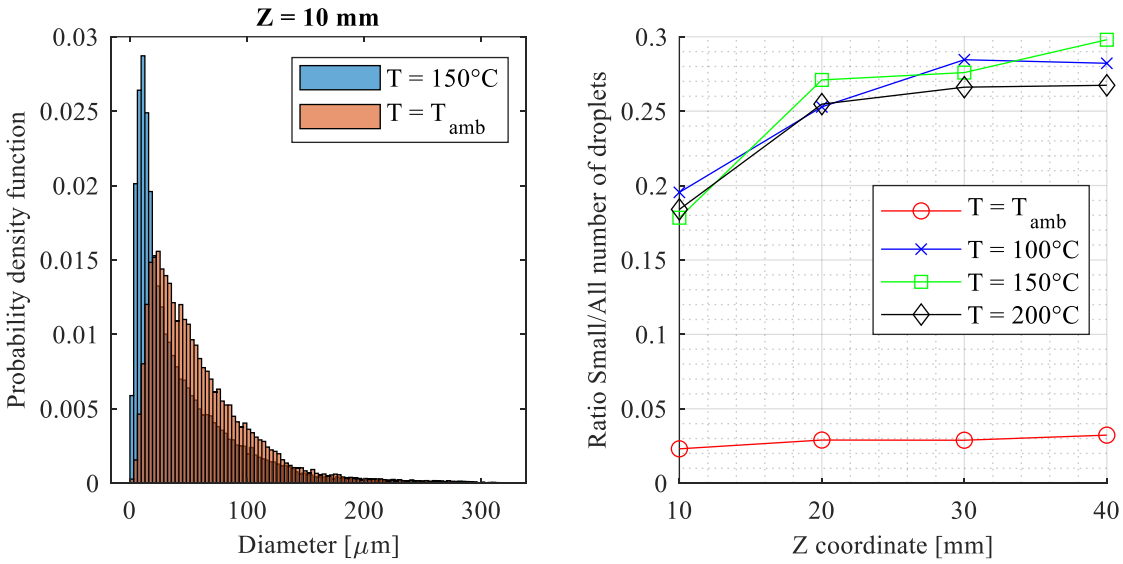

Figure 4.29: Distribution and small/all number of droplets ratio.

It is clear how the ratio of small droplets in the spray increases passing from the ambient temperature to $T = 100\ °C$ and this increase justifies the big drop in the mean diameter. From $T = 100\ °C$ to $T = 200\ °C$ the curves tend to be quite similar in values and for this reason also the mean diameter keeps quite constant in that range of temperatures. Observing the end of the distribution (Figure 4.30), it is possible to notice an overlapping of the two histograms for high diameters with a slight dominance of the columns of $T = 150\ °C$, which explains the larger SMD in this case.

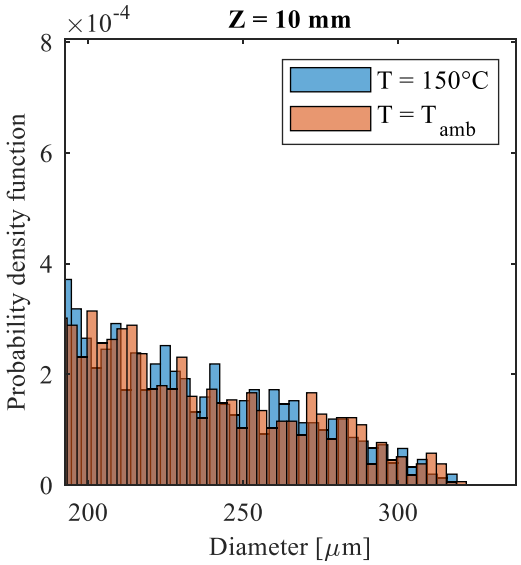

Figure 4.30: Distribution, zoom in the high diameters range.

The big drop in the mean diameter passing from $T = T_{amb}$ to $T = 100\ °C$ could be explained by the contribution of the evaporation that can be responsible for reducing the particle diameters, while further increase in the preheating temperature does not have such a strong influence. This phenomenon could be an interesting topic for future research.

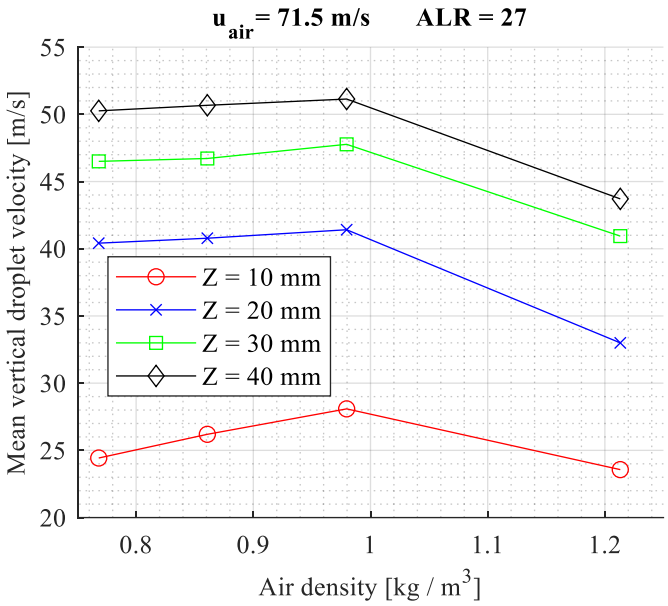

Figure 4.31: Mean vertical droplet velocity.

Figure 4.31 shows the mean vertical droplet velocity for the different air densities and downstream positions. As expected, the droplet velocity follows the trend of the imposed air velocity, that for this test was kept constant. The increase between the environmental temperature and $T = 100\ °C$ is consistent with the reduction in mean diameter in that interval. The absolute value increases again going from the curve at $Z = 10\ mm$ to the curve at $Z = 40\ mm$, as already established in all the previous steady cases due to the acceleration of the droplets in a larger distance.

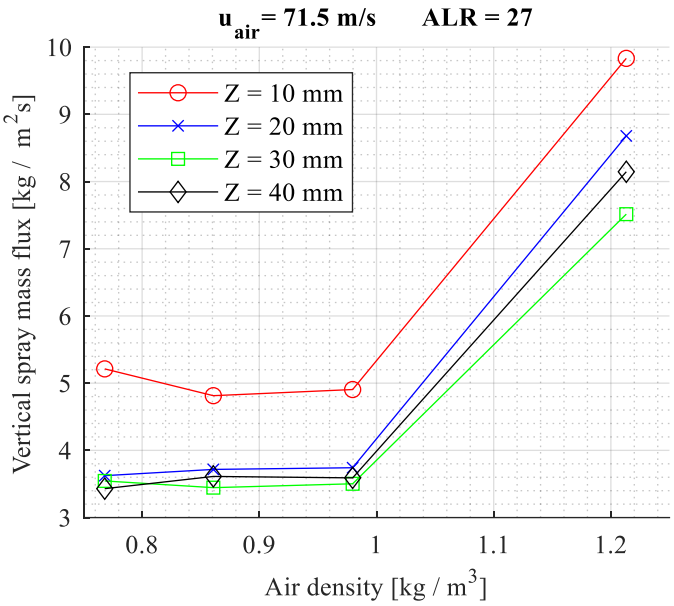

Figure 4.32: Vertical spray mass flux.

The mass flux of the spray (Figure 4.32) keeps constant from T = 100 °C to T = 200 °C and tends to decrease going further away from the atomization edge because of the spreading along the X coordinate of the spray, as already seen in the previous steady chapters. The drop in the mass flux between the ambient temperature test and the others makes sense if an amount of the volume of the spray has been evaporated due to the preheating temperature.

Finally, the influence of the preheating temperature was investigated in tests where, apart from the ALR, the pressure drop (and therefore the Weber number) was kept constant instead of the isentropic air velocity.

Table 4: Influence of a pre-heating temperature, constant Weber number and *ALR*.

T [°C]	T [K]	Δp [mbar]	ρ_{air} [kg /m^3]	$\frac{\Delta p}{p}$ [%]	u_{air} [m/s]	*We* [-]	m_{air} [kg/h]	m_{water} [kg/h]	*ALR* [-]
20	293.15	32	1.24	3.0	71.8	6154	329	12	27
100	373.15	32	0.98	3.0	81.0	6154	292	10.7	27
150	423.15	32	0.86	3.0	86.3	6154	274	10	27
200	473.15	32	0.77	3.0	91.2	6154	259	9.5	27

In the following Figure 4.33 there are represented the SMD and the mean diameter. While the mean diameter shows a trend similar to the trend of the mean diameter with constant air velocity (Figure 4.28), the SMD remains almost constant in this case (constant Weber number). For

constant air velocity the SMD increases by decreasing the density (decreasing the We-number, Figure 4.28).

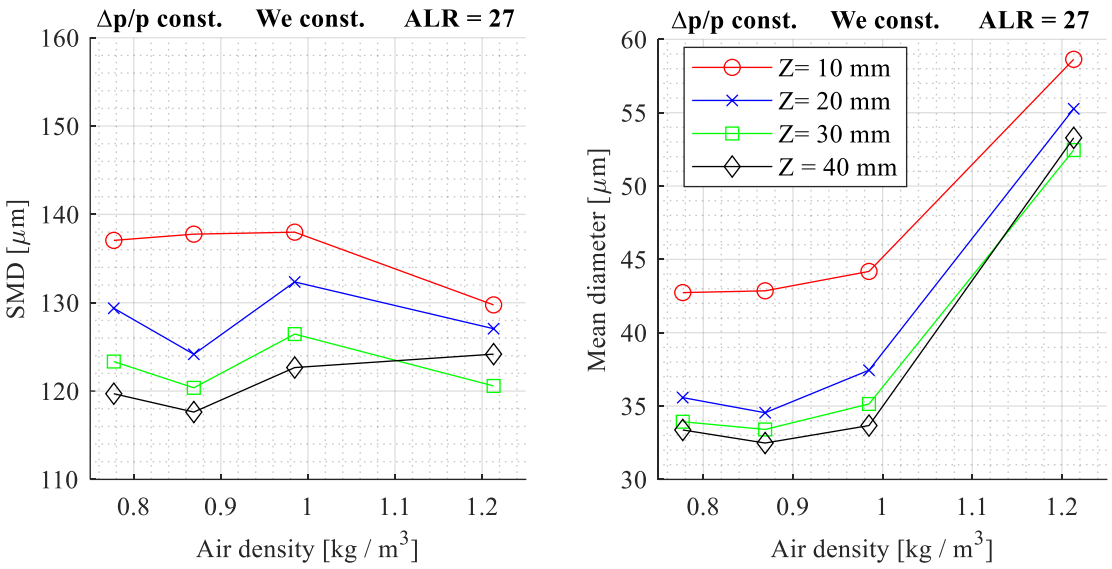

Figure 4.33: SMD and Mean Diameter, influence of a pre-heating temperature.

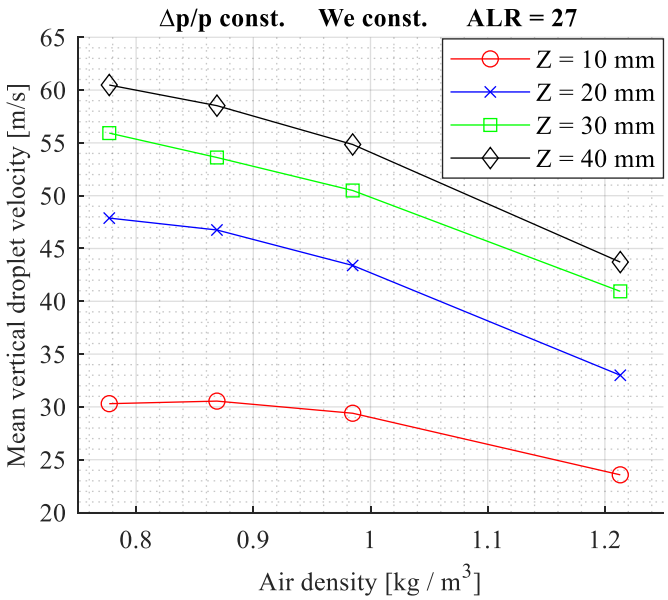

Figure 4.34: Mean vertical droplet velocity.

The mean droplet velocity, shown in Figure 4.34, is now increasing with decreasing air density or increasing the preheating temperature, since the isentropic air velocity is also increasing (Table 4).

Concluding with the mass flux shown in Figure 4.35, the trend is similar to the previous test in Figure 4.32. The largest decrease appears between the atmospheric temperature and the first preheating temperature, probably due to the evaporation of the droplets, and then remains almost constant. Naturally, moving away from the atomization edge the mass flux is decreasing due to the spray spreading in a larger area.

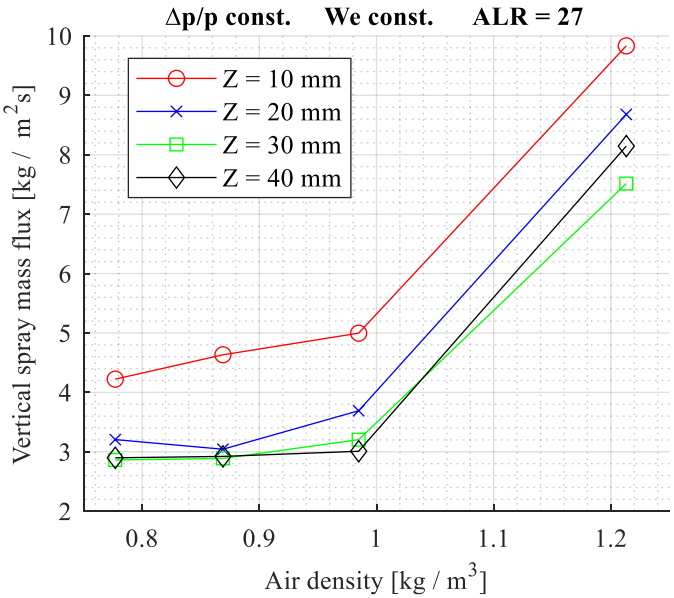

Figure 4.35: Vertical spray mass flux.

4.2 Unsteady airflow tests

As already mentioned, the objective of this project is to investigate the influence of an oscillating airflow in the properties of the spray. To achieve this a siren was installed in the test rig (as described in 3.3) in order to force a fluctuation on the air velocity at a certain frequency and amplitude. The split ratio between the air mass flow that passes through the siren and the mass flow through the plenum controls the amplitude of the oscillation. Figure 4.36 shows the resulting excitation frequencies and their corresponding amplitudes at a certain split ratio from preliminary CTA hot wire measurements analysed with Fast Fourier Transform (FFT), performed to characterize the siren used for this project (see equation (3.1) for the correlation between the excitation frequency and the siren speed).

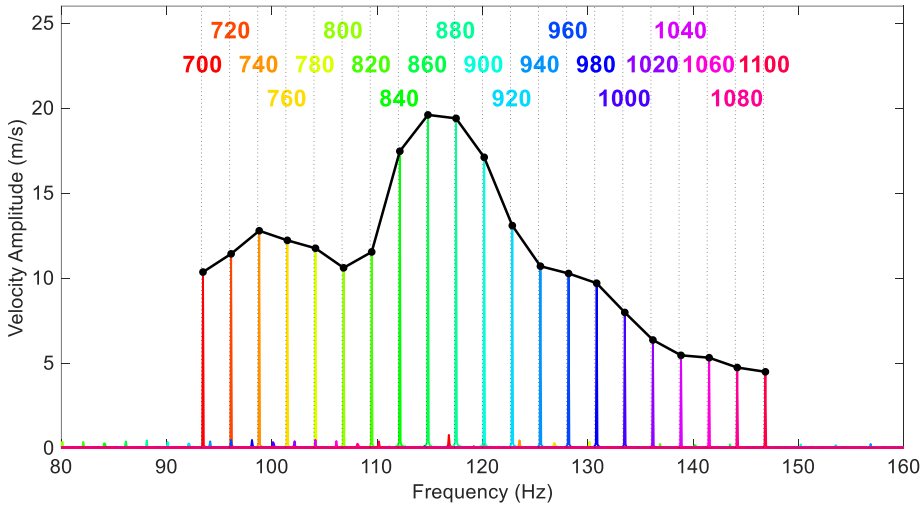

Figure 4.36: FFT of the air velocity measured at 40 mm downstream the atomization edge.

To investigate three frequencies with the maximum difference from each other, the selected ones were 93.5 Hz (700 RPM), 120.2 Hz (900 RPM) and 146.9 Hz (1100 RPM).

As concerns the measurement plan, just one side of the spray in the XZ – plane was studied, since the previously mentioned steady tests showed that the behaviour and the characteristics of the spray are symmetric with respect to the central axis (maximum 1 mm on the left of the atomization edge). The selected measurement positions in the X-axis were from $X = -10$ mm to $X = -0$ mm. In the Y-axis, the measurements were performed at $Y = 0$ mm since from the steady test 4.1.2 it was possible to see that in the various Y positions the mass flux was almost constant, while also to keep a consistency and have a comparison with steady test 4.1.1. The vertical Z position is kept constant at 40 mm downstream the atomization edge. Figure 4.37 illustrates where the six measured points are spatially placed under the airblast atomizer (in mm).

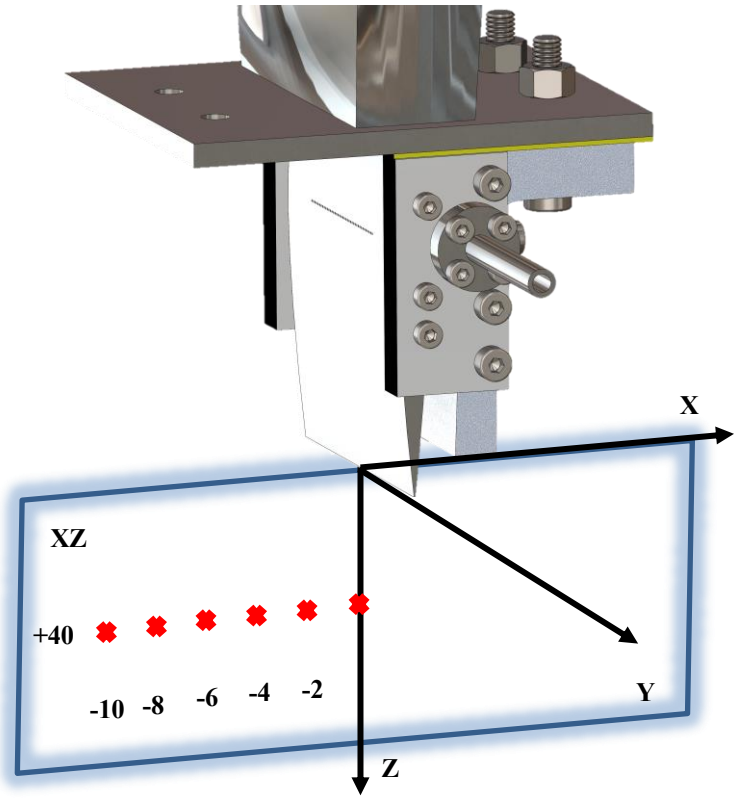

Figure 4.37: Measurement positions, unsteady test.

The operating conditions are again chosen in a way that allows for a comparison with the steady case: the average pressure drop across the nozzle is kept constant around 3 %, the air mass flow oscillates around an average value of 245.9 kg/h and the water mass flow rate is fixed to 12 kg/h. The resulting global ALR oscillates around a mean value of 20.5.

4.2.1 Excitation Frequency 120.2 Hz

In this chapter, only the results for the intermediate frequency 120.2 Hz are shown and discussed, since similar trends and comments can be made for all the three cases. The results for the other studied frequencies are present in Appendix: 93.5 Hz results and Appendix: 146.9 Hz results. In order to compare each spatial position with each other, the mean vertical velocity curves were used as reference to find in which temporal position the peak value is placed. Therefore, all the properties were shifted so that the mean velocity in the different positions match in phase.

Starting from the SMD, as in the steady test 4.1.1, the value slightly increases from the extreme of the interval towards the centre. Along the period of the fluctuation, it shows a peak at a phase angle between 180° and 200°, for each different spatial point while the amplitude remains almost constant.

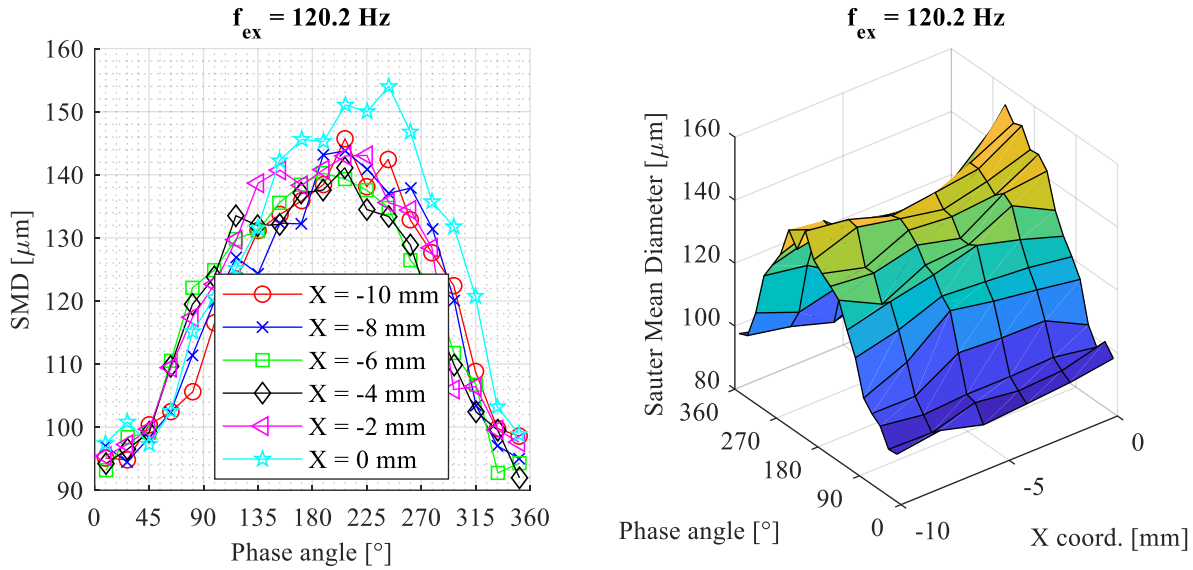

(a) (b)

Figure 4.38: Sauter Mean Diameter, 120.2 Hz.

Figure 4.39 shows the mean vertical droplet velocity. A consistency with the corresponding steady test is noticed: around $X = -5$ mm the velocity reaches a local maximum value. The amplitude of the oscillation remains almost constant in each different spatial position, showing a similar behaviour to the SMD. As expected, when the SMD is low the droplets move faster and vice versa.

The mean horizontal droplet velocity (parallel to the X-axis) is shown in Figure 4.40. It confirms the trend to increase in absolute value moving from the centre of the X-axis to the extreme, far away from the atomization edge. Along the period, a shift compared to the vertical velocity component is noticed because the horizontal velocity is shown in the negatives of the X-axis. When the vertical velocity of the droplets decreases, the horizontal component also decreases in absolute value.

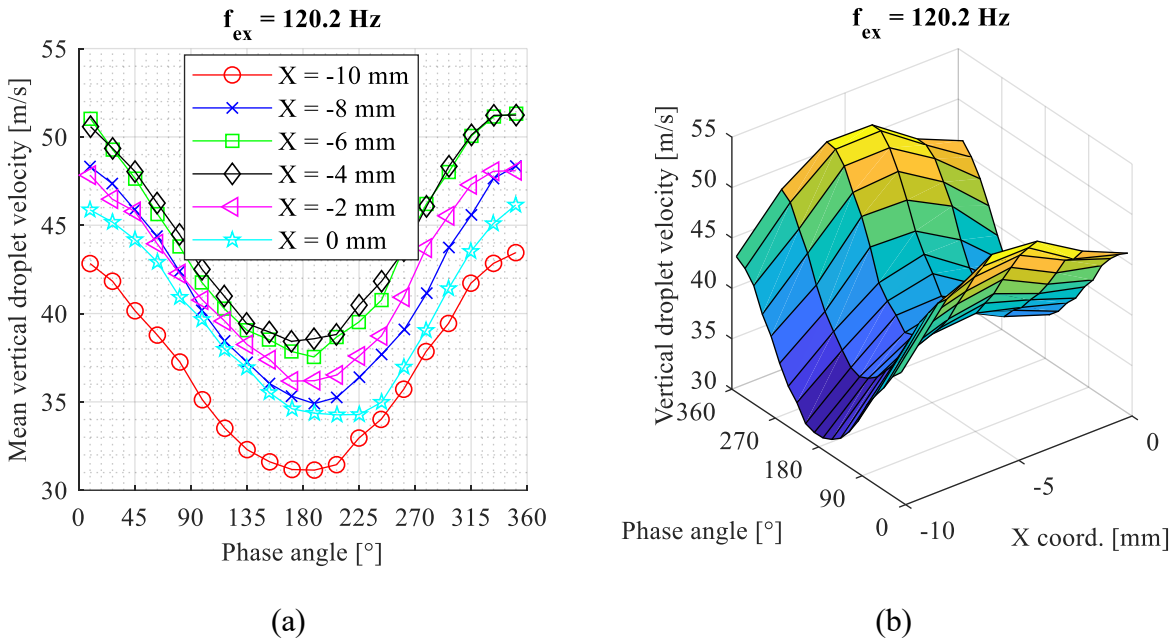

(a) (b)

Figure 4.39: Mean vertical droplet velocity, 120.2 Hz.

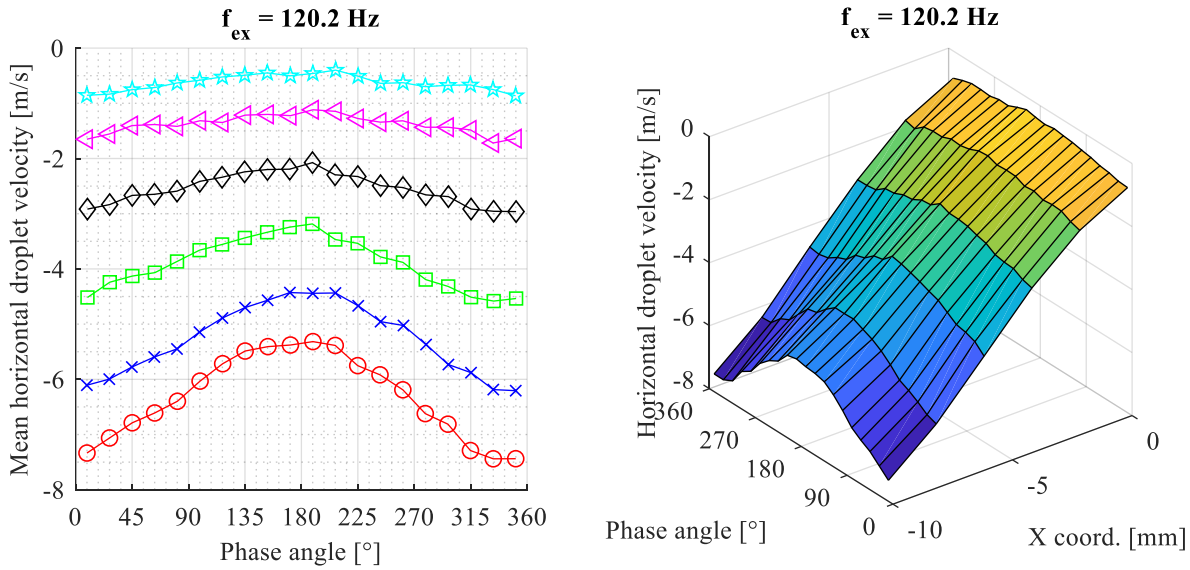

(a) (b)

Figure 4.40: Mean horizontal droplet velocity, 120.2 Hz.

As a result, the outcoming velocity angle (Figure 4.41) tends to remain quite constant along the period in each different spatial position. The velocity angle is obviously increasing (as an absolute value) from the centre of the X-axis to the extreme, matching the angle in the steady tests described in Figure 4.9. The phase independent behaviour means that at a random spatial point,

the external observer would see each droplet passing through that point with the same angle, even though the two velocity components of the droplet are oscillating in time.

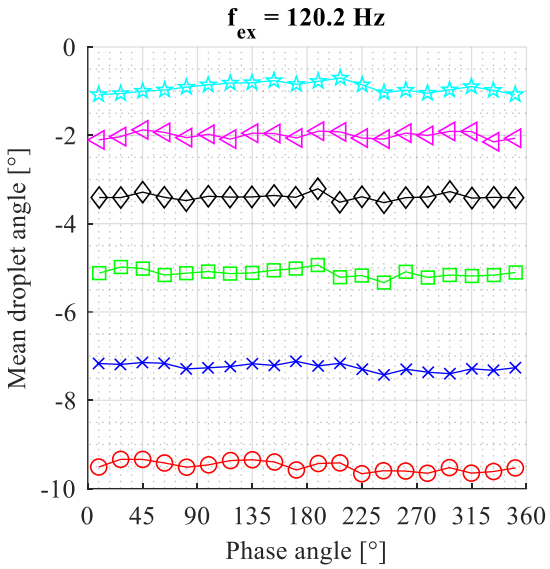

Figure 4.41: Mean droplet velocity angle, 120.2 Hz.

The mass flux of the spray in the vertical direction is shown in Figure 4.42, where an increasing trend moving towards the centre of the spray is noticed as expected from the steady test in section 4.1.1. The spray mass flux strongly oscillates near the centre axis, while towards the extreme of the interval the amplitude of the fluctuation becomes negligible. As expected, the average value of the vertical mass flux is maximum near X = 0 mm and decreases moving along the X-axis.

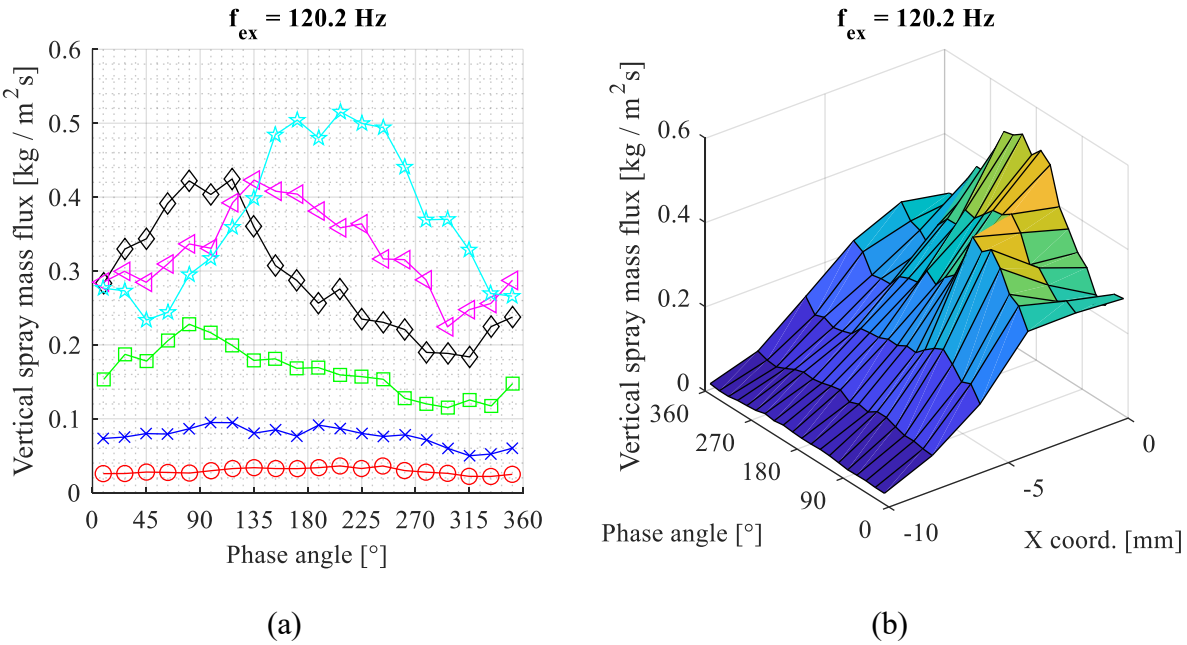

(a) (b)

Figure 4.42: Vertical spray mass flux, 120.2 Hz.

Finally, the droplet number crossing the measurement volume is shown in Figure 4.43. A strong influence of the air fluctuation is observed in the droplet number as well, which matches the phase of the mean droplet velocity. This is normal, since the faster the droplets move, the more droplets are crossing the measurement volume in a certain time interval.

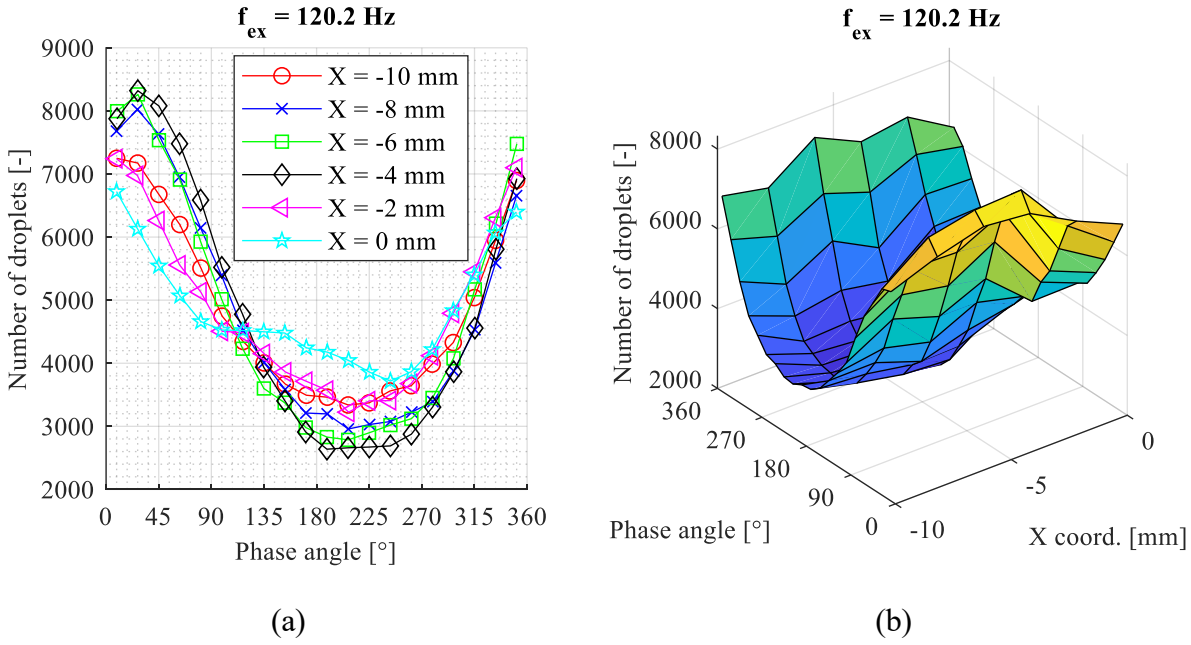

(a) (b)

Figure 4.43: Number of droplets, 120.2 Hz.

4.2.2 Comparison of the three frequencies

Since the main target of this project is to understand the behaviour of the spray characteristics when acoustic instabilities occur and to produce experimental data that could help the development of trustable numerical simulations, in this chapter comparisons between different air excitation frequencies are discussed.

- *Small droplets distribution inside the spray*

An interesting observation would be the percentage of small droplets in the spray for each different experiment. The ratio between the number of small droplets (all the droplets with diameter smaller than 25 µm) and the total number of droplets is illustrated in Figure 4.44, where the axes on the base are the time period (phase angle) and the X coordinate. This ratio is displayed for the three frequencies investigated in this work.

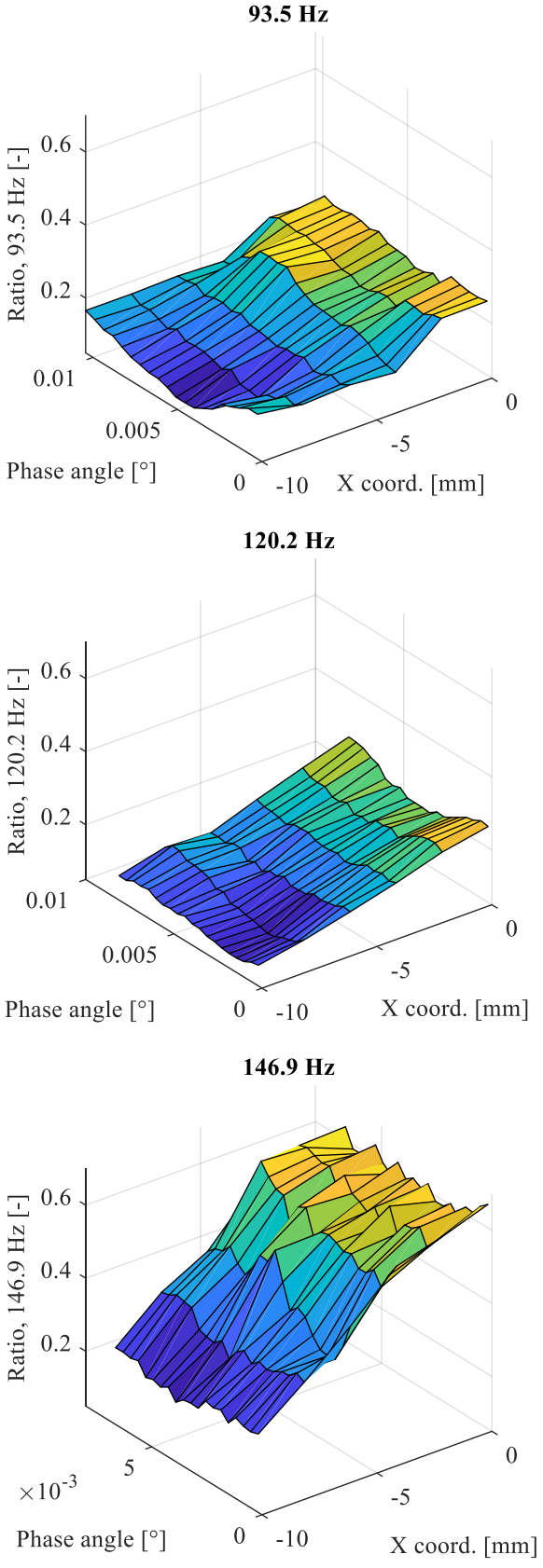

Figure 4.44: Ratio Small/All droplets for different frequencies.

For all the three frequencies, a trend along the spatial coordinate is present. From the extreme of the interval towards the centre of the spray the ratio increases, which means that the higher amount of small droplets is placed under the atomization edge while at the borders of the spray there are more particles with diameter higher than 25 µm. This trend is consistent with the one already discussed for the steady case in chapter 4.1.1. Along the phase angle, there is no significant oscillation in the ratio of small droplets in the spray for any of the three investigated excitation frequencies.

Another interesting observation is that while at 93.5 Hz and 120.2 Hz the ratio keeps in a range between 0.1 and 0.3, for the highest investigated frequency 146.9 Hz it spreads in an interval between 0.2 and 0.7. This trend for the different frequencies is also justified by considering the mean diameters in each case. The following diagram shows three curves which represent the mean diameter for each spatial position, each one corresponding to a specific frequency.

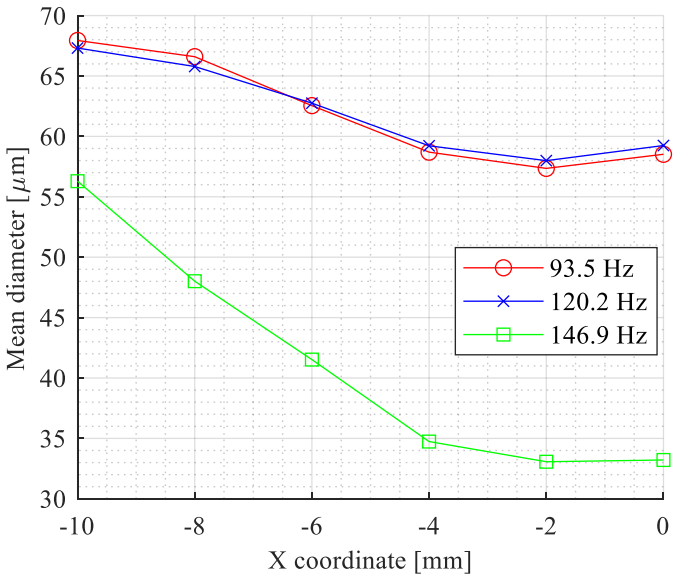

Figure 4.45: Mean diameter averaged in time.

It is clear that, according to the higher percentage of small droplets for the 146.9 Hz, the mean diameters for this frequency come out to be lower with respect to diameters of 93.5 Hz and 120.2 Hz frequencies. Obviously, the trend along the spatial coordinate is confirmed: moving from the extreme towards the centre of the spray, an increase in the ratio of small droplets in the spray is observed and therefore a reduction in the mean diameter happens.

- *Spreading of the Mean vertical droplet velocity*

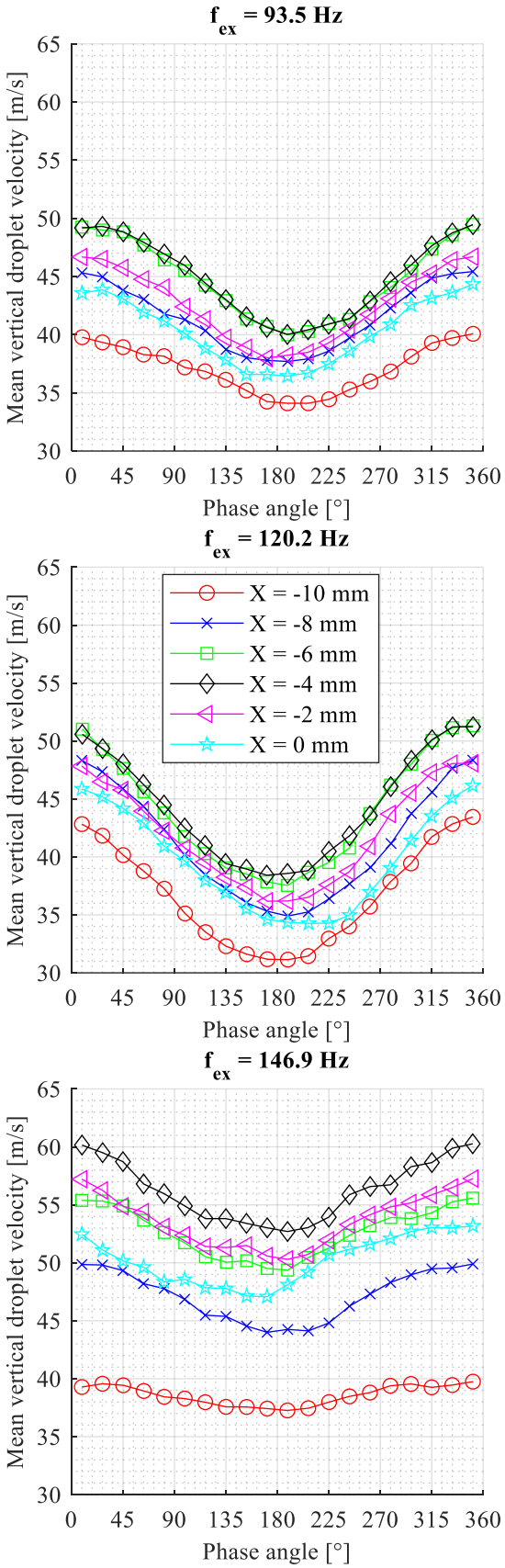

Figure 4.46: Spreading of the Mean vertical droplet velocity.

The mean vertical droplet velocity for the three excitation frequencies is illustrated in Figure 4.46. The amplitude of the oscillation of each single curve, at any given spatial position, is different from one frequency to the other. The lower amplitude appears at 146.9 Hz, the intermediate one is at 93.5 Hz and the bigger one at 120.2 Hz. An explanation for this behaviour can be found in Figure 4.36: the mean droplet velocity amplitude varies according to the variation of the air velocity amplitude, which in fact is minimum at 146.9 Hz, intermediate at 93.5 Hz and maximum at 120.2 Hz. Therefore, the forced airflow influences not only the frequency but also the amplitude at which the droplet characteristics oscillate.

Another interesting outcome from Figure 4.46 is that for a fixed time instant (or phase angle) the difference between the maximum (at $X = -4$ mm) and the minimum velocity (at $X = -10$ mm) increases in the following way: for example, considering the initial time instant, the resulting velocity difference between the aforementioned two positions is 7 m/s at 120.2 Hz, 10 m/s at 93.5 Hz and 20 m/s at 146.9 Hz. To justify this spreading trend of the velocities it is possible to refer to Figure 4.44: the higher the difference between the ratios from the extreme to the centre of the spray, the higher the difference between the number of small droplets that are present in those two spatially different points. Since theoretically small droplets can reach higher velocities compared to bigger droplets, if they are concentrated much more in a single position, the velocity in that point will tend to be higher. Figure 4.47 confirms the behaviour of the velocities.

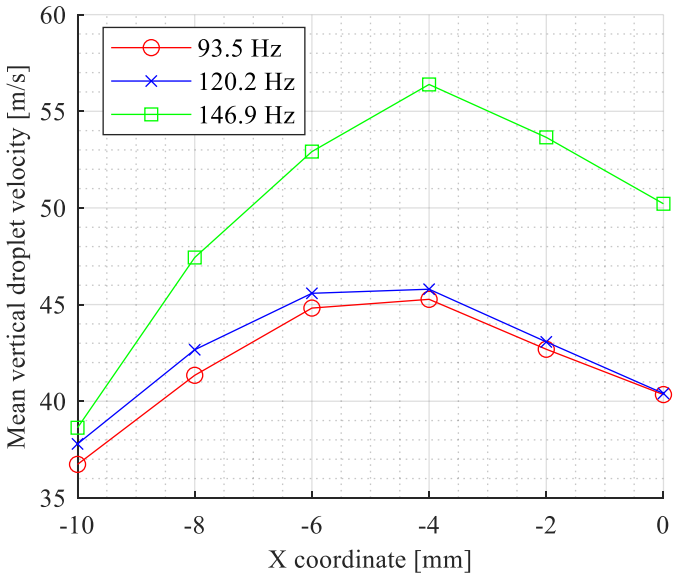

Figure 4.47: Mean vertical velocity averaged in time.

Figure 4.48 shows the amplitude of the droplet vertical velocity for each point of the X-axis and for each excitation frequency. It is clear that the amplitude of the droplet velocity follows the trend of the amplitude of the air at $X = 0$ mm (highest at 120.2 Hz, medium at 93.5 Hz, minimum at 146.9 Hz). The same trend appears also in the other positions. Furthermore, there is a peak of the amplitude at $X = -4$ mm or $X = -6$ mm, which matches with the peak of the average velocity around $X = -5$ mm.

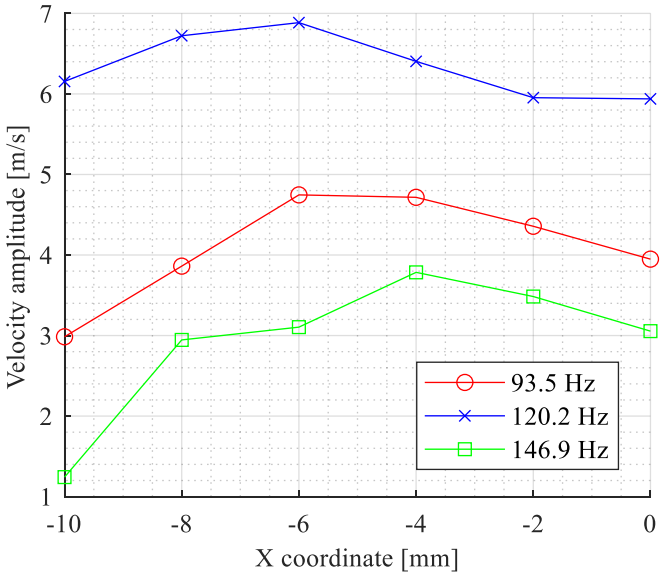

Figure 4.48: Droplet vertical velocity amplitude.

5 Summary and outlook

To face the problem of harmful emissions in jet engine applications, the LPP combustor concept gained more importance during the last years. Them, being more prone to thermoacoustic instabilities, the need to predict them has become of primary importance. The purpose of this work is to provide support in the understanding of these phenomena, in particular experimental data regarding the influence of air instabilities on the produced spray. These experimental data can be used to develop and train machine learning algorithms that will be able to better predict those instabilities.

In an atmospheric conditions setup, the characterization of the forced airflow was performed with CTA hot wire anemometry in preliminary tests. Phase Doppler Anemometry was the method utilized to investigate the spray properties under steady and unsteady airflow conditions: SMD, mean diameter, droplet distributions, velocities, velocity angle, volume flows, mass fluxes and number of droplets. Furthermore, investigations on smaller drop diameters were applied to justify some of the experimental results.

From the steady airflow tests in section 4.1 it is possible to observe that SMD presents a local maximum under the atomization edge but the mean diameter does not, because the number of small droplets (diameter below 25 µm) is higher in this position and therefore the distribution is changing (Figure 4.2, Figure 4.3 and Figure 4.4). The mean vertical velocity shows symmetrical local maximum at approximately $X = \pm 5$ mm and it increases by moving far away from the atomization edge, while the mean horizontal velocity increases going towards the extremes of the investigated X interval. As expected, the mass flux has a maximum under the atomization edge, and it decreases moving at the extremes of X coordinate.

Along the direction of the atomization edge (Y coordinate), the spray properties remain almost constant, especially the spray mass flux. The algorithm to calculate the spray mass flux proposed by Saffman [42] is validated since it gives back a result that is consistent with the actual value measured by the mass flow meter, as shown in 4.1.2.

Investigating the influence of an increasing pressure drop across the nozzle, the SMD, mean diameter and mass flux keep decreasing while the velocity increases. Only for the highest pressure drop (3.5 %), the trend is not confirmed, since both mean diameter and mass flux turn to be bigger (and the velocity smaller) than the respective values at 3 %. Further investigations are suggested.

Looking at the influence of the temperature parameter, the biggest drop in the mean diameter happens by preheating from the environment conditions to 100 °C, while the SMD slightly increases. The contradiction is also confirmed by the droplet distribution, but a future in-depth study can be useful to understand the physical meaning of this phenomenon. For increasing values of temperature above 100 °C, the properties do not change significantly. A reason for that could be the influence of evaporation that can cause a bigger effect only until the evaporation temperature, in the range between 20 °C and 100 °C. Further research is recommended.

The unsteady airflow tests presented in section 4.2 were performed at three different airflow excitation frequencies (93.5 Hz, 120.2 Hz and 146.9 Hz) that cover a wide range of velocity amplitudes (Figure 4.36). The SMD confirms the same trend of the steady airflow test along the spatial coordinate (X coordinate) and it is shifted approximately 180° with respect to the mean vertical droplet velocity due to the size-velocity inverse proportionality. As in the steady airflow test, the mean vertical droplet velocity shows a peak around the spatial position $X = -5$ mm. The amplitude of the fluctuation remains almost constant at each X position. The velocity angle keeps constant in time even though both velocity components oscillate, while obviously increasing its value moving to the sides of the X-axis. The mass flux presents higher values under the atomization edge while its amplitude decreases towards the extremes of the investigated interval: for $X = -10$ mm and $X = -8$ mm, its dependence from time is negligible.

From the comparison between the experiments at the three different frequencies, it appears that at 146.9 Hz there is a higher amount of smaller droplets (diameter below 25 µm) under the atomization edge, while at the extremes of the spatial interval, all the three frequencies show a similar ratio between small and all droplets. The wider range in which this ratio spreads at 146.9 Hz (Figure 4.44) causes a wider gap between the minimum and the maximum velocity for a fixed time instant (or phase angle). In fact, the difference in the number of small droplets (that can obviously reach higher velocities since they have a lower inertia) between the center and the side of the spray is bigger at 146.9 Hz than at 93.5 Hz or 120.2 Hz. For the position $X = 0$ mm, the amplitude of the droplet velocity follows the trend of the amplitude of the air. The maximum vertical velocity amplitude is in the same position of the maximum average vertical velocity, around $X = -5$ mm. This is valid for each excitation frequency. It is, therefore, shown that the forced airflow influences not only the frequency at which the droplet characteristics oscillate, but also the amplitude of this oscillation.

Thanksgiving

Firstly I would like to thank my thesis advisor Thomas for the support during these six months. With him I had the opportunity to work in a very friendly environment and I learnt a lot from his capacities and his attention for details. He has always believed in this project and contributed in a determinant way to make it possible. I would like to express my greetings to professor Zarzalis, who believed in me and gave me the opportunity to have an in-depth study on this subject. I would like to thank also all the guys inside the EBI department. Their knowledge and friendly behaviour always created the right prerequisites to improve myself in different aspects.

Now, I want to say a big thank you to all the friends that shared with me this wonderful year of Erasmus in Karlsruhe, especially the EQUIPO guys. I spent with them all the instants of this experience. If it can be already considered an unforgettable year is thank to you my friends. Also, a special dedication is for my friends of the life. Even though we were physically separated in this last year, they were always present from Pesaro and gave me support and motivation.

Finally, I want to express all my gratitude to my family, my parents Roberto and Emanuela and my brother Francesco. They always encouraged me and supported me along the years of the university. If I always had the stability and the possibility to focus on my goals is because I always felt their presence and their unconditional love.

Thank you very much.

Matteo Occhialini

Bibliography

[1] A. P. Dowling and S. R. Stow, “Acoustic Analysis of Gas Turbine Combustors,” *J. Propuls. POWER*, vol. 19, no. 5, 2003, doi: 10.2514/2.6192.

[2] R. K. Gurubaran, R. I. Sujith, and S. R. Chakravarthy, “Characterization of a prefilming airblast atomizer in a strong swirl flowfield,” *J. Propuls. Power*, vol. 24, no. 5, pp. 1124–1132, 2008, doi: 10.2514/1.35012.

[3] J. C. DeLaat and D. E. Paxson, “Characterization and simulation of the thermoacoustic instability behavior of an advanced, low emissions combustor prototype,” *44th AIAA/ASME/SAE/ASEE Jt. Propuls. Conf. Exhib.*, no. July 2008, 2008, doi: 10.2514/6.2008-4878.

[4] A. J.E. Penner, D.H. Lister, D.J. Griggs, D.J. Dokken and M. McFarland, “Aviation and the global atmosphere. Technical report, Intergovernmental Panel on Climate Change (WMO and UNEP),” 1999.

[5] and H. I. H. S. H. Cohen, G.F.C. Rogers, *Gas Turbine Theory*, 5th editio. 2001.

[6] and I. J. W. Konrad, N. Brehm, F. Kameier, C. Freeman and Day, “Combustion instability investigations on the BR710 jet engine,” *J. Eng. Gas Turbines Power*, pp. 120(39):34–40, 1998.

[7] R. von der Bank and T. Schilling, “Development of an Ultra-Low NOx LP(P) Burner,” 2003.

[8] M. U. E. Canepa, P. Di Martino, P. Formosa and and P. Zunino, “Unsteady aerodynamics of an aeroengine double swirler lpp burner,” 2004.

[9] Rainer Fink., “Untersuchungen zu LPPFlugtriebwerksbrennkammern unter erh¨ohtem Druck,” Technische Universit¨at M¨unchen, 2001.

[10] and H. B. W. H. Pak, E. Hassel, “Stabile, schadstoffarmeMagerverbrennung im nationalen Luftfahrtforschungsprogramm (KEROMIX),” 1998.

[11] L. Bayvel and Z. Orzechowski, *Liquid Atomization*, vol. 53, no. 9. 2013.

[12] A. H. Lefebvre, “Airblast atomization,” *Prog. Energy Combust. Sci.*, vol. 6, no. 3, pp. 233–261, 1980, doi: 10.1016/0360-1285(80)90017-9.

[13] N. Ashgriz, Ed., *Handbook of Atomization and Sprays*. 2011.

[14] B. D. R. Lefebvre Arthur H., *Gas Turbine Combustion 3rd ed*. 2010.

[15] Y. V. I. Borodin V. A., Dityakin YU F, Klyachko L. A., *Atomization of liquids*. Moscow, 1967.

[16] R. W. Tate, "Sprays," *Kirk-Othmer Encyclopedia of Chemical Technology*. pp. 634–654, 1969.

[17] A. H. Lefebvre and V. G. Mcdonell, *Atomization and Sprays, Second Edition.* 2017.

[18] D. M. A. Bermudez, "Spray measurements in a laboratory RQL combustion chamber under high altitude relight conditions," Karlsruhe Institute of Technology, 2020.

[19] M.S. El-Shanawany and A.H. Lefebvre, "Airblast atomization: Effect of linear scale on mean drop size.," *J.Energy*, p. Vol.4(No. 6):80-4097, 1980.

[20] S. Gepperth, A. Müller, R. Koch, and H. Bauer, "Ligament and Droplet Characteristics in Prefilming Airblast Atomization," *ICLASS*, vol. 320, no. 1975, p. 2012, 2012.

[21] M.Sc. Feras Z. Batarseh., "Spray generated by an airblast atomizer: atomization, propagation and aerodynamic instability.," Technische Universit• at Darmstadt, 2008.

[22] O. Klüsener, *The injection process in compressor less diesel engines*. 1933.

[23] and M. Giffen, E., *The Atomization of Liquid Fuels*. New York, 1953.

[24] D. G. Gordon, "Mechanism and speed of breakup of drops," *J. Appl. Phys*, vol. Vol. 30, N, pp. 1759–1761, 1959.

[25] J. O. Hinze, "Fundamentals of the hydrodynamic mechanism of splitting in dispersion processes," *AlChE J.*, vol. Vol. 1, No, pp. 289–295, 1955.

[26] W. R Lane, "Shatter of drops in streams of air," *Ind. Eng. Chem.*, vol. Vol. 43(No, pp. 1312–1317, 1951.

[27] G. H. McKinley and M. Renardy, "Wolfgang von Ohnesorge," *Phys. Fluids*, vol. 23, no. 12, pp. 1–17, 2011, doi: 10.1063/1.3663616.

[28] R. A. Brodkey, *The Phenomena of Fluid Motions*. 1967.

[29] B. E. Gelfand, "Droplet breakup phenomena in flows with velocity lag," *Prog. Energy Combust. Sci.*, vol. Vol. 22, pp. 201–265, 1995.

[30] R.D. Reitz and F.V Bracco, "Encyclopedia of Fluid Mechanics, Mechanisms of breakup

of round Liquid jets," *Encyclopedia of Fluid Mechanics*. Gulf Publishing Company, 2003.

[31] G. Wozniak, *Zerst□aubungstechnik : Prinzipien, Verfahren, Gerate*. 1986.

[32] L. Rayleigh, "On the instability of jets," *Proc. London Math. Soc.*, pp. 4–13, 1878.

[33] C. Weber, "Zum Zerfall eines Flussigkeitsstrahles," *J. Appl. Math. Mech.*, vol. (No. 11), pp. 136–154, 1931.

[34] N. K. Rizk and A. H. Lefebvre, "Influence of liquid film thickness on airblast atomization," *Trans. ASME J. Eng. Power*, vol. Vol. 102, pp. 706–710, 1980.

[35] A. A. Miesse, C. C., Putnam, "Injection and Combustion of Liquid Fuels," vol. Section II.

[36] Johannes Eckstein, "On the Mechanisms of Combustion Driven Low-Frequency Oscillations in Aero-Engines," Technische Universitat Munchen, 2004.

[37] A. Müller, R. Koch, H.-J. Bauer, M. Hehle, and O. Schafer, "Performance of prefilming airblast atomizers in unsteady flow conditions," in *ASME Turbo Expo 2006*, 2006, pp. 1–9.

[38] M. Budakli, T. Gambaryan-Roisman, and P. Stephan, "Influence of surface topography on heat transfer in shear-driven liquid films," *J. Phys. Conf. Ser.*, vol. 395, no. 1, 2012, doi: 10.1088/1742-6596/395/1/012164.

[39] J. Eckstein, E. Freitag, C. Hirsch, T. Sattelmayer, R. von der Bank, and T. Schilling, "Forced Low-Frequency Spray Characteristics of a Generic Airblast Swirl Diffusion Burner," *J. Eng. Gas Turbines Power*, vol. 127, no. 2, p. 301, 2005, doi: 10.1115/1.1789515.

[40] E. O. Doebelin, "Measurement Systems Application Design." pp. 542–555, 1990.

[41] Dantec Dynamics, "BSA Flow Software," p. 417, 2014, doi: 9040U1312.

[42] M. Saffman, "Automatic calibration of lda measurement volume size," in *Applied optics*, 1987, p. Vol. 26, No. 13.

[43] L. R. Collins and A. Keswani, "Reynolds number scaling of particle clustering in turbulent aerosols," *New J. Phys.*, vol. 6, pp. 1–17, 2004, doi: 10.1088/1367-2630/6/1/119.

List of figures

A Appendix: 93.5 Hz results

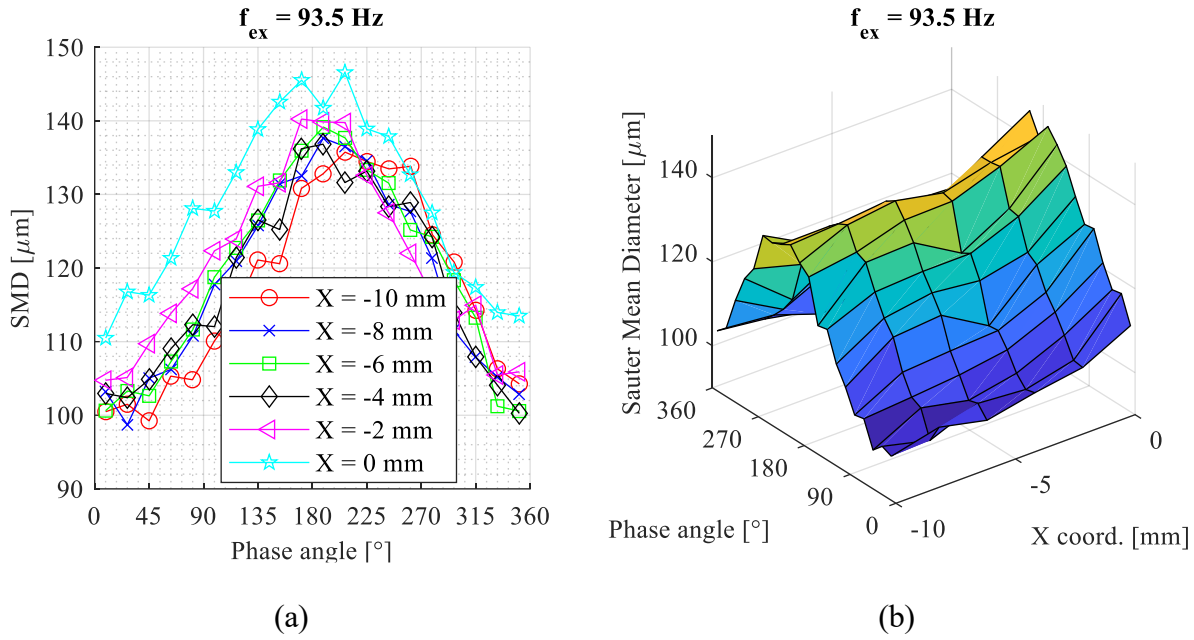

Figure A.1: Sauter Mean Diameter, 93.5 Hz.

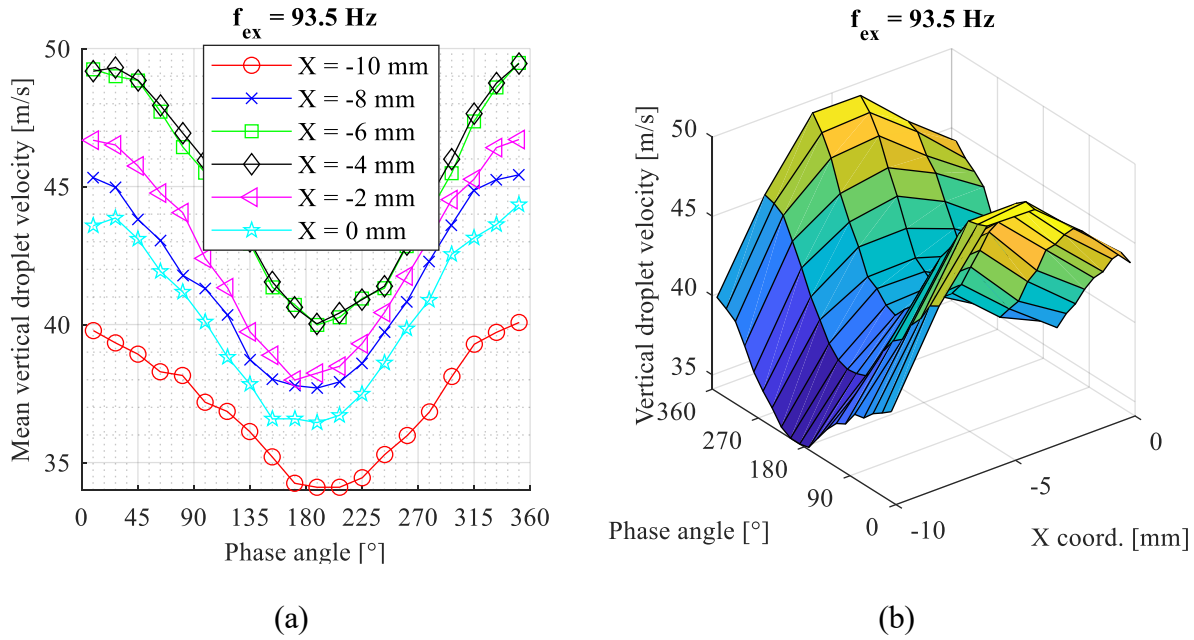

Figure A.2: Mean vertical droplet velocity, 93.5 Hz.

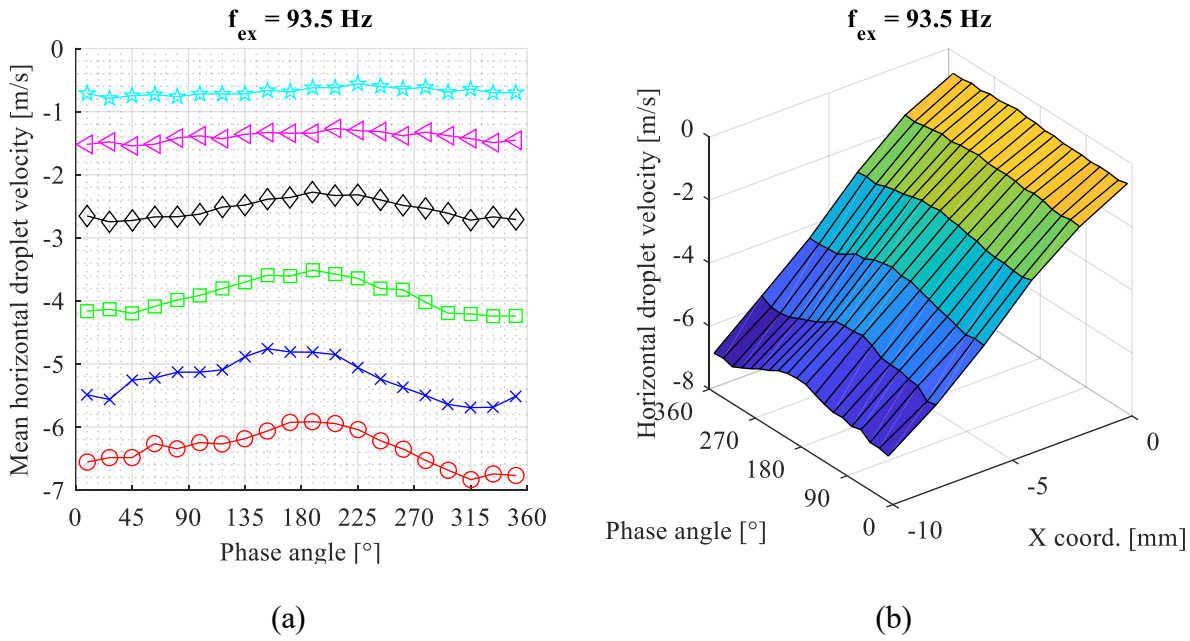

(a) (b)

Figure A.3: Mean horizontal droplet velocity, 93.5 Hz.

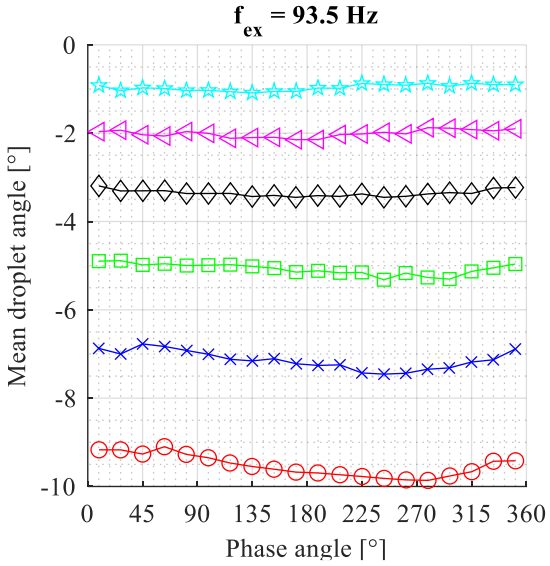

Figure A.4: Mean droplet velocity angle, 93.5 Hz.

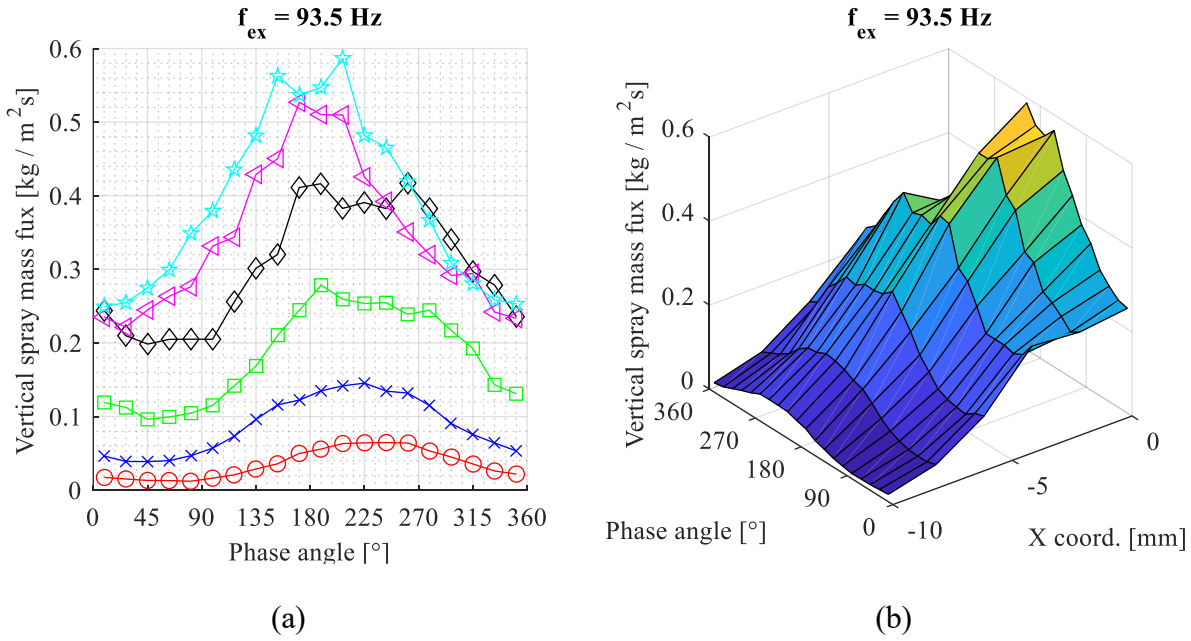

(a) (b)

Figure A.5: Vertical spray mass flux, 93.5 Hz.

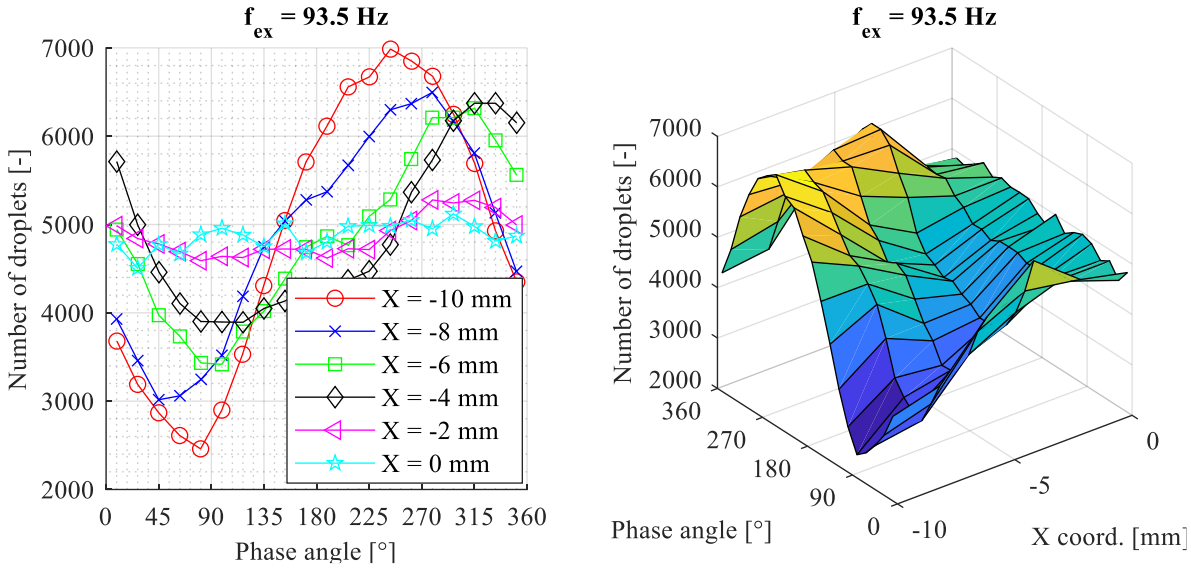

(a) (b)

Figure A.6: Number of droplets, 93.5 Hz.

B Appendix: 146.9 Hz results

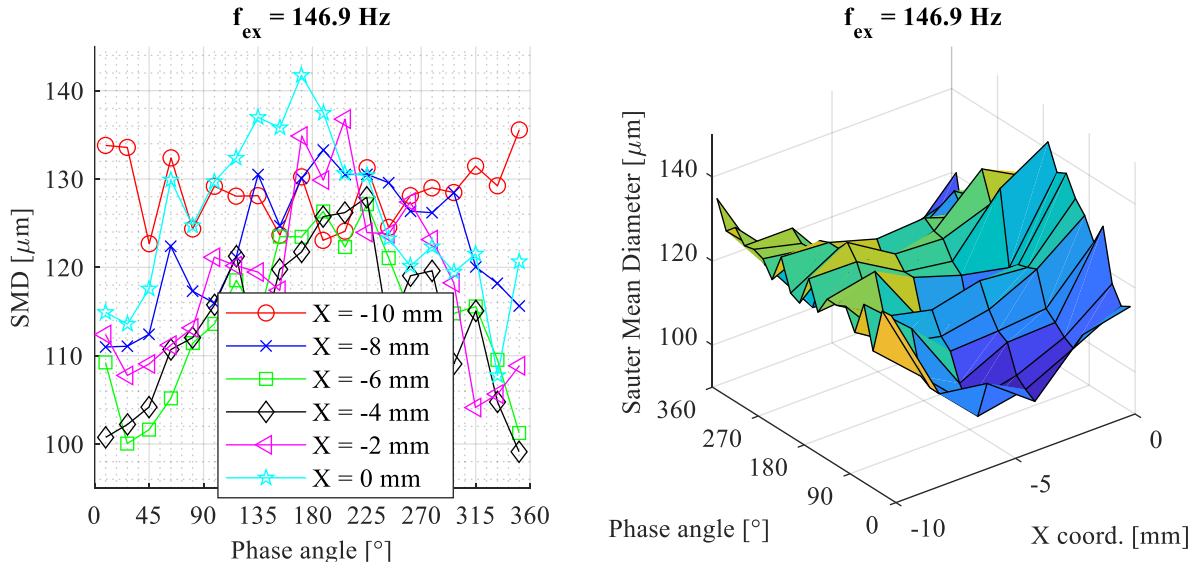

(a) (b)

Figure B.1: Sauter Mean Diameter, 146.9 Hz.

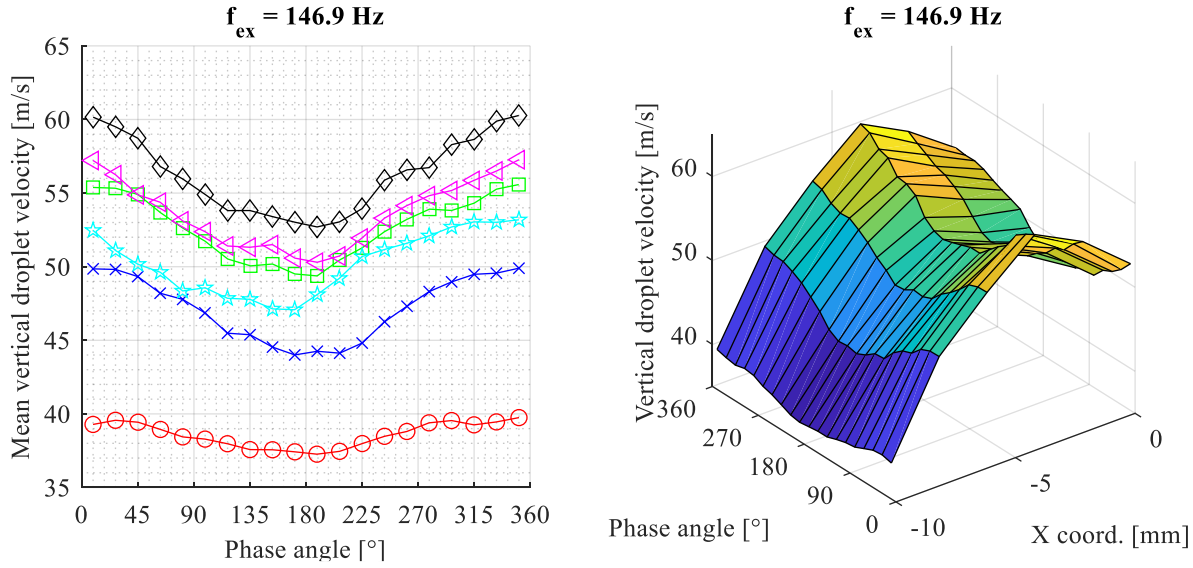

(a) (b)

Figure B.2: Mean vertical droplet velocity, 146.9 Hz.

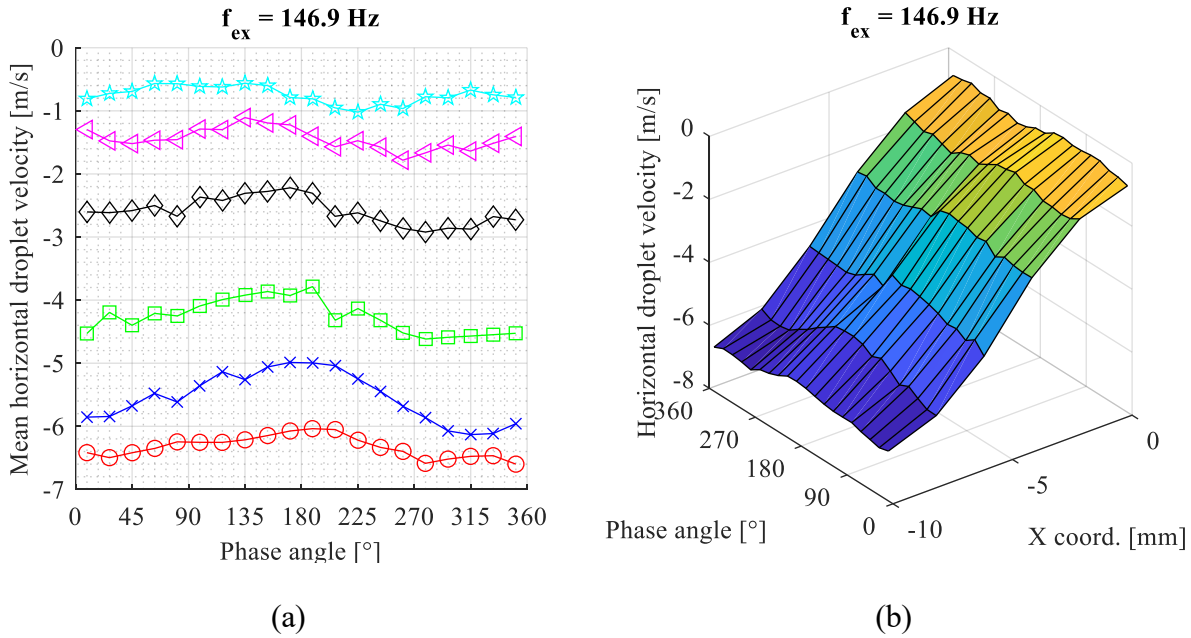

(a) (b)

Figure B.3: Mean horizontal droplet velocity, 146.9 Hz.

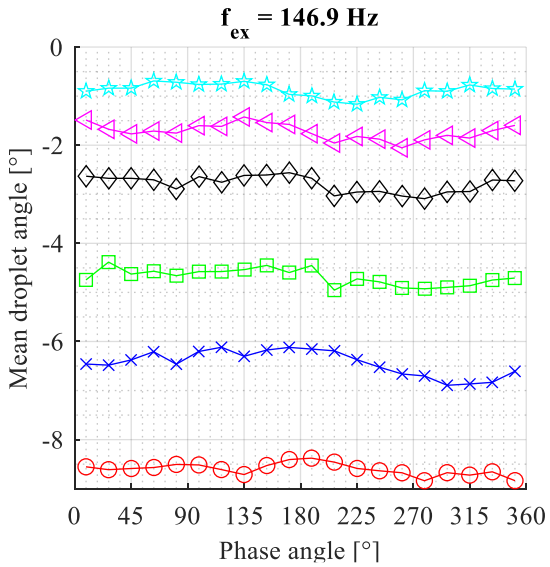

Figure B.4: Mean droplet velocity angle, 146.9 Hz.

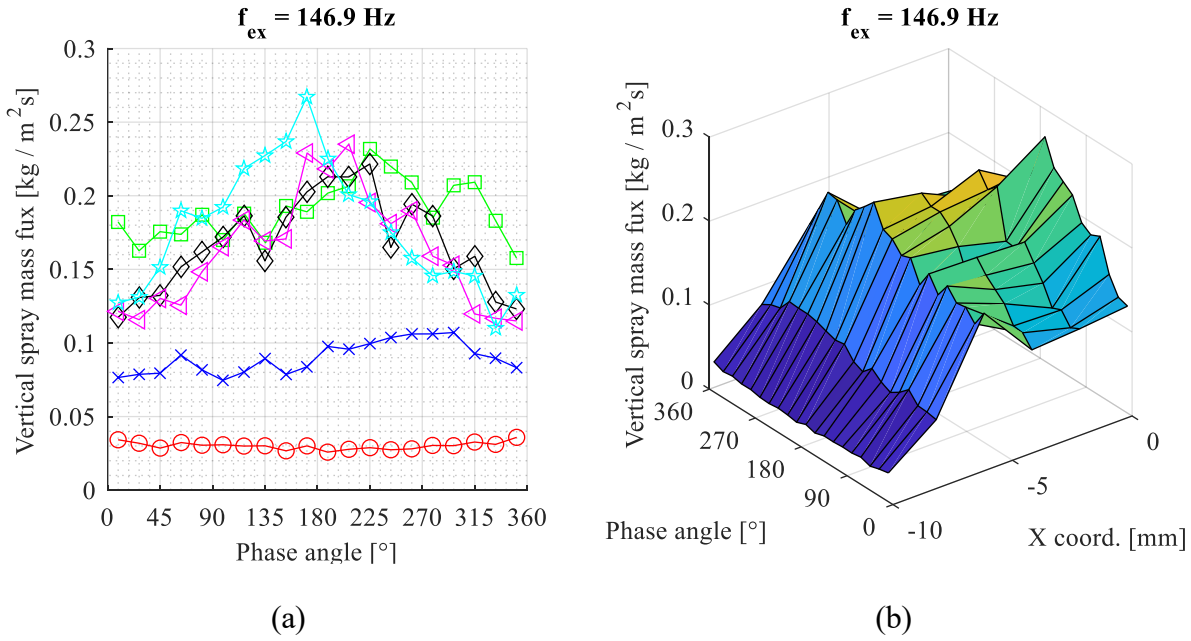

(a) (b)

Figure B.5: Vertical spray mass flux, 146.9 Hz.

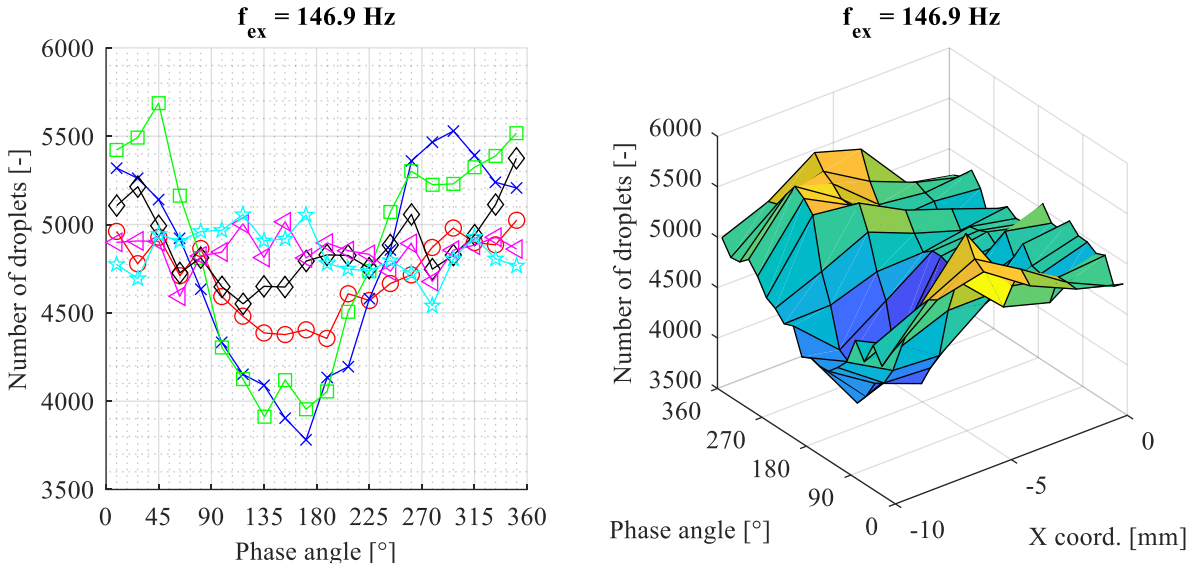

(a) (b)

Figure B.6: Number of droplets, 146.9 Hz.